Analysis of Zincblende-Phase GaN, Cubic-Phase SiC, and GaAs MESFETs Including a Full-Band Monte Carlo Simulator

A Thesis
Presented to
The Academic Faculty

by

Michael Weber

In Partial Fulfillment
of the Requirements for the Degree
Doctor of Philosophy

School of Electrical and Computer Engineering
Georgia Institute of Technology
December 2005

Analysis of Zincblende-Phase GaN, Cubic-Phase SiC, and GaAs MESFETs Including a Full-Band Monte Carlo Simulator

Approved by:

W. Russell Callen, Advisor
School of Electrical and Computer Engineering
Georgia Institute of Technology

Bruno Frazier
School of Electrical and Computer Engineering
Georgia Institute of Technology

Kevin F. Brennan, Co-Advisor
School of Electrical and Computer Engineering
Georgia Institute of Technology

Christopher J. Summers
School of Materials Science and Engineering
Georgia Institute of Technology

Farrokh Ayazi
School of Electrical and Computer Engineering
Georgia Institute of Technology

Hao Min Zhou
School of Mathematics
Georgia Institute of Technology

Date Approved: September 22, 2005

For my family and friends

ACKNOWLEDGEMENTS

A thesis is not the just work on one individual; it is the culmination of ideas, work, and support from many people. This work is no different.

First and foremost I would like to thank my advisor, Dr. Kevin F. Brennan. Kevin was so much more than an advisor; he was a friend, a mentor, a teacher. Without his endless support and guidance, there would be no thesis. And even in his own, difficult, times he never waivered in his leadership and wisdom. For everything you have done for me, academic and personal, I thank you. You will be missed.

The convergence of this work has been rough at times, and I have no one more to thank for his help at the finish than Dr. Russ Callen. Thank you for stepping in as my advisor in Kevin's absence. Your support, time and energy is greatly appreciated. I could not have finished without you.

I would like to thank Dr. Enrico Bellotti for his intellectual guidance. You have been a great collaborator, and I hope that we will continue to work together in the future.

Louis Tirino, my friend, thank you. I could not have survived without you. You have been a much-needed partner during the last 4 years. I will never forget how much you have done for me.

I would like to also thank some of my friends. They have been there throughout the process with support and good times. Thank you, Matt Hill, Brian Thoma, Matt Bain, James Brandtjen, Nate Mansfield, you have all helped in more ways that you can imagine.

Thank you to my family. My parents, Joel and Sheryll, my brother, David, my aunts, Dale and Robin, my cousins, Patrick and Joanna. You have all supported me

though this crazy endeavor. Your love and guidance has kept me on track to the finish line. Dale, thank you for our talks toward the end. I needed someone else to guide me, and you were there for me. Mom and Dad, your support for my decision has been tremendous, and you always believed in me; I will never be able to thank you enough.

Finally, I would like to thank my girlfriend, Jennifer Pero. You were not there from the beginning of my quest, but as far as I'm concerned I didn't really start until you appeared. Thank you so much for you support and patience. Everything is finished now, and we can finally move on.

TABLE OF CONTENTS

LIST OF TABLES

LIST OF FIGURES

SUMMARY

The objective of this research has been to study the high-power device properties of emerging cubic-phase semiconductors. Though the wide-bandgap semiconductors have great potential as high-power microwave devices, many gaps remain in the knowledge about their properties.

The calculations in this work are performed using a ensemble Monte Carlo simulator. The simulator was designed from the ground up to include accurate, numerical band structures derived from an empirical pseudo-potential model. The carrier-phonon scattering rates and impact ionization rates are derived from the calculated band structures. The Monte Carlo simulator is fully-numeric, eliminating the partial analytic calculations that existed in previous versions. This not only improves the accuracy of the simulations, but also allows free movement among many different materials with no change to the simulator (a feature not possible in previous versions). Additional improvements have been made to the simulator: the generalized device structure simulation, the fully-numerical final state selector, and the inclusion of the overlap integrals in the final-state selection.

The device structure used in this work is a metal-semiconductor-field-effect-transistor (MESFET). This is a common device structure used for the materials in question: cubic-phase silicon carbide (3C-SiC), zincblende-phase gallium nitride (ZB-GaN), and gallium arsenide (GaAs). 3C-SiC and ZB-GaN are the wide-bandgap semiconductors on which this work focuses. GaAs is used as a control for the simulator and as a small-bandgap comparison material.

The first comparison that is made among the materials is direct-current breakdown. DC breakdown is a common calculation that occurs when the drain voltage

on the transistor causes significant enough impact ionization to induce an impact ionization current. The voltage at which breakdown occurs is a good indication of how much power a transistor can provide. It is found that GaAs has the smallest DC breakdown, with 3C-SiC and ZB-GaN being over 3 times higher. This follows what is expected and is discussed in detail in the work.

The second comparison made is the radio-frequency breakdown of the transistors. When devices are used in high-frequency applications it is possible to operate them beyond DC breakdown levels. This phenomenon is caused by the reaction time of the carriers in the device. It is important to understand this effect if these materials are expected to be used in a high-frequency application, since this effect can cause a change in the ability of a material to produce high-power devices. MESFETs made from these materials are compared and the results are discussed in detail.

CHAPTER I

INTRODUCTION

1.1 Wide Bandgap Semiconductors

The objective of the proposed research is to analyze device performance for emerging cubic-phase wide-bandgap semiconductors. The relevance of this research comes from the increasing demand of both high-performance and high-power applications. Wide bandgap semiconductors have received much attention recently in both high-frequency and high-power applications. For instance, in the telecommunications market, very high-power microwave transistors are desirable in cellular base stations. In addition, applications in communications and data storage have urged the development of short wavelength, including blue and ultraviolet, detectors and emitters.

Specifically, this research will focus on the characteristics of cubic-phase silicon carbide (3C-SiC) and zincblende-phase gallium nitride (ZB-GaN) metal-semiconductor-field-effect-transistors (MESFETs). The characteristics of transistors constructed from these materials, including device breakdown and frequency effects, will be compared to a mainstream and well-known gallium arsenide (GaAs) transistor. The goal of the research is to fill a void in the theoretical study of wide-bandgap semiconductors. Cubic-phase wide-bandgap materials tend to be overshadowed by their wurtzite phase counterparts because of the difficulty in obtaining experimental data. We hope that this research will give benchmark results for these materials that can be used as

a guide by both theorists and experimentalists.

The result will be important information about the device performance available using these materials. The results in this thesis are obtained using a modeling technique known as material-theory-based modeling. Material-theory-based modeling allows the computation of transport properties for a material using little *a priori* information. In addition, the model can be extended to allow the simulation of devices made from the materials. Device results from these materials is the focus of this work.

1.2 History and Motivation

The classification of wide-bandgap semiconductors is varied. Since the primary physical properties of a semiconductor scale to a certain degree with the energy gap, this parameter provides a reasonable classification scheme. However, comparisons with Si and GaAs are common, because of the importance of these common materials. So, in general, a wide-bandgap semiconductor is classified as a material with a bandgap at least twice the bandgap of Si. This gives a range from about 2eV (with InN and 3C-SiC) up to 6eV (with AlN and diamond).

Because of this larger bandgap, wide-bandgap semiconductors are becoming very important materials for short-wavelength optoelectronic device applications [1–4] and for high-powered microwave devices [5–9]. Their high breakdown fields, large saturation and overshoot velocities [10–16], low dielectric constants, and high thermal conductivities are especially important for microwave power amplifiers. These features result in devices with excellent high-power and high-frequency performance. Devices

made from these materials can produce significantly higher amounts of power compared to those of the more common semiconductor materials, silicon (Si) and GaAs.

Light-emitting diodes (LEDs) created from wide-bandgap semiconductors (specifically the III-Nitride family) can emit blue and ultraviolet light, extending the range of devices to the smaller wavelength side of the spectrum. Blue LEDs fill a gap in the color spectrum of light-emitting devices. With the addition of blue LEDs to the more common red and green LEDs, full-color semiconductor displays become possible.

Semiconductor devices that can withstand high-temperature environments are becoming more important. Wide bandgap semiconductors find applications in aerospace, satellites, and automobile engines. Such applications demand high performance in harsh environments. For instance, Si becomes intrinsic at 200 °C, limiting its device performance in these environments.

In addition, wide-bandgap materials can provide higher power densities than can their mainstream counterparts. The maximum power achievable from a device is proportional to the square of the difference of the breakdown voltage and the knee voltage (Eq. 1), and the breakdown voltage is principally determined by the bandgap of the material. So, a material with a larger bandgap, in general, can produce a higher power density than can a material with a smaller bandgap. The maximum power is

$$P_{max} = \frac{(V_{BR} - V_{knee})^2}{8R_L}, \tag{1}$$

where P_{max} is the maximum power, V_{BR} is the DC breakdown voltage of the

device, V_{knee} is the knee voltage of the device and R_L is the load resistance. Although the benefits of wide bandgap materials are significant, they are not as technologically mature as Si and GaAs. Si and GaAs can easily be grown, and their transport characteristics are very well known. Wide bandgap materials, specifically the III-nitride and silicon carbide families, are relatively much more difficult to grow and process into devices. For this reason, these materials are not nearly as well studied as are Si and GaAs. Currently, 4H-SiC MESFETs and wurtzite-phase AlGaN/GaN high electron mobility transistors (HEMT) are the most popular wide-bandgap devices, with extensive experimental results, while the cubic-phase GaN and SiC MESFETs attract little attention. At best, only fragmentary experimental data for cubic-phase materials are available, thus frustrating a firm understanding of these materials. The progress in the development of III-nitride and SiC based devices is hampered by the difficulty in growing high quality material and in reproducibly fabricating working devices. Presently, it is necessary to use theoretical techniques that can predict material and device performance in advance of experiment in order to assess the relative merits of cubic-phase wide-bandgap semiconductor devices.

1.2.1 The Silicon Carbide Family

SiC has been recognized for a long time as a semiconductor of great importance in electronic applications because of its properties, the possibility of easy growth on a native oxide, and the presence of numerous polytypes [17–20]. The SiC family of semiconductors contains the same semiconductor material grown in many polytypes. The most commonly grown SiC materials are 3C-SiC, 4H-SiC and 6H-SiC.

SiC materials, although varied, generally have high thermal conductivities and high saturation velocities, which make them suitable for high-temperature (above 500K), high-frequency applications [21]. Optoelectronic devices are impractical with the SiC materials because they are indirect semiconductors.

The wireless market typically requires power amplifiers for base-station operation to perform effectively in the 100-1000 watt range [22]. Si devices are used now; however, SiC-based devices can reduce the number of components needed to achieve the same power output, reducing cost and increasing reliability. For applications beyond 2.5 GHz, Si is no longer an option; GaAs and SiGe become options. While these two materials can provide the frequency range needed, they would be weaker at providing the necessary power densities. As a result, SiC-based devices are potential candidates for these high-frequency, high-power applications. Another advantage of SiC is that the fabrication technology is much simpler than that required with III-V HEMTs.

The different polytypes of SiC result from the substrate choice and growth conditions. 6H and 4H are the easiest to grow and are usually epitaxially grown on a Si substrate [5]. As a result, 6H and 4H receive the most attention from both experimentalists and theorists [23–27]. The cubic phase, 3C, is difficult to grow because it does not have a native substrate, thus it receives less interest and, as a result, very little is known about it. In recent years there has been some more interest in 3C-SiC, resulting in both experimental and theoretical work [23, 27–29]. The most difficult to grow is 2H, because of its high formation energy.

1.2.2 The III-Nitride Family

The III-nitride family of semiconductors can fill the emerging market for semiconductor optoelectronic devices. Their large, direct bandgap can be used to produce both blue and ultraviolet emitters and detectors. In addition, for high-frequency, high-power applications, GaN FETs can be employed. The high on-state resistance of Si limits its application to about 100 V at 1 A. FETs made from GaN have a much lower "on" resistance. And although GaN does not have as high a thermal conductivity as SiC, other properties (breakdown field, saturated drift velocity, dielectric constant and carrier mobilities) make it another attractive candidate for high-power, high-frequency devices. Another very important advantage GaN has over SiC is the ability to form heterojunctions. The fact that GaN, together with InN and AlN, allows the formation of heterostructures provides some interesting device possibilities.

The III-nitride family consists of the binary semiconductors, InN, AlN, and GaN, and the ternaries composed of them, $Al_xGa_{1-x}N$, $In_xGa_{1-x}N$ and $In_xAl_{1-x}N$. GaN can be grown in two phases, zincblende (ZB) and wurtzite (WZ), while the remaining III-nitride semiconductors only have the wurtzite polytype. The III-nitride family of materials has gained interest in both optoelectronic and power devices.

Their technological immaturity is mainly due to fabrication problems; however, in recent years, advances have been made in the wurtzite-phase versions. Again, as with the SiC family, the wurtzite-phase materials receive most of the attention because of the relative ease of growth when compared to ZB-GaN. Much work has been completed, both experimental and theoretical, for the wurtzite-phased III-nitrides

[11, 14, 15, 30–39]. Some theoretical studies have been completed for ZB-GaN, with most of the work coming from our group [14, 15, 30, 31, 34, 37, 39–41]. In this respect, this research concentrates on improving the models used for the simulations.

1.2.3 Gallium Arsenide

Gallium arsenide (GaAs) has been extensively studied by both experimentalists and theorists. GaAs is a mainstream semiconductor used in both optoelectronic and device structures. GaAs has been extensively studied with the Monte Carlo method [42–46]. The principal reason for including GaAs in this study is to provide a baseline comparison of the GaN and SiC devices. In this way, the GaAs calculations serve as a control on the model, enabling an accurate description and comparison of the operation of the various device structures.

1.3 Material-Theory-Based Modeling

We have developed a modeling technique that can proceed with only limited reliance on experimental data. This technique is called material-theory-based modeling [33, 47]. The capability of the material-theory-based modeling method is particularly useful in studying the wide-bandgap semiconductors since reproducible, reliable experimental data are not available for most of the III-nitride and SiC families of materials. The goal of material-theory-based modeling is to function as a predictive technique. Material-theory-based modeling consists of a series of hierarchical modeling tools that extend from a fundamental physics-based, microscopic analysis to engineering-based device models. The key ingredient within the material-theory-modeling method is the full-band, ensemble Monte Carlo technique [43, 48]. We have

further improved our earlier full-band Monte Carlo simulator by reformulating the scattering rates using a fully numerical approach [49]. In this way, all of the important transport parameters, band structure, phonon scattering rates, and impact ionization rates enter the Monte Carlo code numerically. Much of the parameterization of the method is thus removed, and the simulation can proceed with little reliance on experimental measurements of transport phenomena. The primary ingredients to the simulation are an accurate, numerically generated, full-band structure, phonon energies, dielectric constants, and deformation potentials.

Using the material-theory-based modeling paradigm, we have developed a comprehensive self-consistent device simulator, including both zincblende phase and wurtzite phase materials [31,40,50]. As mentioned above, in the present work, we have extensively updated and improved the Monte Carlo simulator. In addition to our work, Dessenne et al reported a ZB-GaN MESFET Monte Carlo simulation; however, it was based on an analytical band structure approximation, limiting its use in device breakdown analysis [51]. Very little analysis of the transport dynamics within 3C-SiC has been reported [29]. Some studies of bulk transport in 3C-SiC have been reported [28,29], but there are no known theoretical or experimental studies of 3C-SiC MESFETs.

As stated before, material-theory-based modeling can compute transport properties and device characteristics for immature semiconductor materials. The model used in this research was designed to be both more general and more accurate than its counterpart [41]. The material-theory-based model uses five main components. Figure 1 shows an overview of these five components. The components are material

parameters, band structure, scattering rates, bulk simulator, and device simulator. The model starts with some basic material parameters including bandgaps, dielectric constants, optical data, phonon information, and lattice constants. These parameters are used throughout the simulator, all the way from the band structure calculations to the device simulator.

1.3.1 Boltzmann Transport Equation

The Boltzmann transport equation (BTE) is the form of the carrier distribution function in the non-equilibrium conditions of a semiconductor. There are many ways to solve the BTE, each with advantages and disadvantages. The two primary ways of solving the BTE are analytically, using either drift-diffusion or hydrodynamic simulators [52], and fully-numerically, using a complete Monte Carlo device simulator.

The analytical methods for simulating semiconductor materials are very useful. Analytic methods are typically used in situations where full-band Monte Carlo cannot be used. This includes situations when long simulation times are needed, complex 2D device structures are present, or when a complete 3D device structure is required. The Monte Carlo model is arguably the most accurate way of simulating semiconductor materials and devices. A Monte Carlo simulation can provide insight into semiconductor characteristics up to breakdown. Analysis of high-field and high-energy regions are the primary reason for employing a Monte Carlo simulator. In addition, if no experimental (or previous *ab initio* theoretical) work is available for a semiconductor material, analytic models cannot be used; however, a Monte Carlo simulator can be used even when there is very little information available.

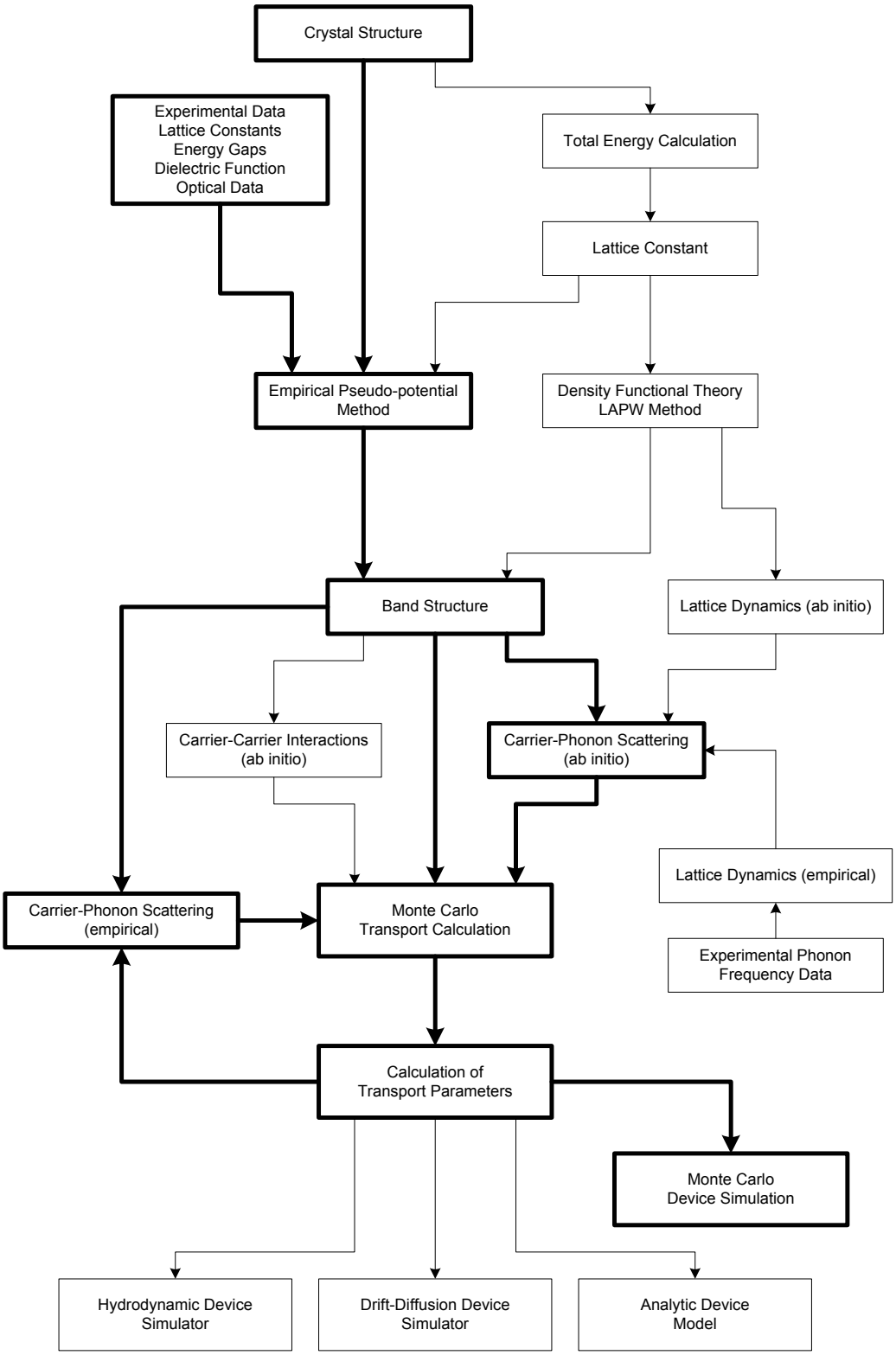

Figure 1: The hierarchical chart for the material-theory-based modeling technique.

1.3.2 Bulk Simulation

The first step in the simulation technique is the computation of the band structure. The band structure is integral to the entire simulation, and every module in the simulation uses it in some fashion. The band structure is computed using the empirical pseudo-potential method (EPM). EPM computes the form factors for a semiconductor material. It uses the simplex minimization algorithm to minimize the error between the experimental band structure information and the form-factor computed band structure [53–56]. The result is a band structure that closely matches the experimental information available.

Next, using the obtained band structure for the material, the model calculates the scattering rates for the material. The scattering rates are integral to the transport and device calculations. The scattering rates define the response of the particles to the semiconductor lattice [15,24,34,46,57–63]. The simulator in this work includes all of the scattering rates that are active in the cubic-phase materials presented: acoustic, non-polar optical, polar optical, impurity, and impact ionization. The calculations of each of the rates is completely numerical, and the integration of the rates includes new information on convergence [64]. In addition, to maintain the minimization of fitting parameters, only two empirically defined parameters are used in the scattering rates: the inter-band acoustic deformation potential and the intra-band acoustic deformation potential [65].

The major section of the material-theory-based model is the Monte Carlo simulator itself. The Monte Carlo method is a stochastic method, deriving its name from

the gambling city of Monte Carlo, located in Monaco. In principle, the Monte Carlo method can be used to solve a wide range of mathematical problems. The Monte Carlo method hinges on the use of randomly generated numbers to solve (in this case) an integro-differential equation, the BTE. The Monte Carlo simulator takes the band structure, the material parameters, and the carrier scattering rates and solves the BTE to produce basic transport properties of the materials such as steady-state drift velocities, impact ionization coefficients, carrier mobilities, and diffusivities. From here, the process can move directly to a Monte Carlo device simulation (such as in this work), or these computed material parameters can be the inputs to an advanced drift-diffusion or hydrodynamic device simulator.

1.3.3 Device Simulation

The Monte Carlo device simulator is a simple extension to the bulk Monte Carlo simulator above. The primary differences include real-space simulation of the carriers, boundary conditions from the layout of the device, and Poisson solutions to obtain electrostatic potentials. The device simulator presented in this work is a general device simulator; it is not limited to MESFET layouts (however only MESFET structures are analyzed in this research). With the device simulator, both DC and high-frequency analyses can be performed, and detailed insight into the operation of devices can be gleaned from the microscopic variables present in the simulator.

1.4 Summary

This research focuses on the the device performance of emerging cubic-phase wide-bandgap semiconductors. Using a general full-band Monte Carlo simulation model

provides highly accurate performance evaluation, in both bulk semiconductor materials and MESFET devices. The goal of this research is to provide benchmark performance figures for zincblende-phase GaN and cubic-phase SiC.

This thesis is organized into seven sections. The first chapter provides a general introduction to the goals of this research and gives an overview of the materials analyzed in the research and the methods used. The second chapter presents an overview of the various semiconductor modeling techniques and introduces the Monte Carlo simulation technique. Chapter 3 describes the Monte Carlo technique used to simulate the materials. Chapter 4 extends the Monte Carlo simulation model to include device modeling. Next, the result of the DC breakdown study of MESFETs is presented in Chapter 5. Chapter 6 details the high-frequency study of the MESFET devices. Finally, Chapter 7 provides general conclusions and recommendations for future work.

CHAPTER II

SEMICONDUCTOR MODELING

2.1 The Boltzmann Equation

The Boltzmann transport equation (BTE) is the form of the carrier distribution function in the non-equilibrium conditions of a semiconductor:

$$\frac{\partial f}{\partial t} + \frac{\boldsymbol{F}_{ext}}{\hbar} \cdot \boldsymbol{\nabla}_k f + \boldsymbol{v} \cdot \boldsymbol{\nabla}_x f = \left(\frac{\partial f}{\partial t}\right)_{scatterings} \tag{2}$$

This equation governs the motion of charge in the six-dimensional phase-space formed by real-space locations and wave vectors (also referred to as phase-space or k-points). The distribution function, $f(\boldsymbol{k}, \boldsymbol{r}, t)$, defines the probability of finding a particle at real-space position $\boldsymbol{r}$, with wave-vector $\boldsymbol{k}$ at time t. From a given initial distribution of particles, the BTE describes the behavior of f as a function of time, where $\boldsymbol{F}_{ext}$ is the external electric field applied to the material, and $\boldsymbol{v}$ is the average velocity of the distribution.

The BTE, however, is not an exact solution to the non-equilibrium conditions of a semiconductor. Two assumptions have been made in the derivation of the BTE. The first is that the distribution function is assumed to be classical; both the real-space and phase-space components are specified simultaneously. Of course, this violates the

Heisenberg Uncertainty Principle. Therefore, the BTE is valid only when quantum-mechanical effects are not present. Second, the scatterings in the BTE are assumed to be instantaneous. Scatterings, however, do have a finite duration, and, in practice, the external field can affect the carrier during a scattering event. Neither of these assumptions affects the results in this work. The devices analyzed in this research do not contain quantum effects (because the scale of the devices is large enough to prevent such effects), so the classical assumption is valid, and the instantaneous scattering assumption is invalidated only at very high fields, which never appear in this work.

2.2 Analytic Methods

Analytic methods for simulating semiconductor materials are very useful. They provide moderate accuracy and fast execution times. Analytic methods can also be used in situations where full-band Monte Carlo calculation cannot. When long simulation times, 3D device structures, or complex device layouts are required, analytic simulation methods are very effective. The drift diffusion and hydrodynamic models are the two most widely used analytic BTE simulation models.

2.2.1 Drift-Diffusion and Hydrodynamic Model

The drift-diffusion (DD) model starts with a simplified version of the BTE, which is then reduced to simple differential equations by employing the method of moments. The DD model first simplifies the BTE by assuming that the change in the distribution of the particles can be approximated by a relaxation time, τ, assumption (Eq. 3).

$$\left(\frac{\partial f}{\partial t}\right)_{scatterings} = -\frac{f - f_0}{\tau} \tag{3}$$

Now, with the simplified BTE, the first two moments are evaluated to produce the carrier continuity equations (Eq. 4) and the drift-diffusion equations (Eq. 5). These equations, when combined with the Poisson equation, form the DD model.

$$\begin{aligned} \frac{\partial n}{\partial t} + \boldsymbol{\nabla}_x \cdot (n\boldsymbol{v}) = 0 \\ \frac{\partial p}{\partial t} + \boldsymbol{\nabla}_x \cdot (p\boldsymbol{v}) = 0 \end{aligned} \tag{4}$$

$$\begin{aligned} \boldsymbol{J}_n = q\mu_n n\boldsymbol{F} + qD_n\boldsymbol{\nabla}_x n \\ \boldsymbol{J}_p = q\mu_p p\boldsymbol{F} - qD_p\boldsymbol{\nabla}_x p \end{aligned} \tag{5}$$

The DD model is very good at computing the means of the particle distribution (voltages, currents, etc.) on fairly large devices, but the model breaks down quickly when the transients are quickly changing and when the analysis requires knowledge of the high-energy tail of the distribution. Since this work concentrates on the breakdown of sub-micron devices, the DD model is not acceptable. The breakdown of a device is a high-energy phenomenon, and simulating the high-energy regime is a weak point of the DD model. In addition, the feature lengths in this work are small, and as the feature length of devices shrinks, the system moves away from quasi-steady-state

conditions and can generate fast changing transients, again, a weakness of the DD model. One option to try to overcome these drawbacks is to take additional moments of the BTE.

The hydrodynamic model does improve upon the DD model, but not in the cases analyzed in this work. The hydrodynamic model involves taking more moments of the BTE. It adds temperature effects and energy continuity, slightly increasing the high-energy validity of the simulator. The focus of this work is device breakdown, which relies completely on the high-energy effects, so the hydrodynamic model cannot be used either. Detailed information about the hydrodynamic model is found in Smith et al. [66].

2.3 Monte Carlo Model

With all of the disadvantages of the method of moments (at least with respect to this work), we examine the Monte Carlo (MC) model. The Monte Carlo model is arguably the most accurate way of simulating semiconductor materials and devices. This accuracy, however, comes at a price. First, an overview of the Monte Carlo method is given, then the specific case of solving the BTE is examined.

2.3.1 The Monte Carlo Method

The MC method can be used to solve a wide range of mathematical problems. The MC method hinges on the use of randomly generated numbers to solve (in this case) an integro-differential equation (the BTE). However, before moving into the more complicated solution of the BTE, it is useful, as an example, to examine a very simple case of MC use.

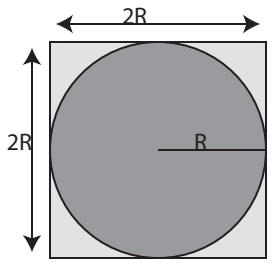

Figure 2: The basic schematic for computing π using the Monte Carlo method.

The example will calculate the value of π. By following this simple example through, we can see how the MC method operates and evaluate the advantages and disadvantages of the MC method. The basic idea behind calculating the value of π with MC starts by inscribing a circle in the the square occupying $x \in [-R, R]$ and $y \in [-R, R]$. The area of the circle will be πR^2 and the area of the square will be $4R^2$, so the ratio of the area of the circle to the area of the square is $\pi/4$ (Figure 2). This means that for N random points in the square, there should be approximately $N\frac{\pi}{4}$ of the points in the circle. From this fact, the MC method for calculating π is apparent:

1. Pick a point in the square $x, y \in [-R, R]$.

2. If the point is inside the circle ($x^2 + y^2 <= R^2$) then increment the hit counter, M, by 1.

3. Continue picking until N random points are chosen.

4. Compute the approximation of π: $\pi' = 4 * M/N$.

Obviously, the error between the real value of π and the approximation will depend on the value of N, but it will also depend on the random numbers that are picked.

The user has control over N, but, of course, has no control over the random numbers. This fact will return as one of the disadvantages of the MC method. But, before looking at that, it is interesting to look at the results of the π calculation (Figure 3). As already stated, the error of π' does depend on N, and, furthermore, it depends on N in a log-linear way. To get 10 times the accuracy (or one significant digit), the MC method needs 10 times as many random points, again, another disadvantage. The Newton iteration method can calculate π with quadratic convergence (halving the error for each iteration). The MC method, on the other hand, converges very slowly. This brings up one of the major points of MC. The MC method does guarantee that the result *will* converge to the answer; however, it does not guarantee how long it will take. The π calculation result graph shows this important "feature" of MC. The upper and lower bound error bars show the range of values that the simulations achieved, while the center line shows the average error of the runs. Note that this graph includes results from many simulation runs (remember the uncontrollable random numbers), so that the error bars can be computed.

With all of these disadvantages, it seems like the MC method is useless, but it is not. Although it may be hard to see from this example, there is one big advantage to the MC method: the algorithm to compute π is simple. Almost anybody can understand it and it is very simple to write a simulator for it. Other methods for computing π are significantly better in accuracy and speed; however, they require either an in-depth knowledge of geometry or calculus. So, for this example, the MC method may not be the best idea. When a significantly more complicated equation needs to be solved (like the BTE), the MC method can solve it with very few simplifying

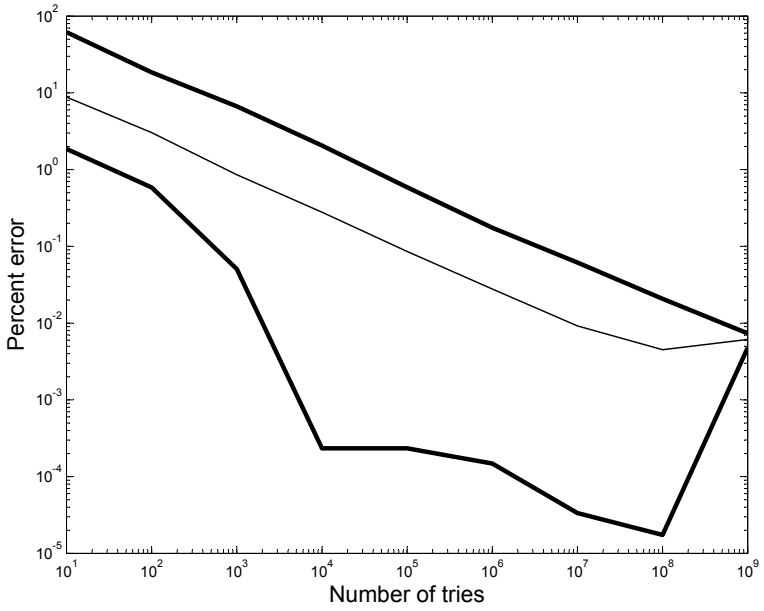

Figure 3: The Monte Carlo results from the computation of an approximation to π. This is the result of 100 simulation runs. The upper and lower bold lines bound the results, while the center line is the average of them all.

assumptions.

2.3.2 Monte Carlo and the Boltzmann Equation

The MC simulation of the BTE is much the same as in the π example, just on a larger scale. And, although a rigorous mathematical proof exists that proves the MC method provides convergence to the integro-differential BTE, it is beyond the scope of this work. The proof exists for the interest of the reader [67]. A clearer way to understand the MC method as applied to the BTE is to analyze the algorithm physically. All of the electrons simulated during an MC simulation follow strict first-principles physics (at least in a classical way). This can provide much insight into the physics behind a material and a device. On the other hand, the drift-diffusion and hydrodynamic methods hide much of the microscopic physics behind coupled differential equations.

The MC method of solving the BTE is an exact solution [33]. The only limit to its accuracy is the amount of first-principles physics included in the model (and numerical errors). The major advantage over the method of moments is the fact that the carrier-scattering mechanisms are included; there is no relaxation time approximation. This becomes very important when analyzing the high energy tail of a carrier distribution.

The basic idea of solving the BTE with MC is literally to trace the trajectory of the particles. The particles (electrons in this research) are traced through all of their six dimensions (three in real space, three in wave-vector space). By following a particle (or an ensemble of them) over a long period of time, macroscopic information can be statistically evaluated from the microscopic estimators. For instance, in a simulation of bulk GaAs, 10,000 electrons are simulated for 5 ps. During the simulation, each electron's energy is recorded at each discrete time step, and when the simulation concludes, the average energy for the ensemble can be calculated. That is the simulation method: trace the particles through a material (or a device), record their microscopic estimators, and then compute the macroscopic variables from those values.

So, the high-level overview for the simulator (not including the device effects described in Chapter 4) has just two steps, repeated many times:

1. Drift the electron(s) according to classical, Newtonian physics.

2. Potentially scatter the electron(s).

Of course, the actual MC simulator has many more steps than just two, and each of the steps is fairly complicated, but the basic idea is summed up in those two global

steps. The next chapter delves deeper into the MC simulator, including inputs to the simulator and the actual algorithms used.

CHAPTER III

THE MONTE CARLO MODEL

This chapter gives the details of the MC model for bulk semiconductor materials, saving the device-specific information until Chapter 4. Even in a device MC simulator, the solution of the BTE is the same as that in the bulk simulator, so this chapter is applicable to both the device simulator and the bulk simulator. The overview of a complete material-theory-based model is shown in Figure 4; however, not all parts of it are used in this simulator. This simulator follows the bold path and contains modules/programs for the bold boxes. The remaining boxes and paths are either alternative solutions or higher-order phenomena that are not included in this work.

First, the three major inputs to the simulator are described: the material parameters, the band structure, and the scattering rates. These inputs are of monumental importance, and the accuracy of the simulator is almost exclusively limited by them. Finally, the actual equations of motion and the simulation algorithms are described in detail.

3.1 The Material Parameters

This work focuses on three materials (all cubic-phase): zincblende-phase gallium nitride (ZB-GaN), cubic-phase silicon carbide (3C-SiC), and gallium arsenide (GaAs). Basic material parameters and band structure form factors (described later) are

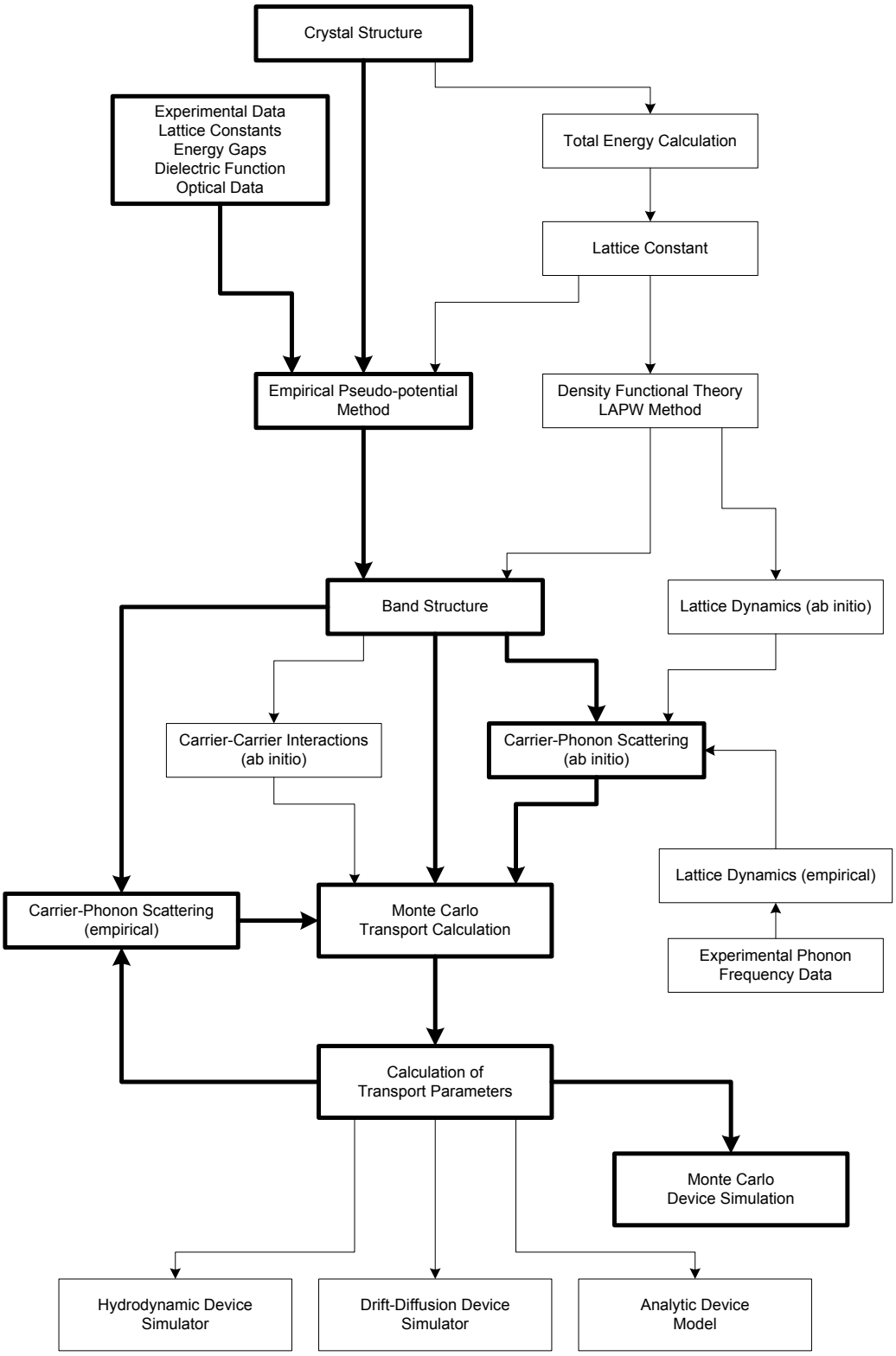

Figure 4: The schematic chart for the material-theory-based modeling technique.

Table 1: The material parameters for GaAs, 3C-SiC and ZB-GaN.

	GaAs	3C-SiC	ZB-GaN
Lattice constant (Å)	5.65	4.35	4.50
Bandgap (eV)	1.42	2.20	3.20
Static relative permittivity	13.18	9.72	9.50
Optical relative permittivity	10.89	6.52	5.35
Density ($\frac{g}{cm^3}$)	5.36	3.17	6.10
Sound velocity ($10e6\frac{cm}{s}$)	0.522	0.644	0.457
Interband acoustic deformation potential (eV)	17.0	8.0	12.0
Intraband acoustic deformation potential (eV)	11.0	14.0	12.0
Optical deformation potential field ($10e9\frac{eV}{cm}$)	0.21	1.3	1.0
Optical phonon energy (meV)	35.36	120.0	92.0

needed for each material. All of the material parameters for the materials are given in Table 1 [68].

3.2 The Electronic Band Structure

The band structure of a material defines the possible electron energy values in the crystal lattice; it is split up into bands, and, given a band number, ν, and a wave-vector, $\boldsymbol{k}$, the band structure defines the function $E_\nu(\boldsymbol{k})$. Because the band structure is the first input into the MC model, and all of the future steps depend on it, the accuracy of it is extremely important, especially at high energies where material breakdown occurs. There are multiple ways of computing a band structure; two methods will be highlighted.

3.2.1 Analytic Method

An analytic band structure is the simplest method of defining a band structure. It assumes that the band structure's energy surfaces are perfect spheres. The simplest model is a single-valley, parabolic band structure. The parabolic band is described

by the energy-wave vector relationship in Eq. 6, and it is completely characterized by the semiconductor's effective mass.

$$E(\boldsymbol{k}) = \frac{\hbar|\boldsymbol{k}|^2}{2m^*} \tag{6}$$

A single-valley, parabolic band structure is vastly inaccurate at all but the smallest carrier energies and therefore is valid only under small applied electric fields. To start with, this band structure cannot reproduce the negative differential region (NDR) found in many semiconductor materials. The NDR region is the section of the velocity field curve where the velocity drops, usually found in direct materials. The reason for the drop in velocity is the movement of the electron distribution to the upper valleys (L and X) from the low-energy valley Γ. The electron mass is much larger in the L and the X valley than it is in the Γ valley, so the velocity of the distribution falls. To capture that effect, additional valleys must be incorporated. For instance, in GaAs, it is common to have a three-valley model using the effective mass approximations to include three valleys: Γ, X, and L. By adding the extra higher-energy valleys, the NDR region of the velocity-field curve can be reproduced; however, any fields beyond that quickly become inaccurate.

An extension to the parabolic band structure that increases the accuracy to slightly higher energies is the non-parabolicity factor. By including a non-parabolicity factor, α, in each of the valleys (Eq. 7), the accuracy at the high-energy end of valleys becomes a little better [69]. However, the accuracy is still insufficient to analyze very

high energy effects like impact-ionization effects and device breakdown.

$$E(\boldsymbol{k})(1+\alpha E(\boldsymbol{k})) = \frac{\hbar|\boldsymbol{k}|^2}{2m^*} \tag{7}$$

In addition to the energy-accuracy problems, simulators that employ multiple valley band structures have to include additional non-physical phonons that pose problems that will be described later.

3.2.2 Empirical Pseudo-potential Method

A significantly better method for computing "real" band structures is the empirical pseudo-potential method (EPM). The EPM computes the band structure by calculating the pseudo-potential that repels the electrons from the core region. These pseudo-potentials can then be used in the nearly-free electron problem to obtain a band structure for the material [53]. The empirical section of the EPM uses experimental data such as energy gaps, dielectric response, and effective masses to fit the pseudo-potentials. The result is a very accurate band structure based on real-world measurements.

The band structures used in this work were created with the EPM using the latest experimental findings. This ensures that utmost accuracy is obtained in what amounts to the most important data in the modeling technique. Figure 5 shows the result of an EPM calculation of GaAs. This figure shows the GaAs band structure that is used in all scattering rate calculations, bulk simulations, and device simulations.

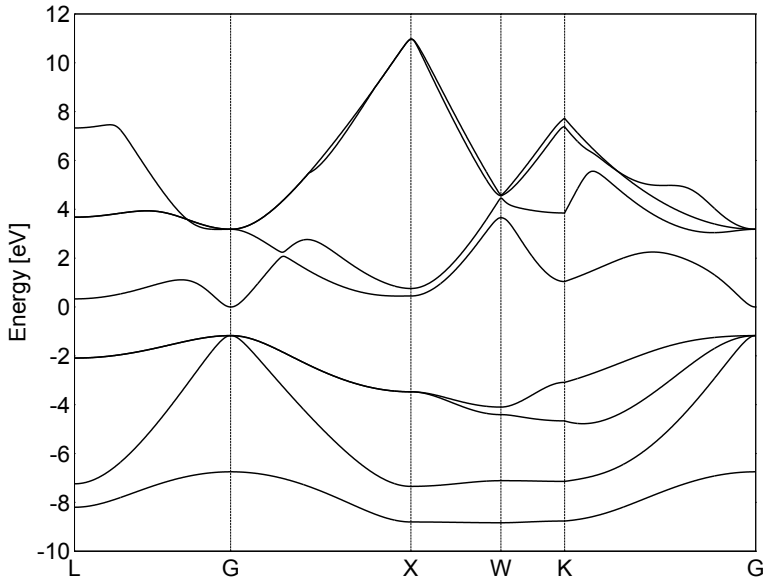

Figure 5: The band structure for GaAs. This band structure is computed using the EPM technique. It includes the first four conduction bands and the first four valence bands.

3.3 The Carrier Scattering Rates

The carrier scattering rates define the particle-phonon interaction probabilities. The scattering rates (and the distribution's reaction to them) complete an exact solution[1] to the collisions term of the BTE: $\left(\frac{\partial f}{\partial t}\right)_{scatterings}$. Scattering mechanisms affect the particle distribution, $f(\boldsymbol{k}, \boldsymbol{r}, t)$, in two ways. First, the scattering rates define the per-unit-time probability of the distribution changing, and, second, the reaction of the particle to the scatter provides the actual change to the distribution.

The calculation of scattering rates starts with Fermi's golden rule:

$$S(\boldsymbol{k}, \boldsymbol{k'}) = \frac{2\pi}{\hbar} \left| \langle \psi_{\boldsymbol{k}} | H_p | \psi_{\boldsymbol{k'}} \rangle \right|^2 \delta(E(\boldsymbol{k'}) - E(\boldsymbol{k})), \tag{8}$$

[1] As exact a solution as the included physics to calculate the scattering rates and the reactions allow.

where $S(\boldsymbol{k}, \boldsymbol{k'})$ is the probability (per-unit-time) of a scattering event between a particle with momentum $\boldsymbol{k}$ and a particle with momentum $\boldsymbol{k'}$. Basically, Fermi's golden rule says that a scatter must satisfy energy conservation (the delta function) and that the probability is based on the interaction between the quantum states of the particles. Fermi's golden rule, however, is only the starting point; the first extension is to integrate over all final states to get a cumulative rate, expressed as the inverse of the scattering time, for a single initial state:

$$\frac{1}{\tau(\boldsymbol{k})} = \frac{V}{(2\pi)^3} \int_{BZ} S(\boldsymbol{k}, \boldsymbol{k'})\, d\boldsymbol{k'} \tag{9}$$

Finally, the interaction, H_p, must be defined for each of the scattering mechanism types: non-polar optical, polar optical, acoustic, impurity, and impact ionization.

Traditionally, MC simulators use a valley scheme for computing the scattering rates. For instance, it is common to confine polar-optical phonon scattering to the Γ valley since it is most active there. This simulator, however, does away with the concept of valleys altogether. In a full-band simulator, valleys are artificially defined areas of a band structure, which add no useful value to a full-band simulator. For example, with simulators that use valleys, intra- and inter-valley scattering rates are calculated so particles can travel between the valleys. These mechanisms are non-physical so, by definition, they must be empirically determined from the MC bulk simulation. This, however, would add more fitting parameters, which this research

tries to avoid. A smaller number of fitting parameters achieves greater flexibility for simulating novel semiconductors since the simulator is less reliant on experimental data.

With the elimination of valleys, each scattering rate is treated equally throughout the energy range of the material. This, however, does not eliminate the correct assumption that polar-optical phonons are most active in the Γ valley; this fact is preserved by the relative strengths of the scattering rates in this valley, but, by allowing polar-optical scattering over the entire range of energies, we have relaxed a simplification that is common in previous MC simulators.

In the following sections, each of the mechanisms is examined and the scattering rate equation for that mechanism is given (without derivation). Detailed information about scattering rate calculations can be found in Ridley [70], Fawcett, Boardman and S. Swain [46], or Brennan [69].

3.3.1 Non-Polar Optical Phonons

An optical phonon is the quantum of lattice vibration that occurs when the ions in a crystal oscillate in opposition. Specifically, a non-polar optical phonon is an optical phonon where ions of approximately the same charge oscillate. Although the dispersion relation for these phonons is non-constant, it is generally assumed to be constant. It is the simplest scattering rate to compute because it has a constant phonon energy and it has no dependence on the phonon wave vector, q (Eq. 10).

$$\frac{1}{\tau_{NP}} = \left(\frac{\pi(D_t k)^2}{(2\pi)^3 \rho \omega_{NP}}\right)\left[N_{op} + \frac{1}{2} \pm \frac{1}{2}\right] \times \sum_{IW} I(\boldsymbol{k}, \boldsymbol{k'})\delta[E_f - E_i \pm \hbar\omega_{NP}]\Delta^3\boldsymbol{k}, \tag{10}$$

where $\frac{1}{\tau_{NP}}$ is the non-polar scattering rate, $D_t k$ is the non-polar deformation potential, ρ is the density of the material, $\hbar\omega_{NP}$ is the non-polar optical phonon energy, N_{op} is the occupation number, $I(\boldsymbol{k}, \boldsymbol{k'})$ is the overlap between the initial and final k-point, E_f is the energy of the destination k-point, E_i is the energy of the initial k-point, and $\hbar\omega_{NP}$ is the energy of the non-polar phonon.

Figure 6 results from the computation of the non-polar scattering rate in GaAs, 3C-SiC, and ZB-GaN. Note that since all of these materials are quite polar (as compared to Si), the non-polar optical scattering rate is fairly small, and in fact plays virtually no role in the simulation.

3.3.2 Acoustic Phonons

An acoustic phonon scattering rate has the form of a deformation potential. An acoustic phonon occurs when the ions in a crystal vibrate in the same direction. This is the most complicated rate to compute because of the non-constant phonon dispersion relation ($\omega(q)$). In the non-polar optical scattering, the phonon dispersion was close enough to a constant that the assumption was warranted. The dispersion relation for acoustic phonons is not regarded as a constant. Although the true acoustic dispersion relationship can be computed by means of the adiabatic bond-charge model, this process is complicated (e.g., [71]). In addition, for the novel materials analyzed in

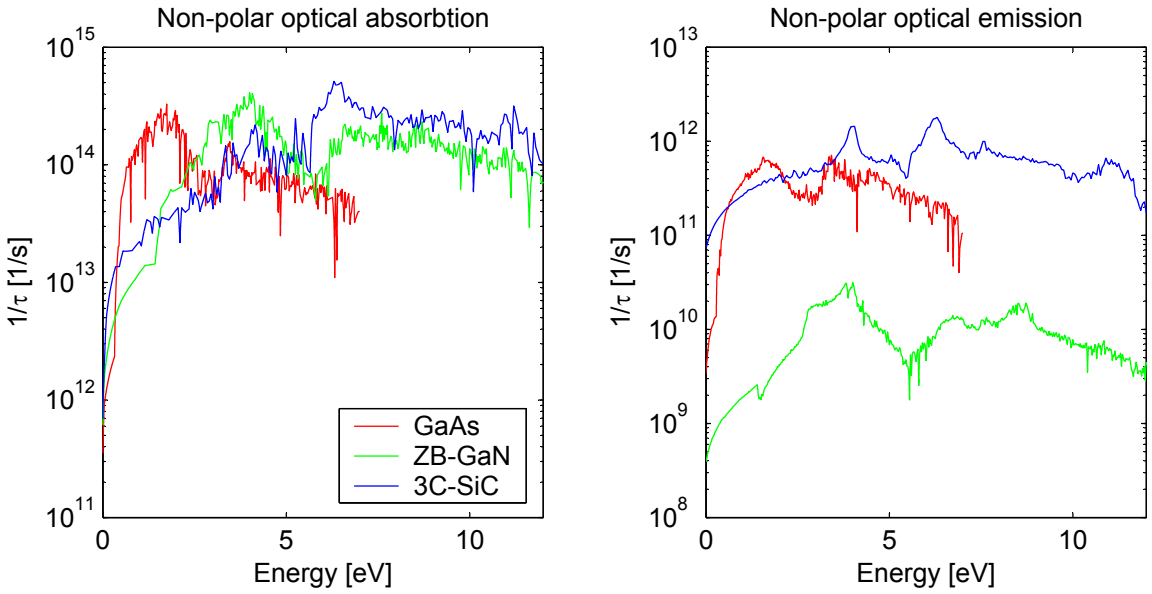

Figure 6: The non-polar optical scattering rate for GaAs, ZB-GaN, and 3C-SiC. It includes both absorption and emission.

this work, the extensive parameters needed for the bond-charge model are generally unavailable. So a simple dispersion relation is used, Eq. 11 and Eq. 12 [48].

$$\omega(\boldsymbol{q}) = \begin{cases} \omega_{max}\sqrt{1-\cos\left(\frac{|\boldsymbol{q}|a}{4}\right)} & |\boldsymbol{q}| < 1.0, \\ \omega_{max} & \text{else.} \end{cases} \tag{11}$$

$$\omega_{max} = \frac{4v_l}{a}, \tag{12}$$

where a is the lattice constant of the material, $\boldsymbol{q}$ is the phonon's wave-vector, and v_l is the longitudinal velocity in the crystal. This dispersion relationship uses only basic material parameters that are readily available, and it reproduces the actual

relationship fairly well, although there has been some concern with this formula at high $\boldsymbol{q}$ [48].

In addition to the acoustic phonon dispersion relation, the acoustic scattering rate requires an acoustic deformation potential that varies over the entire Brillouin Zone (BZ). The deformation potential, like the phonon dispersion, can be computed numerically; however, this adds significant complexity to the computation. One of the main problems with numerical acoustic deformation potentials is the amount of data (and computation) required. A different deformation potential is used for interactions between each initial and final k-point, so the number of deformation potentials (for a k-dependent calculation) is the number of k-points squared divided by two. Each of these potentials has to be computed from a bond-charge model (like the phonon dispersion). Again, for the materials in this work, the experimental values are not available. Details about the choice of the deformation potential will be discussed later.

With the acoustic dispersion relation, the derivation of the acoustic phonon scattering rate can be completed (Eq. 13).

$$\begin{aligned}\frac{1}{\tau_{AC}} = \left(\frac{\pi E_1^2}{(2\pi)^3\rho}\right)\sum_{IW}\frac{|\boldsymbol{q}|^2}{\omega(\boldsymbol{q})}\left[N(\boldsymbol{q})+\frac{1}{2}\pm\frac{1}{2}\right] \\ \times I(\boldsymbol{k},\boldsymbol{k'})\delta[E_f - E_i \pm \hbar\omega(\boldsymbol{q})]\Delta^3\boldsymbol{k},\end{aligned} \tag{13}$$

where $\frac{1}{\tau_{AC}}$ is the acoustic scattering rate, E_1 is the acoustic deformation potential, $\boldsymbol{q}$ is the phonon's wave-vector, ρ is the density of the material, $N(k)$ is the occupation number, $I(\boldsymbol{k},\boldsymbol{k'})$ is the overlap between the initial and final k-point, E_f is the energy

of the destination k-point, E_i is the energy of the initial k-point, and $\hbar\omega(\boldsymbol{q})$ is the energy of the acoustic phonon.

The reason the acoustic scattering rate takes so much computational power is that the results of the energy conservation delta are not known. Without knowing $\boldsymbol{q}$ it is not possible to determine if energy conservation holds; however, using energy conservation was the way to determine $\boldsymbol{q}$ for both the non-polar optical and polar optical rates. This paradox is solved by taking the maximum possible acoustic phonon energy ($E_{ph,max}$) and assuming that all phonon energies less than that are possible final states. So, with an initial k-point of energy E_i, all final k-points with energies between E_i and $E_i \pm E_{ph,max}$ are assumed to satisfy energy conservation initially. Now there is a list of potential final k-points (no other k-points are available because the phonon energy would not be large enough) and $\boldsymbol{q}$'s can be computed. Finally, with a $\boldsymbol{q}$, it is possible to compute the phonon energy from the dispersion relation, and the true energy conservation is determined. As a result of this algorithm, many more potential final-states are available than in either non-polar optical or polar optical, so the computation takes much longer.

Figure 7 shows the results from the computation of the acoustic scattering rate in GaAs, 3C-SiC, and ZB-GaN.

3.3.3 Polar Optical Phonons

A polar optical phonon mainly occurs in ionic semiconductors. It is similar to a non-polar optical phonon; however, in actuality, a polar optical phonon can occur in either the optical mode or the acoustic mode. The polar optical rate is dependent on

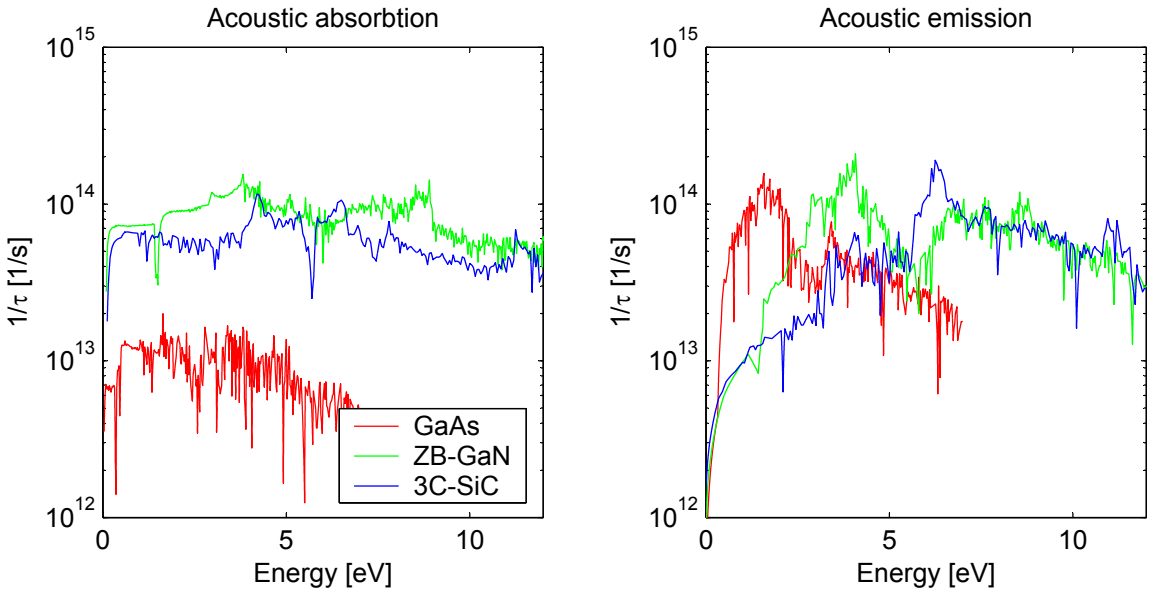

Figure 7: The acoustic scattering rate for GaAs, ZB-GaN, and 3C-SiC. It includes both absorption and emission.

the polarity of the material. Again, it is a fairly simple scattering rate to compute because the phonon energy is assumed constant, but since the rate depends on the phonon wave vector, the computation of the rate takes longer than that for non-polar optical. The equation for the non-polar optical scattering rate is shown in Eq. 14.

$$\frac{1}{\tau_{PO}} = \left(\frac{2\pi}{a}\right)\left(\frac{q\omega_{op}}{8\pi^2}\right)\left(\frac{1}{\epsilon_\infty} - \frac{1}{\epsilon_0}\right)\left[N_{op} + \frac{1}{2} \pm \frac{1}{2}\right] \times \sum_{IW} \frac{1}{|\boldsymbol{q}|^2} I(\boldsymbol{k}, \boldsymbol{k'})\delta[E_f - E_i \pm \hbar\omega_{OP}]\Delta^3\boldsymbol{k}, \tag{14}$$

where $\frac{1}{\tau_{PO}}$ is the polar optical scattering rate, a is the lattice constant of the material, $\boldsymbol{q}$ is the phonon's wave-vector, ω_{op} is the polar-optical phonon frequency, ϵ_∞ is the optical permittivity, ϵ_0 is the static permittivity, N_{op} is the occupation number, $I(\boldsymbol{k}, \boldsymbol{k'})$ is the overlap between the initial and final k-point, E_f is the energy of the

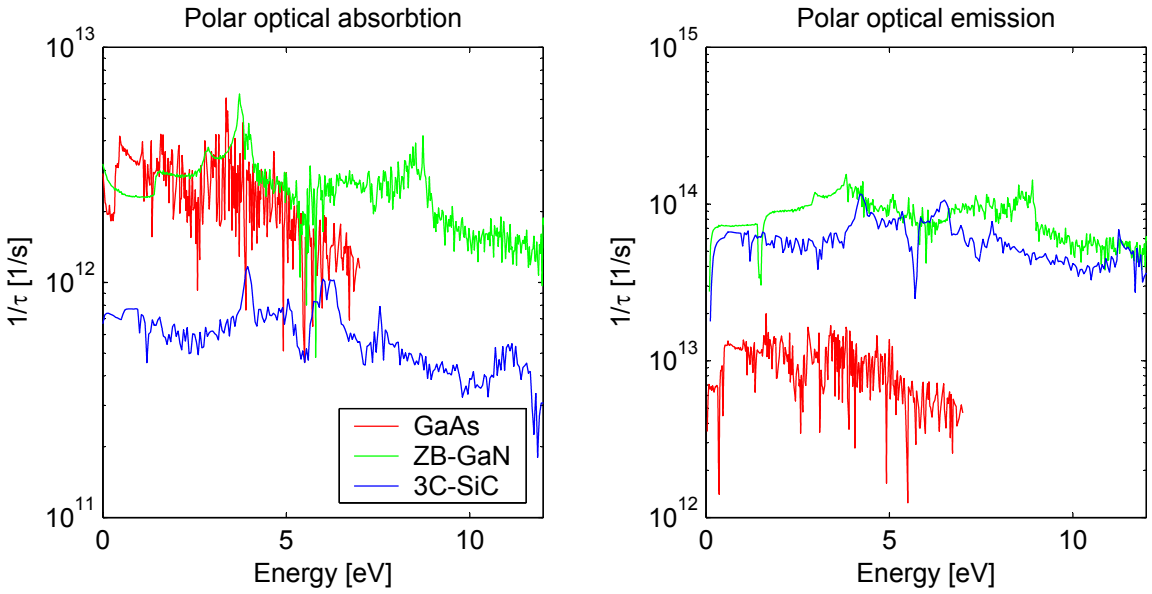

Figure 8: The polar optical scattering rate for GaAs, ZB-GaN, and 3C-SiC. It includes both absorption and emission.

final k-point, E_i is the energy of the initial k-point, and $\hbar\omega_{OP}$ is the energy of the polar-optical phonon.

Figure 8 results from the computation of the polar scattering rate in GaAs, 3C-SiC, and ZB-GaN. Note that since all of these materials are polar, the polar optical scattering rate is large, and at low energy is the dominant scattering mechanism.

3.3.4 Impurity Scattering

Semiconductor materials contain impurities, whether placed intentionally, as with doping in a device, or unintentionally, from impure materials. Whatever the cause, these impurities disrupt the periodic potential throughout the crystal. When an electron traveling through the crystal passes near these impurities, it is scattered by the deformed potential. This scattering is called impurity scattering.

Impurity scattering is an elastic collision. The deflection of the electron by the

impurity causes no energy loss or gain, but merely changes the electron's momentum (or wave vector). For the ionized impurity scattering mechanism, the scattering source can be simplified as a screened Coulomb potential.

In this work, the impurity scattering is not computed numerically. Instead, a simple analytic approximation is used because of both the complexities of the impurity scattering rate and its limited active region. The analytic scattering rate used in this research is shown in Eq. 15 (the Brooks-Herring formulation [62, 72]).

$$\frac{1}{\tau_{IMP}} = \left(\frac{2\pi N_f Z^2 q^4 N(E_k)}{\hbar \epsilon_s^2} \right) \frac{1}{q_D^2 (2k^2 + q_D^2)}, \tag{15}$$

where N_f is the ionized impurity concentration, q is the impurity phonon's wave-vector, E_k is the electron energy, ϵ_s is the static permittivity, q_D is the inverse Debye length, and $N(E_k)$ is the density of states at energy E_k.

Since the impurity scattering rate is highly dependent on the doping levels, the device simulator contains a separate impurity scattering rate for each of the doping sections in the device.

Figure 9 results from the computation of the impurity scattering rate in GaAs, 3C-SiC, and ZB-GaN. All of these rates are calculated with an impurity concentration of $1 \times 10^{17} cm^{-3}$.

3.3.5 Impact Ionization

Impact ionization is not strictly a scattering rate, it is a generation and recombination process. However, it does fall under the same model (time-dependent rate), so it is

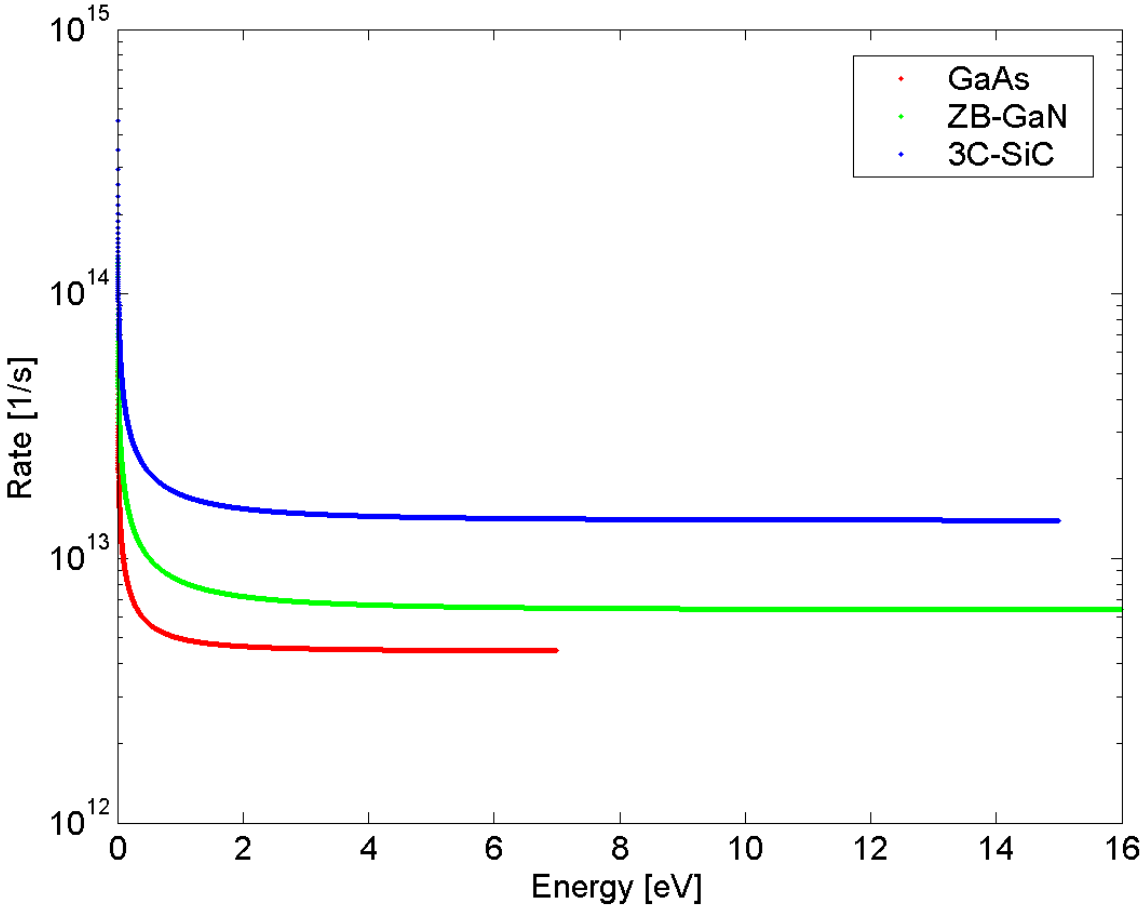

Figure 9: The impurity scattering rate for GaAs, ZB-GaN, and 3C-SiC. The results are for an ionized doping concentration of $1 \times 10^{17} cm^{-3}$.

included in the scattering rate calculations in the simulator. An impact ionization event occurs when a high-energy electron collides with the crystal lattice, transferring its energy to an electron in the valence band. The result is a new electron in the conduction band, a new hole in the valence band, and the initiating electron's reduced energy. Unlike the scattering rates, impact ionization has no effect on the lattice and produces no phonons. Impact ionization is a high energy process. The starting energy of impact ionization must be greater than that of the bandgap (or else the initiating electron would not have enough energy to promote a bound electron to the conduction band). Beyond the bandgap, it quickly becomes the dominant scattering rate. The impact ionization is so high at large energies as to prevent the run-away of electron energies. Whenever an electron has too much energy, it impact ionizes to reduce the energy. Impact ionization is the most important interaction at high energies, and it is completely responsible for device breakdown.

Since impact ionization is not a scattering rate *per se*, the computation is completely different from that for the phonon-interaction rates. Impact ionization involves the interaction among two electrons and a hole. First, the initial electron must be above the bandgap in energy. Then, the first electron, second electron, and the hole must satisfy energy conservation among them. Finally, all of the particles together must satisfy momentum conservation. So, impact ionization ends up being a triple integral over the entire BZ. This is infeasible to compute directly, so a Monte Carlo integration technique is used instead. A grid spacing of $0.05a$ in k-space is used for locations to compute the rate, so only 916 points per band are computed in the final rate. All of these simplifications allow a computationally tractable solution. Details

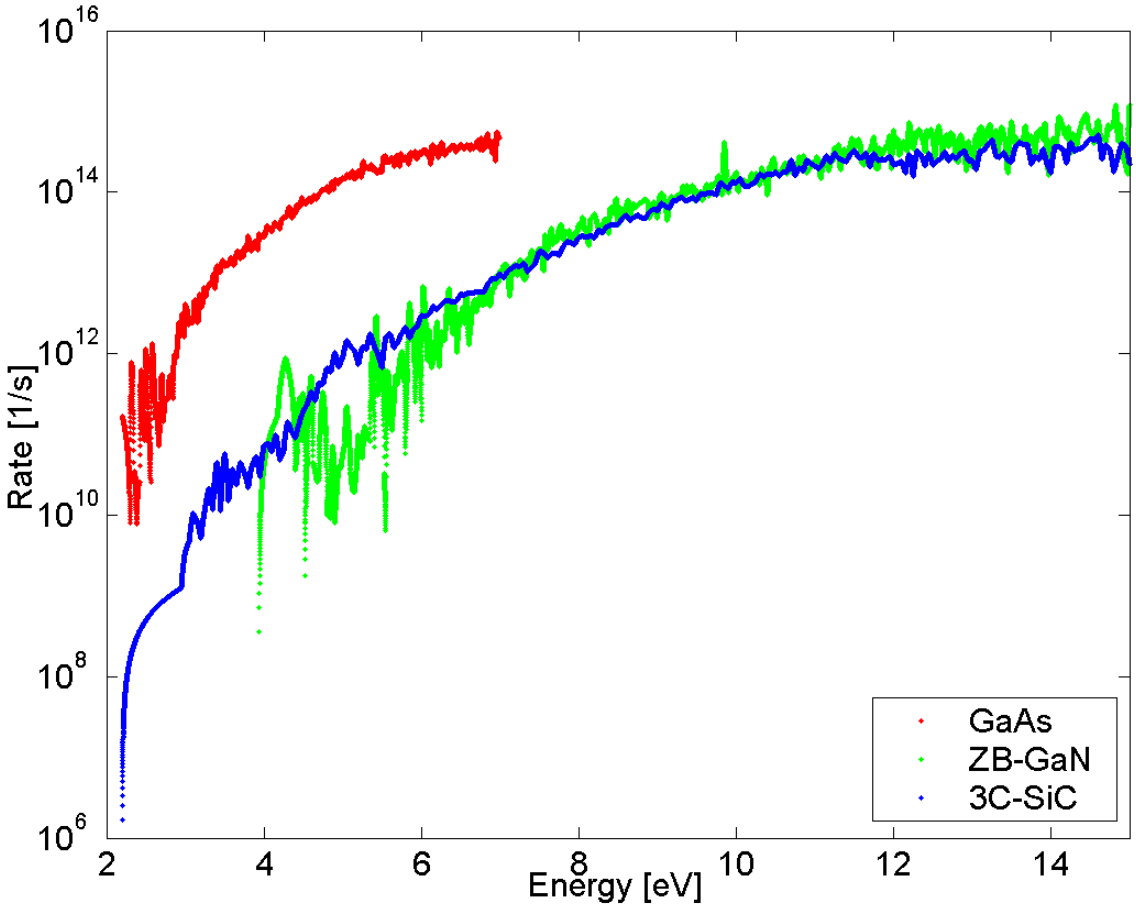

Figure 10: The impact ionization rate for GaAs, ZB-GaN, and 3C-SiC.

of both the derivation and computation of impact ionization can be found in many papers [15, 24, 34, 40, 43, 57, 58, 60, 63, 73, 74].

Figure 10 shows the results from the computation of the impact ionization rate in GaAs, 3C-SiC, and ZB-GaN.

3.3.6 Scattering Rate Convergence

As mentioned previously, a scattering rate is computed by choosing an initial k-point and integrating over all of the final k-points in the BZ. Since the k-points in the BZ

are discretized, and there is no formula that can represent the complexities of a empirical band structure, the integral must be simplified to a sum over k-points in the BZ. The question of how fine an integration grid is needed hinges on the convergence of the scattering rate. There are two variables that contribute to the scattering rate convergence: the k-point grid resolution and the energy delta. Since the energy band structure is discretized, the delta function found in all of the scattering rate calculations (which represents energy conservation) cannot be solved exactly, therefore an approximation must be made. Since the energy delta function mathematically defines that the initial and final energies must be exactly the same, the computation of the energy delta function must be looser. So we define the parameter, ΔE, which defines a range of energies that are accepted for the energy conservation delta function.

By combining these two unknown variables, the k-point integration grid and the energy delta size, the polar-optical rate at $\boldsymbol{k}_i = [0, 0, 0]$ in GaAs is computed, and Figure 11 is generated. This graph illustrates the convergence of the scattering rate. Notice that as the integration grid spacing is reduced, the scattering rate converges to the correct value. We found that to achieve proper convergence of fully-numerical scattering rates, a much finer integration grid is needed than has been previously used. The scattering rates for this simulator use an integration grid of $\Delta k = 0.0005\frac{2\pi}{a}$, while many previous fully-numerical simulators use integration grids as big as $0.02\frac{2\pi}{a}$. The obvious drawback with using such a fine grid is an increase in computation time for the calculation. Scattering rate calculations are slow and can take as long as a week to complete.

It is interesting to note that once convergence has been achieved by using a fine

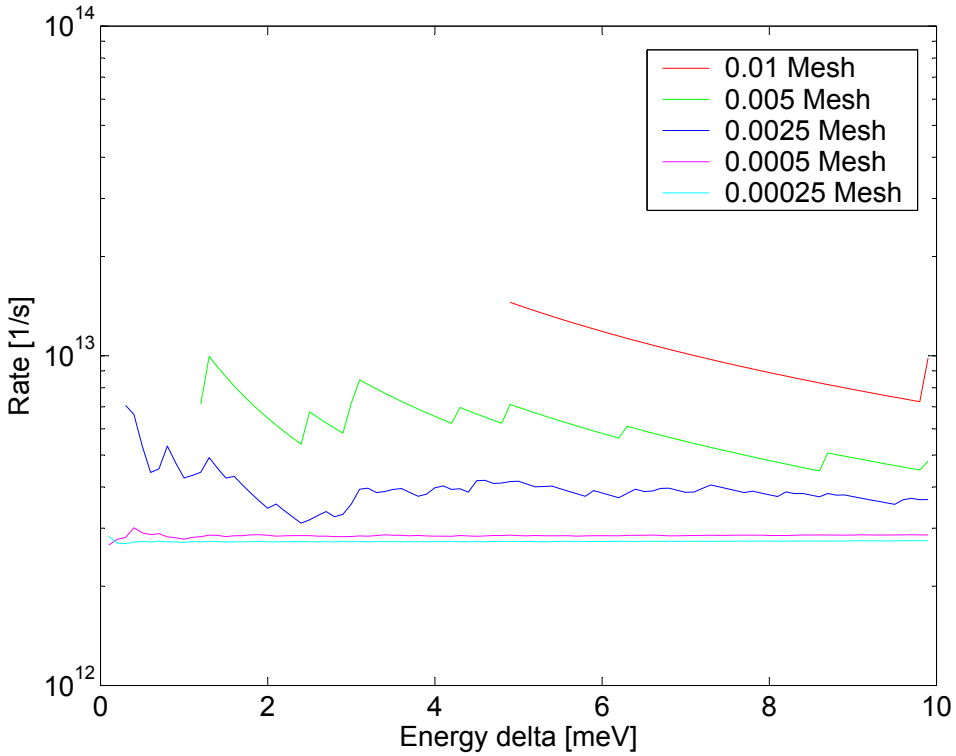

Figure 11: The scattering rate convergence test for polar-optical phonons in GaAs. All computations are made at Γ. Both the integration grid size, Δk, and the energy delta are varied as shown in the graph.

enough integration grid, the energy delta plays little role in determining the scattering rate. This is because as the energy delta is increased, there is convergence to the actual scattering rate; however, to see the effect of non-convergence due to the energy delta, it would have to be set very small (smaller than the values in this work). Since the energy delta plays little role in determining the scattering rate (once convergence is achieved), a small energy delta, $\Delta E = 0.0005$ eV, is used because the fewer the points that satisfy the energy conservation, the faster the computation is. Of course, if the energy delta is too small, then, potentially, no final state points could be found, so the energy delta is not made smaller.

To complete the convergence analysis, since the previous result was the scattering

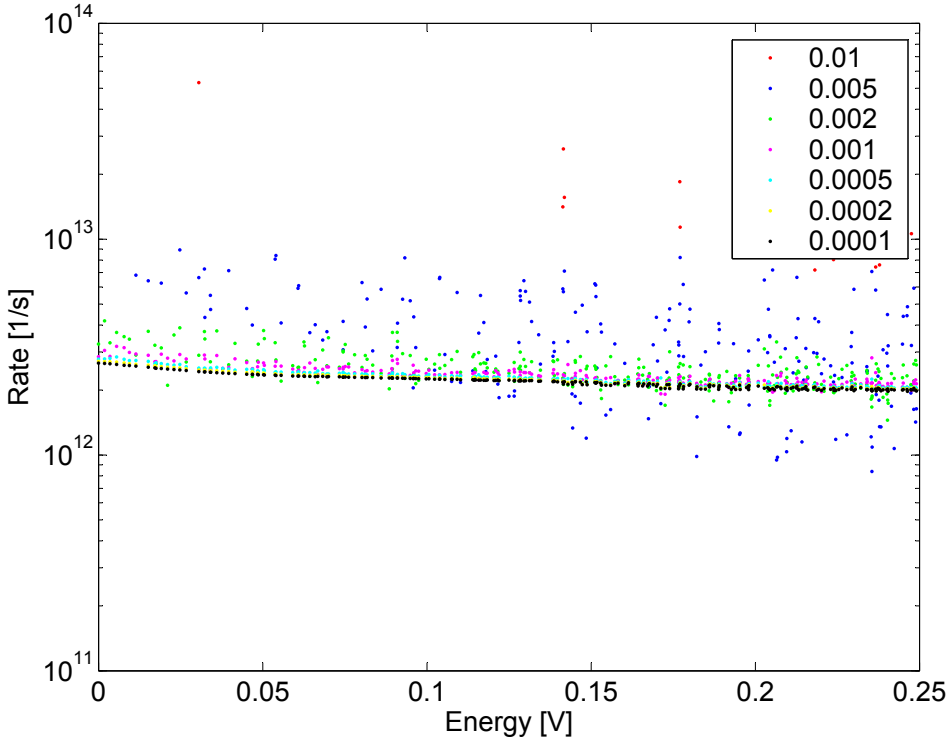

Figure 12: The second scattering rate convergence test for GaAs polar-optical phonons. For this graph, the energy delta is held constant ($\Delta E = 0.0005$ eV) and the rate is computed for about 100 k-points for varying grid sizes.

rate for only one k-point, the scattering rate is calculated for many k-points. Now, the energy delta remains constant at $\Delta E = 0.0005$ eV, and the rate for about 100 k-points is calculated using the different integration grids. This graph (Figure 12) verifies that the convergence at the fine integration grids remains valid at many initial k-points, so we assume that the convergence is achieved for all k-points in the Irreducible Wedge (IW).

3.3.7 Acoustic Deformation Potential

The focus of this work is the analysis of novel semiconductors with little experimental data. To this end, the fitting parameters in this work are few. The addition of more fitting parameters can increase the accuracy of the results; however, each additional

fitting parameter requires more experimental or modeling results. So to limit the dependence on previous work, the number of fitting parameters is kept to two. Both parameters are acoustic deformation potentials.

The difference between the two deformation potentials is the bands on which they operate. The first acoustic deformation potential is used for interactions between states (initial and final) in the first conduction band. The second deformation potential is used for all other interactions (e.g. first and second band, second and third band, etc.) Of course the real deformation potential varies over the entire BZ, so for each initial and final state there is a different deformation potential; however, we have found that these two values are used to adjust the results at both high and low energies. Using only one deformation potential for all interactions does not provide enough flexibility.

3.3.7.1 Acoustic Deformation Potential Calculation

The deformation potentials are chosen by running the bulk simulation for several combinations of potentials [65]. In general, the deformation potential can be guessed fairly accurately without any simulations (they are generally $\approx$ 10 eV). Therefore values are taken above and below that. Then, the bulk simulation is run (at both low fields and high fields) for each combination of the deformation potentials (generally 5 potentials are selected, so 25 simulations are run). Then the velocity field (low-energy) and the impact ionization coefficients (high-energy) results are compared to both experimental data and previous simulation work. The deformation potential for the closest set of results is used for further bulk work and device simulations.

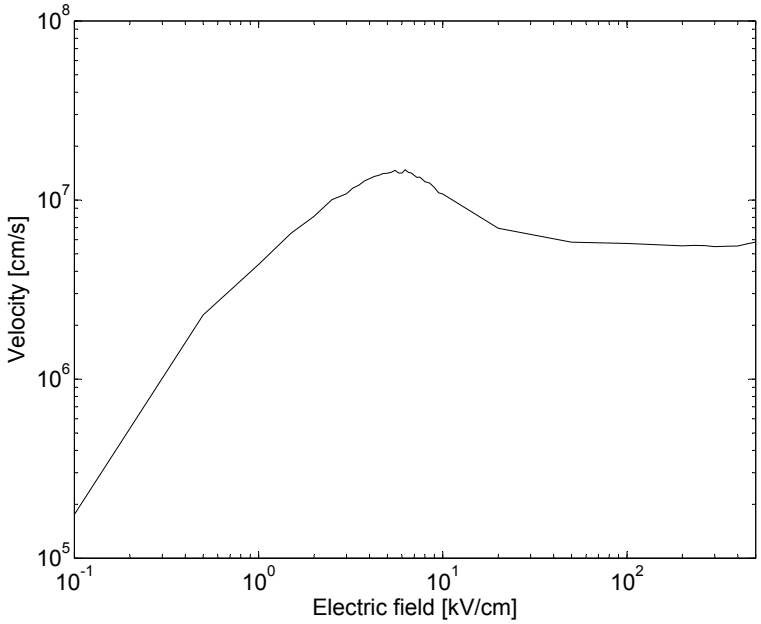

Figure 13: The velocity field curve for GaAs after the two acoustic deformation potential fitting parameters were chosen.

For example, in GaAs, the range of acoustic deformation potentials that were examined for the intraband acoustic deformation potentials was 12-20 eV, and the interband potentials were 2-20 eV. The results for the velocity field curve are shown in Figure 13 and the impact ionization coefficients are shown in Figure 14.

3.4 The Simulator Algorithms

The flow of the MC bulk simulator is, on the surface, simple (Figure 15). There are three basic inputs that set up the simulator for a specific material: the material parameters, the band structure, and the scattering rates. Next, the initial distribution of particles is created, the interpolation data structures are created and the simulation is ready to start. The whole simulation is split into two loops: the time loop and the particle loop. The time loop moves the simulation through time, and the particle loop does the single-step MC simulation for each particle in the ensemble. For each

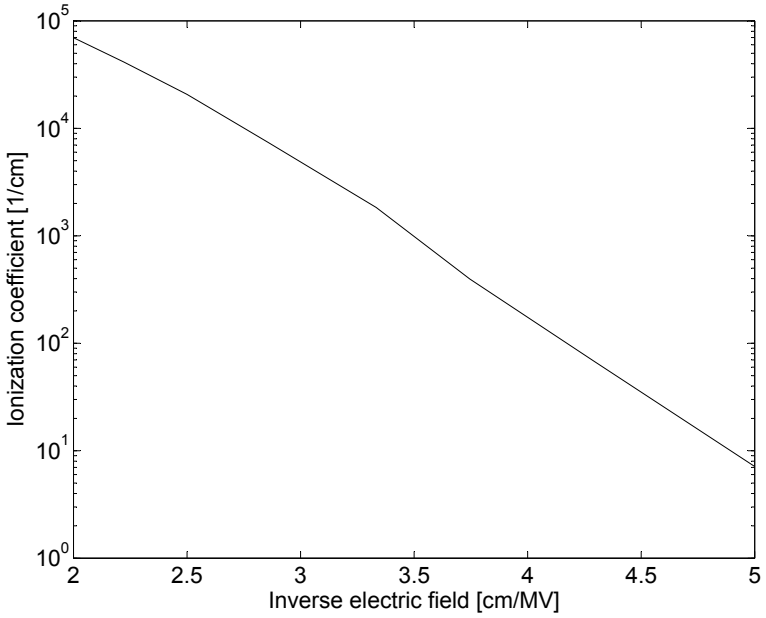

Figure 14: The impact ionization coefficients for GaAs after the two acoustic deformation potential fitting parameters were chosen.

particle, at each time, the particle is drifted, data is collected from the particle and a scatter-try occurs. This continues throughout the simulation. When the simulation completes, some analysis of the estimators is performed, but most of the analysis occurs post-simulation. This completes the overview of the MC bulk simulator. In the following sections, each of the modules mentioned will be examined in detail.

3.4.1 Interpolation Schemes

Since the functions and data associated with semiconductor modeling are of infinite resolution, interpolation schemes are needed to convert between continuous data and discrete data. The two most important interpolation schemes in a MC simulator are the conversion of a wave-vector to an energy and, its inverse, an energy to a set of wave-vectors.

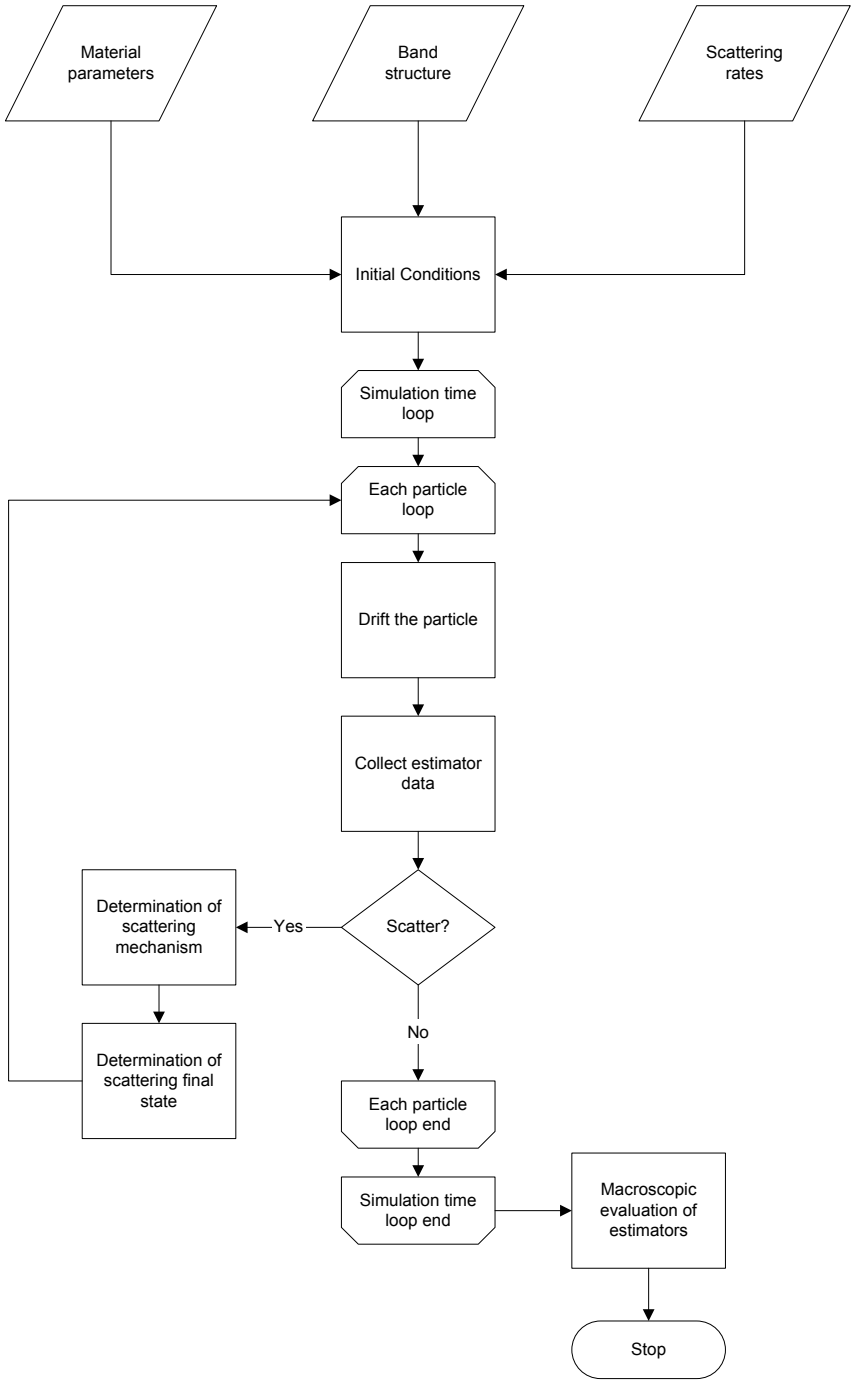

Figure 15: The flow chart for the bulk MC simulator.

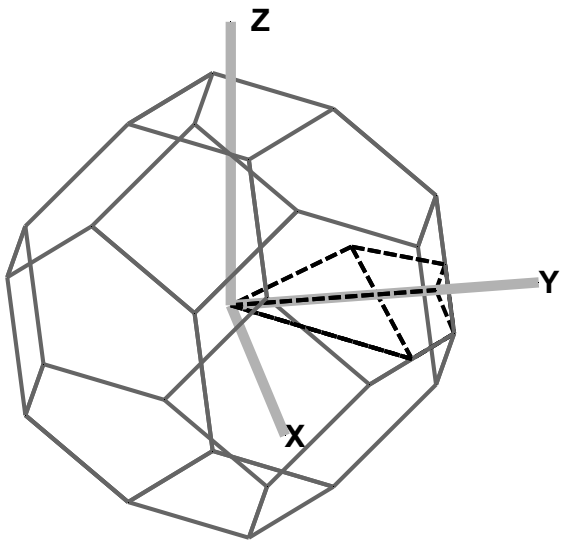

Figure 16: The BZ (solid) and the IW (dotted) for zincblende materials.

3.4.1.1 Energy Interpolation

The real-world band structure is of infinite resolution and infinite range. Of course, some discretization must occur for use in a computer simulation. The first step is to reduce the range, and this occurs in two steps. First, the electron's wave-vector is reduced to the BZ and then it is reduced to the IW (Figure 16). In a crystal lattice, the wave-vectors can take any real value; however, any vector outside the BZ is completely equivalent to a vector inside the BZ. When referring to the energy (and gradient of the energy) of an electron, the volume can be reduced even further by recognizing the symmetry of the BZ. The smallest volume of unique energies in the BZ is called the IW. By transforming the electrons to the IW, the volume of required energies is drastically reduced.

Now, with a manageable volume of energies, the resolution in the IW is still infinite, so the wave-vectors need to be discretized. The IW is discretized by taking

the energy at a wave-vector resolution of $\Delta k = 0.02\frac{2\pi}{a}$. In addition to having infinite resolution, a crystal also has an infinite number of bands. But since, physically, an electron can only reach finite energy values before reaching the vacuum level, χ, the number of bands used in the simulator can be finite. For the ZB materials in this work, only the first four conduction bands of the crystal are needed. This provides an energy range that is larger than what is seen during a simulation. With $\Delta k = 0.02\frac{2\pi}{a}$ and four bands, the band structure function, $E_\nu(\boldsymbol{k})$, becomes manageable.

The interpolation scheme comes into play because, in the simulator, the electrons are not restricted to the discretized k-points. Since an electron in the simulator can take on any k-point, an interpolation scheme is needed. The steps to interpolate an energy are as follows:

1. Bring the k-point into the BZ, which results in a new k-point, $\boldsymbol{k}_{BZ}$.

2. Using the symmetry of the BZ, rotate $\boldsymbol{k}_{BZ}$ into the IW ($\boldsymbol{k}_{IW}$).

3. The vector, $\boldsymbol{k}_{IW}$, is located in a cube with side length Δk. Each of the eight vertexes ($\{\boldsymbol{k}_\lambda\} = \{\lambda = 1, 2, \ldots, 8\}$) is weighted with a second-order Taylor series (Eq. 16).

$$E_{\nu,\lambda}(\boldsymbol{k}) = E_\nu(\boldsymbol{k}_\lambda) + \nabla_k E_\nu(\boldsymbol{k}_\lambda)(\boldsymbol{k} - \boldsymbol{k}_\lambda) + \frac{1}{2}\nabla_k E_\nu(\boldsymbol{k}_\lambda)(\boldsymbol{k} - \boldsymbol{k}_\lambda)^2 \qquad (16)$$

Finally, the energy of this point is determined by the sum over the eight weighted points (Eq. 17).

$$E_\nu(\boldsymbol{k}_{IW}) = \sum_{\lambda=1}^{8} W_\lambda E_{\nu,\lambda}(\boldsymbol{k}_{IW}) \tag{17}$$

Where the weights are given by

$$W_\lambda = \left(1 - \frac{|\boldsymbol{k}_{IW,x} - \boldsymbol{k}_{\lambda,x}|}{\Delta k}\right)\left(1 - \frac{|\boldsymbol{k}_{IW,y} - \boldsymbol{k}_{\lambda,y}|}{\Delta k}\right)\left(1 - \frac{|\boldsymbol{k}_{IW,z} - \boldsymbol{k}_{\lambda,z}|}{\Delta k}\right).$$

The same operations occur when the gradient of the energy is needed; however, although the energy of an electron is invariant on the wedge number, the gradient is not. So, whatever rotation/translation operations brought $\boldsymbol{k}_{BZ}$ into the IW, the same operations need to be applied, in reverse, to the gradient.

There are two very important factors associated with the energy interpolation algorithm: speed and accuracy. The accuracy of the interpolation is crucial, because every aspect of the simulator relies on the energy function. By using a second derivative interpolation scheme, the error is kept small (less than 1% as compared to EPM). As for speed, the MC simulator spends more than 50% of the simulation time interpolating energies, so, obviously, any improvement of the energy routine will have a dramatic effect on the simulator's overall speed. Extensive effort has been spent on ensuring that the energy function is as fast and accurate as possible.

3.4.1.2 Wave-Vector Interpolation

The wave-vector interpolation is used during the final state selection after scattering. The scattering mechanism determines the energy of the particle after a scatter, so, the inverse of an energy interpolation is necessary: a wave-vector with that energy is

needed.

Wave-vector interpolation is the inverse of the energy interpolation: given an energy, it finds the k-points that have that energy. The energy-interpolation scheme, $E_\nu(\boldsymbol{k})$, is a function, so when given a band and a k-point, there is only one energy value; however, for the inverse this is not true. An energy is associated with an infinite number of k-points and a finite number of bands. But, because of the discretization of the IW, only a finite number of wave-vectors are returned on a search.

The data-structure for the search is an array of k-points, bands and energies, sorted by energy (Figure 17). This list is generated at the beginning of the simulation and has roughly 25 million entries. The ordered-energy list consists of the energies for all k-points on a grid of $\Delta k = 0.0025\frac{2\pi}{a}$ or finer. By having this list sorted on energy, a simple binary search can be used to find k-points with a given energy.

The search for a set of wave-vectors, however, cannot find an exact energy value. For example, a search for $E = 1.31458$ will not produce any results because of the discrete nature of the list, so when the wave-vector lookup is performed, an energy delta value is given. The delta value determines the range of energies that are returned (all k-points with energies between $E_f - \Delta E$ and $E_f + \Delta E$). In fact, there are multiple energy deltas used during the simulation because of accuracy and speed constraints (this is discussed in 3.4.3).

3.4.2 The Carrier Drift

A carrier drift is the reaction of a particle to the surrounding electric field. Of course, in a real system, the particle is continually "drifting;" however, in the simulator, the

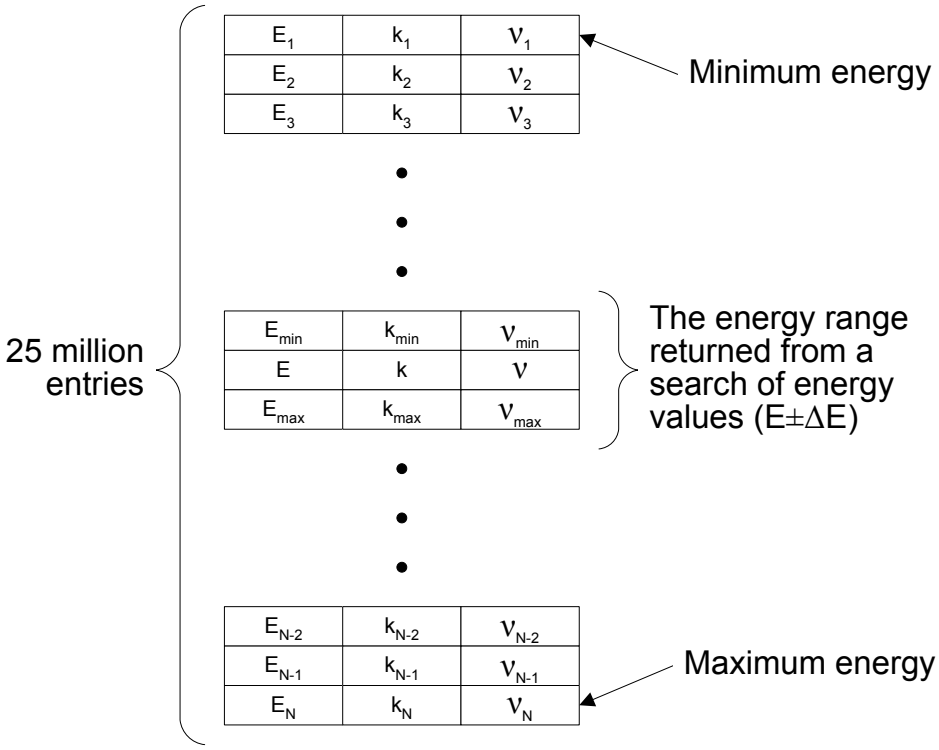

Figure 17: A schematic of the ordered-energy set used in the inverse energy interpolation algorithm.

particles only drift for short periods of time, to be interrupted by scattering events.

The drift process is characterized by a drift time, τ. The drift time is the unit of time of the whole simulator; everything is measured with ticks from this clock. One of the biggest causes of poor performance in the MC simulator occurs when τ is set too small. This causes excessive drift operations (which causes extra, unnecessary energy interpolations, scattering checks, etc.); on the other hand, in order to maintain the stability of the simulator, the drift time cannot be too long either. If the drift time is too long, a particle could miss necessary scatters. To maintain a balance between accuracy and speed, the drift time follows this relationship: $\tau \approx \max\{\mathcal{S}(E)\}/10$, where $\mathcal{S}(E)$ is the energy-dependent total-scattering rate.

Now, with the drift time, the particle drifts in the electric field. The particle is updated in phase-space during a drift. The particle's wave-vector is updated according to Eq. 18, where q is the electronic charge and $\boldsymbol{F}$ is the applied electric field. It is assumed that the particle will drift according to classical Newtonian physics between two potential scatterings.

$$\boldsymbol{k}_f = \boldsymbol{k}_i - \frac{q\tau}{\hbar}\boldsymbol{F} \tag{18}$$

The real-space movement is more complicated, and for full-band MC simulators, some simplifications need to be made. The spatial change resulting from the free-flight of a particle is

$$\boldsymbol{\Delta r} = \int_0^\tau \boldsymbol{v}_g(t)\, dt = \frac{1}{\hbar}\int_0^\tau \nabla_k E(\boldsymbol{k})\, dt, \tag{19}$$

where $\boldsymbol{\Delta r}$ is the change in the real-space vector and $\boldsymbol{v}_g$ is the group velocity of the particle. For analytic bands, this equation can be numerically (or directly) evaluated and the real-space movement will be exact; however, in a full-band simulator, the band structure function, $E_\nu(\boldsymbol{k})$, is much too complicated to be evaluated in the integral. But, because the drift-time in the MC simulator is small, a simple two-point approximation of $\boldsymbol{\Delta r}$ is valid:

$$\boldsymbol{\Delta r} = \frac{\boldsymbol{v}_{g,i} + \boldsymbol{v}_{g,f}}{2}\tau = \frac{\nabla_k E(\boldsymbol{k})|_{\boldsymbol{k}=\boldsymbol{k}_i} + \nabla_k E(\boldsymbol{k})|_{\boldsymbol{k}=\boldsymbol{k}_f}}{2\hbar}\tau, \tag{20}$$

where $\boldsymbol{v}_{g,i}$ is the group velocity at the initial k-point and $\boldsymbol{v}_{g,f}$ is the group velocity after the drift.

After the particle is subjected to a drift process, it can scatter. Since the scattering rate is simply the probability of a scatter per unit time, the scatter-check formula is

$$\mathcal{P}_{scatter} = \mathcal{S}(E)\tau \tag{21}$$

where $\mathcal{S}(E)$ is the energy-dependent total-scattering rate. A random number is chosen, and if the number is less than $\mathcal{P}_{scatter}$, the particle scatters, otherwise, the particle "self-scatters." A self-scatter is a computational result from the discretization of time.

A particle (on average) will self-scatter 9 times and non-self-scatter 1 time for every 10 drifts. When the particle does scatter, the simulator moves into the scattering process.

As stated before, the self-scatter is a major computational hurdle in MC simulation. In order to guarantee convergence of the simulation, the drift time must be less than the maximum scattering rate by a margin (about 10 times less to account for the randomness of the scattering decision). However, every self-scatter is a wasted drift since a single double-length drift is equivalent to a drift, self-scatter, drift. The difference between the two is that the latter involves an additional call to the energy and energy gradient interpolation. These calls are unnecessary in the former case. The problem is magnified by the fact that the maximum scattering rate at a given particle's energy and the maximum overall scattering rate (from which the drift-time is derived) can differ by as much as a factor of 1000.

The solution to the self-scattering problem is to use more than one drift time for differing conditions. The scattering rate can be broken up into different energy regions with a drift-time for each region, or the drift-time can be computed with a random distribution [75]. The problem with this technique is that the synchronization of the ensemble of particles is sacrificed. Therefore extra drifts have to be inserted to re-sync the ensemble before statistics can be taken from the ensemble, or in the case of the device, the ensemble must be re-synced even more often. In this work, the constant drift time is used at the expense of computation time; however, the simulator could be improved by examining these methods.

Table 2: The scattering mechanisms and the corresponding electron's final-state energy after a scatter.

Scattering mechanism	Energy conservation	Final state energy
polar optical absorption	inelastic	$E_f = E_i + \hbar\omega_{OP}$
polar optical emission	inelastic	$E_f = E_i - \hbar\omega_{OP}$
non-polar optical absorption	inelastic	$E_f = E_i + \hbar\omega_{NP}$
non-polar optical emission	inelastic	$E_f = E_i - \hbar\omega_{NP}$
acoustic absorption	inelastic	see text
acoustic emission	inelastic	see text
ionized impurity	elastic	$E_f = E_i$
impact ionization	inelastic	$E_f = E_i - E_g$

3.4.3 The Electron Scatter

The scattering process is probably the most complicated section of the simulator. It starts when it is determined that the particle does indeed scatter (non-self scatter). From there, the type of scattering mechanism is randomly determined, based on the relative strength of the scattering rates, and the final state's energy is calculated, based on the chosen scattering mechanism.

The choice of scattering mechanisms mirror the scattering rate calculations in Section 3.3: acoustic, polar optical, non-polar optical, impurity and impact ionization. The energy of the final state for the particle depends on which type of scattering occurred. The list of possible scattering types, and the formulas for the particle's final-state energy, are given in Table 2. Acoustic phonons (because of their non-constant phonon energy) require a more complicated final-state energy calculation (Eq. 22, absorption and Eq. 23, emission) [53]. With the particle's final energy calculated, the reverse-energy-lookup algorithm can start to resolve the final k-point of the particle.

$$
\begin{aligned}
E_{aco} &= \frac{0.5 M_e v_s^2}{q} \\
C &= \frac{4\sqrt{E_{aco}}}{\frac{k_B T}{q}} \\
x &= C(\sqrt{E_i} + \sqrt{E_a co}) \\
z_1 &= \frac{1}{3}x^3 - \frac{1}{8}x^4 + \frac{1}{60}x^5 - \frac{1}{5040}x^7 \\
z_2 &= \frac{1}{2}x^2 - \frac{1}{6}x^3 + \frac{1}{48}x^4 - \frac{1}{4320}x^6 \\
E_f &= E_i + \frac{k_b T}{q}\frac{z_1}{z_2}
\end{aligned}
\tag{22}
$$

$$
\begin{aligned}
E_{aco} &= \frac{0.5 M_e v_s^2}{q} \\
C &= \frac{4\sqrt{E_{aco}}}{\frac{k_B T}{q}} \\
x &= C(\sqrt{E_i} - \sqrt{E_a co}) \\
z_1 &= \frac{1}{3}x^3 - \frac{1}{8}x^4 + \frac{1}{60}x^5 - \frac{1}{5040}x^7 \\
z_2 &= \frac{1}{2}x^2 - \frac{1}{6}x^3 + \frac{1}{48}x^4 - \frac{1}{4320}x^6 \\
E_f &= E_i - \frac{k_b T}{q}\frac{z_1}{z_2}
\end{aligned}
\tag{23}
$$

It is useful to again mention the removal of the valleys from the simulator, because the electron's final-state selection is where the valley-less simulator becomes both more straightforward and more accurate. With an analytic band structure simulator, the concept of valleys is simple. An electron can occupy one and only one valley and cannot be anywhere else; however, with a full-band simulator, an electron can

be in a valley or not be in a valley. Previous simulator generations used a clever technique to both find and keep track of valleys throughout the simulation. This technique works fairly well when only electron drifts are considered, but when the final-state selection is included, the algorithms become unnecessarily complicated and potentially inaccurate. The reason is that when the final-state selection uses analytic formulations, a return to the full-band model becomes difficult. Analytic final-state selections use an analytic band structure in their derivation, so when these algorithms are applied to the full-band model, the band structures do not line up. So the final-state algorithm produces a final k-point for the electron (with by definition a specific energy); however, the energy of that final state is not the same in the empirical band structure as it is in the analytic band structure. So if the result of the analytic final-state selection does not match the empirical band structure, another iteration of the algorithm must be run. This continues until the two results coincide.

This simulator eliminates this trial algorithm and directly uses the fully-numerical formulation of the scattering rates to determine the final-state after a scattering event. By using the full derivation of the scattering rate for final-state selection, every final k-point chosen is valid; however, some k-points will have a higher probability of being picked because of the relative strength of that interaction (between the initial k-point and the potential final k-point). On average, the choices made from the direct, fully-numerical method will reproduce the analytic final-state formulations used in the previous work. Again, the simulator circumvents the mathematical derivations of the scattering mechanisms by relying on the relative strengths of the pure scattering rates to produce the answer.

After computing the final energy of the particle, the scattering process needs to find a list of k-points that have that energy. As mentioned before, there are multiple energy deltas used to perform the wave-vector interpolation. Using many energy deltas increases the speed and accuracy of the simulator. The algorithm for choosing the delta is exhibited in Figure 18. Obviously, as the energy delta increases, the number of k-points that satisfy the reverse lookup will increase. The choice of ΔE comes from the trade-off between execution speed and validity. From this trade-off, a cutoff number of k-points is established, k_{cutoff}. The algorithm starts at the smallest ΔE and does a reverse-lookup query. If the number of k-points returned is greater than k_{cutoff}, then there are enough points and the algorithm is done. But, if too few points are found for that delta, ΔE is increased and the lookup is repeated. ΔE continues to grow until the reverse-energy lookup returns at least k_{cutoff} points. When the algorithm completes, there is a list of potential final-state k-points that all conserve energy. Next, the scattering process assigns a probability to each of the k-points and randomly picks one of them.

For all scattering mechanisms except impact ionization, the scattering process now focuses on momentum conservation. Each k-point in the list already conserves energy (plus or minus the numerical error, ΔE) and momentum does not need to be conserved (because the phonon receives the difference); however, each phonon type does have a probability distribution of wave-vectors. Table 3 contains the probability distribution for each phonon type, where $\boldsymbol{q} = \boldsymbol{k}_f - \boldsymbol{k}_i$ is the phonon's wave-vector. The algorithm for final-state selection is

`foreach(`$\boldsymbol{k}_{IW} \in$ `findkpts(`E_f`, `ΔE`))`

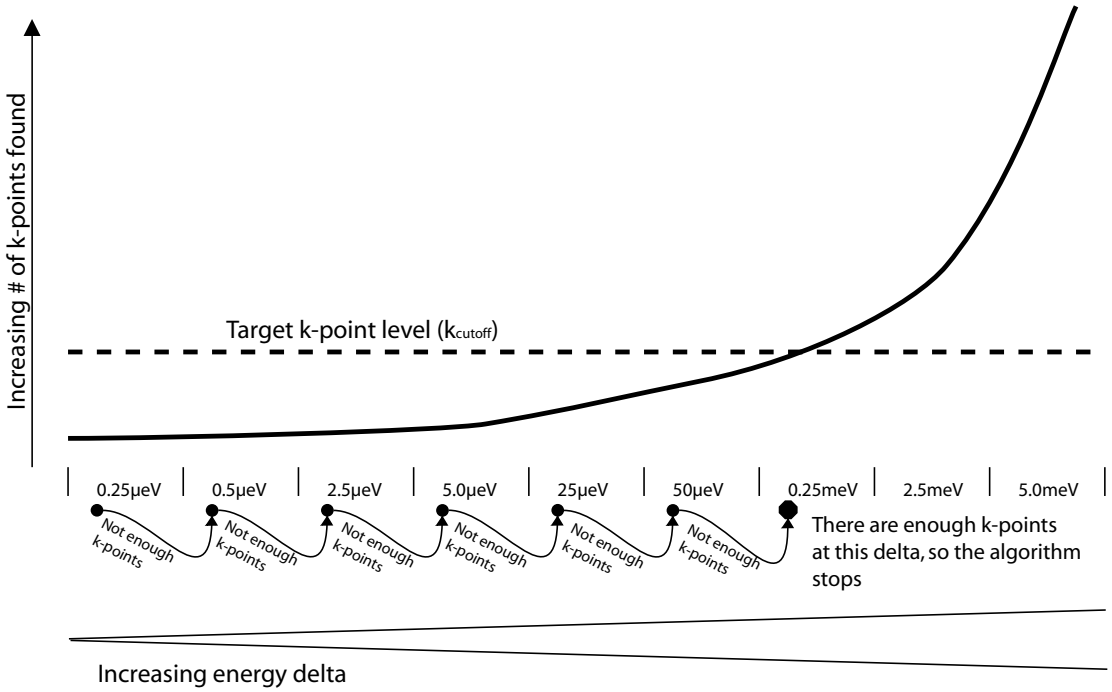

Figure 18: Schematic for the algorithm that chooses the energy delta during a scatter.

```
    foreach(w ∈ wedges)
      k_f = transform_wedge(k_IW, w)
      q = k_f − k_i
      probability = I(k_f, k_i)×P(q)
    end
end
```

First, the list of IW k-points is found using the energy delta that was determined in the previous paragraph. Now, the particle can scatter to any location in the BZ that satisfies energy conservation, and any point in the IW has the same energy as the equivalent wedge points. So, the resulting final-state k-points from the energy lookup are transformed to each of the 48 (for zincblende) wedges. With the initial

Table 3: The phonon type and the phonon wave-vector distribution function.

Phonon type	Probability distribution
polar optical	$\frac{1}{\|\boldsymbol{q}\|^2}$
non-polar optical	1
acoustic emission	$\|\boldsymbol{q}\|$
ionized impurity	$\frac{1}{(\|\boldsymbol{q}\|^2+\beta^2)^2}$

and potential final k-points, $\boldsymbol{q}$ is computed. Next, for each possible final k-point, the phonon wave-vector probability, $\mathcal{P}(\boldsymbol{q})$, and the overlap integrals are computed. For each k-point in the reverse-energy list, the phonon's wave-vector and the overlap between the two states are computed, and a running count of the probabilities is saved. Finally, using a MC rejection technique, a random number chooses the final state of the particle, and the scattering process is complete.

The final-state selection for impact ionization is slightly different from that of the other mechanisms, because the impact ionization mechanism does not involve a phonon; it is an interaction between two electrons. In the simulator, however, it is modeled as a scattering process. The conservation of energy and the computation of the wave-vectors remains the same; however, the determination of the final state is different.

The momentum conservation computation illustrates the first point made about the multiple ΔE values. Computing the $\boldsymbol{q}$ distribution function and looking up the overlap takes time. If too many points result from the reverse-energy lookup, then the performance of the scattering process will be hampered. On the other hand, if too

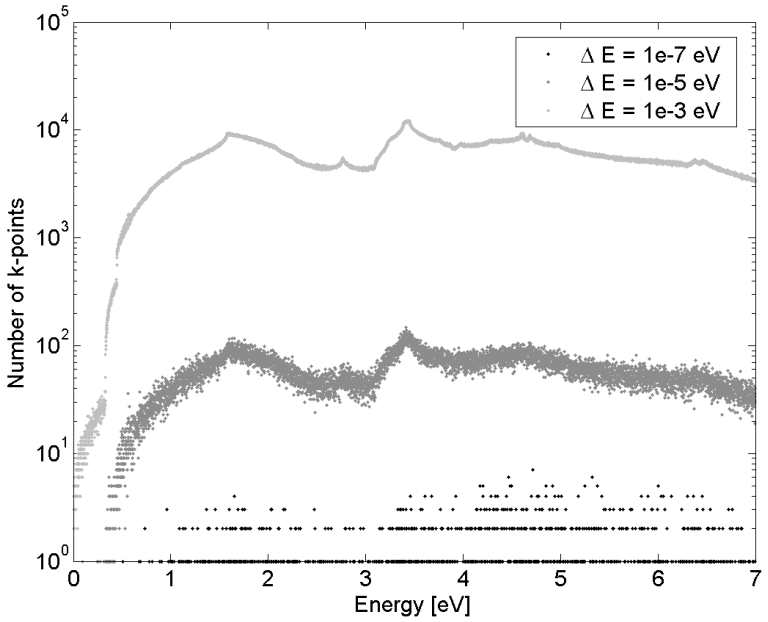

Figure 19: A graph of the number of final-state k-points that satisfy the energy delta conservation taken from a bulk simulation of GaAs.

few points are found, then the choice of phonon wave-vectors may not be large enough to reproduce the correct distribution for each of the mechanisms. For instance, if, during a polar-optical event, only 5 points are found in the reverse-lookup algorithm, then they will conserve energy; however, all 5 points could have a large $\boldsymbol{q}$. From table 3 it is seen that the probability of a large $\boldsymbol{q}$ for a polar-optical phonon is small, but if all 5 points have a large $\boldsymbol{q}$, one of them will have to be chosen, and that selection will skew the distribution of polar-optical phonons to the high $\boldsymbol{q}$ region. This is *not* saying that, during a normal simulation run, there will never be a polar-optical phonon with a large $\boldsymbol{q}$, it is just saying that if, for every scatter, all of the choices are low-probability vectors, then the distributions can become invalid. There has to be the proper quantity of small $\boldsymbol{q}$s and large $\boldsymbol{q}$s to guarantee that the distribution will be valid. This requires a k_{cutoff} number of final-state possibilities.

There is another benefit to the varying ΔE values. When the electrons in the simulator reach higher energies, the number of k-points found in the reverse-energy lookup increase in related to the density-of-states (Figure 19); as a result, the ΔE can drop and still satisfy the k_{cutoff} requirement. A smaller ΔE will result in final-state selections that have a more accurate energy conservation. This is an important benefit, especially because this simulator is aimed at high-energy effects. So, having multiple energy deltas results in a simulator that is both faster and more accurate.

The data in Figure 20 are the result of a GaAs MESFET device simulation. The simulation occurs close to GaAs's breakdown, so the results include both high energy and low energy particles. The graphs illustrate the phonon wave-vector probability distributions mentioned earlier. It is useful to analyze them to prove the validity of the simulator's scattering process.

The upper two graphs are the data for the polar-optical phonons. Notice that there is a very large percent of the distribution at low $\boldsymbol{q}$, which is what is expected, since the probability is proportional to $\frac{1}{|\boldsymbol{q}|^2}$. Next there are the acoustic phonon and the non-polar-optical phonon graphs. The acoustic phonons have a varied distribution, but notice that the peak is at large $\boldsymbol{q}$s (as opposed to the non-polar-optical phonons, which have a much flatter distribution). This is because the acoustic phonon scattering rate is directly proportional to $|\boldsymbol{q}|$, which moves the distribution to large wave-vectors. The peak in the acoustic distribution near $\boldsymbol{q} = 0$ arises from the low energy electrons scattering in the Γ valley. Since those electrons do not have enough energy to jump to a different valley, they have to scatter within the Γ valley. The Γ valley is small, which means that the scatter must involve a small $\boldsymbol{q}$. With this

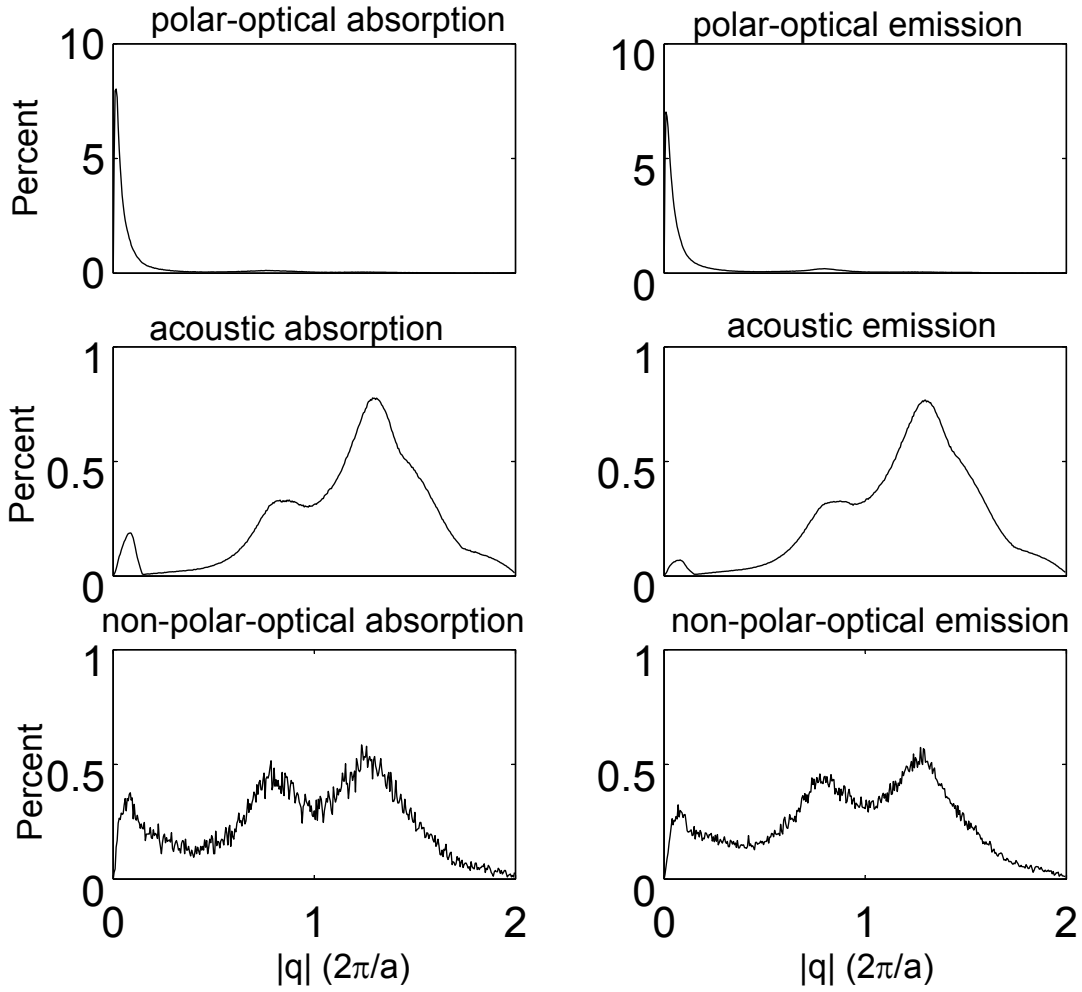

Figure 20: The q-distribution results (as a percent of all scatters) for all of the phonon types taken from a simulation of a GaAs MESFET.

analysis, the simulation matches the theoretical phonon wave-vector distributions and the MC scattering process is confirmed.

3.4.4 The Estimators

Estimators are microscopic variable analyzers. They are continually updated from the ensemble of particles throughout the simulation. By analyzing the estimators, macroscopic information about the simulation can be gleaned.

Since MC is an inherently noisy solution, the analysis of the results must be

carefully considered. In order to reduce the statistical uncertainty of the simulation results, the simulation time, T, is divided into smaller sections, called output times, T_O. Instead of analyzing the estimators over the entire history and getting one average value, the estimator sub-history versus time can be used. This allows further analysis of the microscopic information. Specifically, usually only the later part of the estimator data is used, because, generally, the beginning of a simulation is marred by transients.

There are four main estimators in the bulk simulator:

1. Gradient velocity
2. Drift velocity
3. Scatter velocity
4. Average energy

The gradient velocity is the ensemble average-velocity computed from the gradient of the band structure. It is very accurate and is computed as follows

$$\boldsymbol{v}_{grad}(t) = \frac{\frac{q}{\hbar}\sum_{p\in\text{particles}} \nabla_k E_p}{N}, \tag{24}$$

where q is the electronic charge, E_p is the energy of a particle in the ensemble, and N is the number of particles. This computation occurs at the end of each T_O step to produce the gradient-velocity estimator, $\boldsymbol{v}_{grad}(t)$.

The drift-velocity estimator is computed by looking at the amount of energy the ensemble of particle receives/loses during drifts. The formula for $|\boldsymbol{v}_{drift}(t)|$ is

$$|\boldsymbol{v}_{drift}(t)| = \frac{\sum_{p\in\text{particles}} \sum_{\text{drifts}} (E_{p,f} - E_{p,i})}{|\boldsymbol{F}|\tau N} \tag{25}$$

where $E_{p,i}$ and $E_{p,f}$ are the energies of a particle before and after a drift, respectively, and, again, N is the number of particles. The drift estimator is also very accurate, and, over the length of the simulation, will converge to the same value as the gradient-velocity estimator does (which should be expected).

The scatter-velocity estimator uses the amount of energy gained and lost through scattering events to compute the velocity of the ensemble. The equation is

$$|\boldsymbol{v}_{scatter}(t)| = \frac{\sum_{p\in\text{particles}} \sum_{\text{scatters}} (E_{p,f} - E_{p,i})}{|\boldsymbol{F}|\tau N}, \tag{26}$$

where $E_{p,i}$ and $E_{p,f}$ are the energies of a particle before and after a scatter, respectively. The scattering velocity estimator is noisy, and, in many cases, its usefulness is limited. The scattering estimator is noisy because of the discrete and infrequent nature of scatters. When a particle does scatter, the amount of energy gained is large (so the velocity in that case will be high). However, many times a particle will not scatter during a T_O step, so the scattering velocity estimator jumps from low velocities to high velocities, but generally oscillates around the correct velocity. However, in an ideal simulator, the scattering-velocity estimator would converge, over time, to

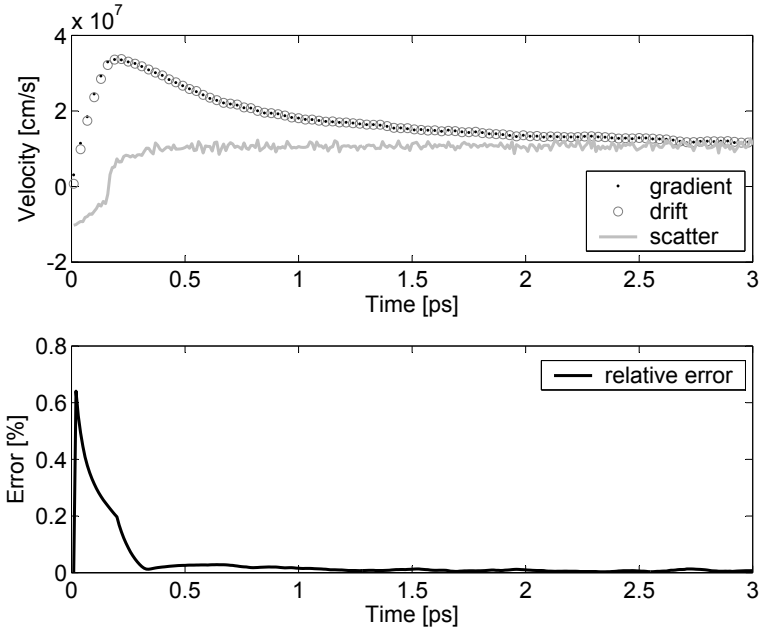

Figure 21: Results for some of the estimators calculated during a simulation of bulk GaAs. The top graph shows a common velocity field curve in bulk GaAs, measured with each of the velocity estimators. The bottom graph shows a relative error curve which approximates the error within the calculations.

the other velocity estimators; at high fields it generally does.

The average energy estimator is very simple. It is computed by calculating the average energy of the particles in the ensemble for the current sub-history:

$$\bar{E}(t) = \frac{\sum_{p \in \text{particles}} E_p}{N} \tag{27}$$

Figure 21 shows the results from a bulk GaAs simulation with $F_x = 10\frac{kV}{cm}$. The simulation lasted for 3 ps and the ensemble contained 20,000 particles.

CHAPTER IV

DEVICE MODELING

With the bulk MC simulator in place, the system can now be extended to perform device simulations. As mentioned before, the MC section of the device simulator is the same as that of the bulk simulator. The only difference between the two is that the device simulator has extra modules to solve the Poisson equation and keep track of the real-space locations of the particles.

4.1 Device Algorithm

The flow chart for the device simulator is shown in Figure 22. The simulator consists of five main modules: `surface`, `renew`, `charge`, `poisson` and `current`. In addition to these device modules, the drift and scatter modules from the MC bulk simulator are used to compute the reaction of the electrons to the fields present in the device. Finally, the output module is used to gather the statistics from the simulator for further post-processing analysis.

The device simulator is initialized by reading in the device structure and placing the electrons throughout the device. Next, all of the particles in the device are drifted and scattered, updating the phase-space vector and the real-space location. The `surface` module enforces the boundary conditions throughout the device; particles can leave the device in this module, but no new particles are introduced. Particles

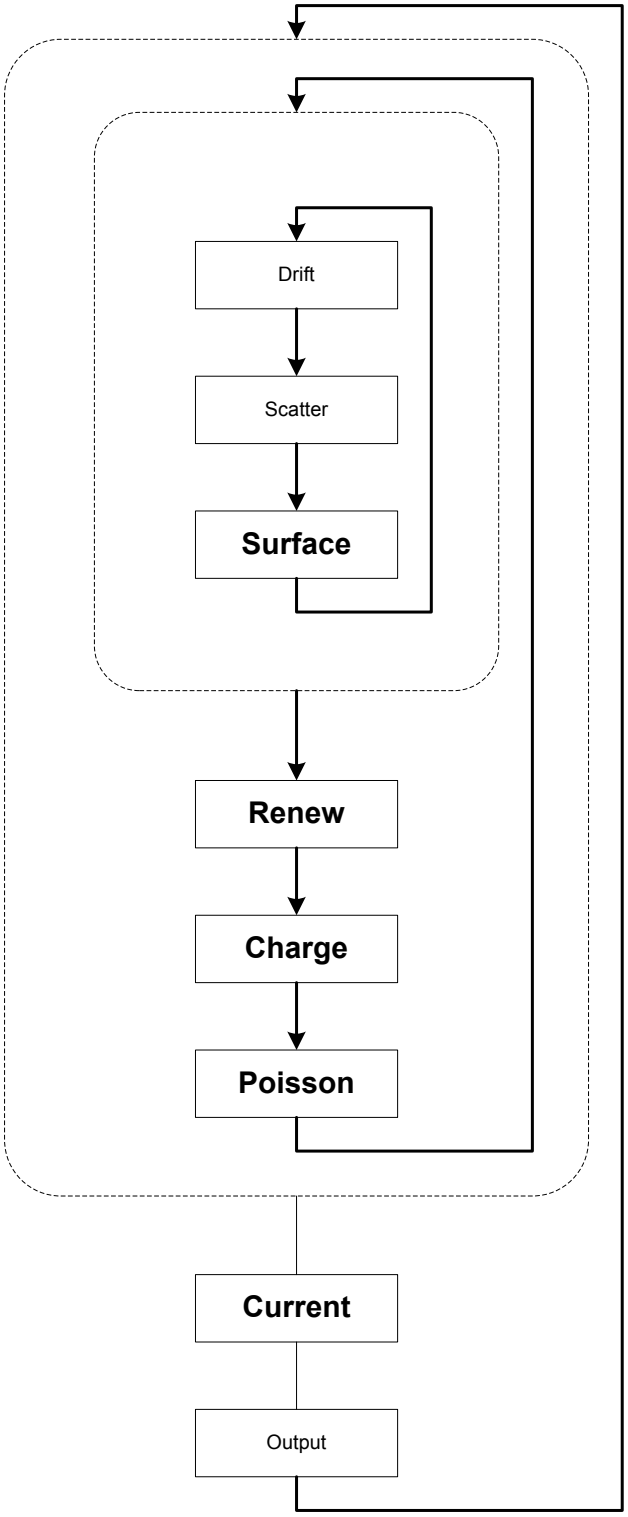

Figure 22: A schematic overview of the device simulation modules.

are reintroduced into the device, because of charge neutrality, in the `renew` module. Next, the `charge` module computes the charge and carrier concentration throughout the device. Then, the `poisson` module uses the current carrier concentration to update the potential and electric fields in the device. And finally, the `current` module computes the current in the device for that time step. This process continues for the duration of the simulation. Each of the device modules will be discussed in detail in the following sections.

4.2 Initialization

The simulator begins by reading all of the material information needed throughout the simulator: scattering rates, band structures, material parameters and overlap integrals. Next, the device-specific information, including the grid information and the doping profile, is loaded. And finally, the data structures needed in the simulator, like the ordered energy set, are calculated.

To begin the simulation, the electrons in the simulator are grouped into super-particles because of the high doping concentrations in the device. A super-particle typically represents $\approx 100,000$ electrons. The simulator starts by distributing the super-particles throughout the device according to the doping levels provided. The initial doping profile is then used in both the `renew` module and the `poisson` module. Throughout this discussion, a super-particle will be referred to as a particle or an electron; however, in the simulator they are always super-particles.

Now, the positions and momenta of the super-particles must be established. The initial conditions in the device are somewhat arbitrary since the device geometry,

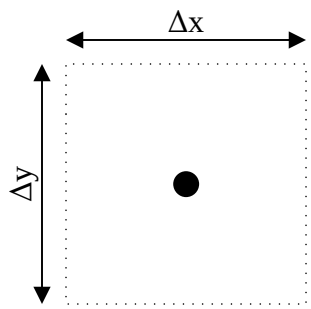

Figure 23: The schematic for a single grid cell in the device simulator.

initial doping and applied voltages will govern the steady-state response; however, a poor initial condition decision will extend the simulation time. So in this work, the carrier locations are distributed to ensure charge neutrality by randomly distributing an equal number of electrons as there are dopants, and the carrier momenta are generated using a randomized Maxwellian distribution. This ensures a relatively short relaxation time (the only way of reducing the relaxation time further is to pre-process the device geometry with a drift-diffusion or analytic simulation and read the steady-state potential in as the initial condition).

4.3 The `surface` *Module*

4.3.1 Grid Definition

The grid definition is a very important concept in the device simulator. All of the calculations and results are defined on the grid, and it represents the physical size and shape of the device being simulated. The `surface` module uses the grid to confine the electrons, by applying the imposed boundary conditions.

A grid point is centered in a grid box (Figure 23). All of the particles contained in that box (except those that deal with charge) belong to that grid point. For example,

when computing the average energy of the particles in the device, the corresponding grid point is assigned the average energy of all of the particles in a grid box corresponding to that grid point. The spacing between two grid points in each direction is Δx and Δy, which also define the size of the grid box. Although Δx does not have to equal Δy, in this simulator it does. Repeating these grid points over the whole device results in a matrix of grid points and grid boxes. As a result, all of the operations and results in the device simulator operate on these grid matrices.

One of the important decisions to make when defining the grid for the device is the grid spacing, Δx. If the grid spacing is too small, then the computation time and memory requirements become unwieldy; on the other hand, if the grid spacing is too large, then the device results will not converge properly. Because a large grid will produce incorrect results, the choice of Δx errs on the side of small. The upper limit on the size of the spacing is related to the Debye length of the electrons [40], and is given by

$$\Delta x < \lambda_D \tag{28}$$

with λ_D defined by

$$\lambda_D = \sqrt{\frac{\epsilon_0 k_B T}{q^2 n}} \tag{29}$$

where ϵ_0 is the static dielectric constant, k_B is the Boltzmann constant, T is the absolute lattice temperature, q is the charge of an electron, and n is the carrier concentration. A grid spacing of 2.5 nm is chosen in order to satisfy these requirements.

In addition to the Debye length requirement, the maximum distance that a particle should travel during a Poisson time-step should be smaller than the grid spacing, so that a particle does not skip over any grid points during its travels. This criteria is also satisfied with the choice of $\Delta x = 2.5\,\mathrm{nm}$.

4.3.2 Boundary Conditions

4.3.2.1 Edge of Device

The edges of the device that do not contain contact regions are modeled with Neumann conditions. This means that there is no flux of charge through that edge; consequently, the electric field is zero at that point. The `surface` module simply reflects a particle off of this boundary. In addition to reflecting the particle in real space (which keeps the charge flux zero) the particle's k-point is reflected in the direction that the particle left the device. This is because the k-point of the particle defines how it reacts to the electric field. Thus, because the particle drifted out of the device, the k-point needs to be inverted so the direction vector of the particle is also reflected.

4.3.2.2 Contacts

All the edges of the device that are left are covered by contacts. There are two kinds of contacts that this simulator can handle: ohmic and Schottky. As far as the `surface` module is concerned, both contacts behave exactly the same. They are both perfectly absorbing. If a particle leaves through either of the two contact types, it is included in the current calculation and the particle is deleted from the ensemble. The difference between the two contacts comes into play during the `renew` module.

4.4 *The* `renew` *Module*

The `renew` module injects particles back into the device and removes extra particles from the device to maintain charge neutrality. The two different types of contacts (ohmic and Schottky) are differentiated in this module. Since a Schottky contact is rectifying, no particles can enter this contact. As a result, the `renew` module completely ignores the Schottky contacts and only considers the ohmic contacts.

The device is defined with a specific initial doping concentration. When this concentration is translated into the particle ensemble, the result is an electron count for each grid cell. This is where the `renew` module gets its charge neutrality information. In the cell directly adjacent to the ohmic contact, charge neutrality is enforced. If the current number of electrons in the neutral cell is more than the doping electron count, then electrons are removed from the device (through that ohmic contact) until that cell is charge-neutral. Conversely, if the current number of electrons is less than the doping electron count, then particles are injected into the cell through the contact. The particles that are injected are uniformly distributed along the length of the grid cell, on the edge adjacent with the contact. The momentum of the electron is directed into the device, and the initial k-point is computed randomly from the thermal equilibrium distribution. The result is a charge-neutral layer of cells directly below the ohmic contact.

4.5 *The* `charge` *Module*

With all of the boundary conditions and contact detections completed, the simulator can calculate the charge distribution throughout the device. As stated before, the

normal grid box rules are not used in this module. If the regular grid box rules were used, termed the nearest-neighbor rules, some accuracy would be lost because a super-particle (which represents the charge of many electrons) on the border of a grid cell should really be divided between the two adjacent grid points. This scheme, called cloud-in-cell, is used for the charge distribution because of the large impact it has on the simulation. The charge distribution is integral in determining the potential and field profile, and the field profile is the most important factor in driving all of the electrons in the system. So, even though the cloud-in-cell method takes more computation time, it is used in the `charge` module to ensure the greatest accuracy.

4.5.1 Cloud-in-Cell

The cloud-in-cell method is used to distribute super-particle charge. Since each of the particles in the simulation is not an individual electron, but, is in fact, a cluster of many electrons, assigning the entire charge of the super-particle to one grid point would be a great simplification. The cloud-in-cell method distributes a portion of charge to up to four adjacent grid points (Figure 24). The super-particle's charge is modeled as a uniform box of charge with a size equal to that of a grid box (the black square). Now, this charge box will overlap up to four grid boxes (the four boxes with black points in them). A fraction of total super-particle charge is distributed to each of the four grid points (the four black points) based on the area of the overlap between the charge box and the corresponding grid box.

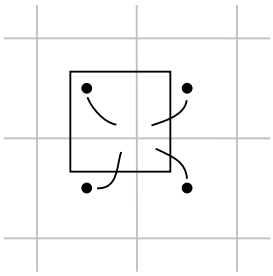

Figure 24: An illustration of the cloud-in-cell algorithm.

4.6 The `poisson` *Module*

The `poisson` module is used to calculate the electrostatic potential (and the field profile) throughout the device. The Poisson equation gives the electrostatic potential due to a distribution of charge. The two-dimensional Poisson equation is given by

$$\frac{\partial^2 \Phi}{\partial x^2} + \frac{\partial^2 \Phi}{\partial y^2} = -\frac{\rho}{\epsilon}, \tag{30}$$

where Φ is the electrostatic potential, ρ is the charge density distribution, and ϵ is the dielectric constant. Although the Poisson equation can be solved analytically, in general, for the complex charge distributions seen in a MC simulation, it must be solved numerically. As with the previous device work [31], an iterative finite-difference scheme is used to solve the equation. The potential is discretized on the same grid points as used for the other variables, and the charge distribution comes from the cloud-in-cell method mentioned previously. The finite-difference scheme is applied to the partial derivatives, resulting in

$$(\Phi_{i+1,j} - 2\Phi_{i,j} + \Phi_{i-1,j}) + (\Phi_{i,j+1} - 2\Phi_{i,j} + \Phi_{i,j-1}) = -\frac{\rho_{i,j}}{\epsilon}\Delta_x\Delta_y \tag{31}$$

where i and j are the node indices of the grid points, $\rho_{i,j}$ is the charge density at node (i, j) from the `charge` module, and Δ_x and Δ_y are the grid spacings from Figure 23. Each grid-point in the device has one Equation 31 associated with it, so the resulting equation to be solved is a large system of linear equations.

Eq. 31 is used for internal, non-boundary nodes. When the node, (i, j), is a boundary node, the boundary conditions come into play. As described previously, there are two different boundary conditions: Dirichlet and Neumann. Dirichlet boundary conditions force the electrostatic potential at a node to a given voltage:

$$\Phi_{i,j} = V_{applied} \tag{32}$$

Neumann boundary conditions force the field to zero, which means that the electrostatic potential at the boundary is equal to the potential at the adjacent grid-point. Since the Neumann boundary condition varies with the location of the boundary, there are four cases:

$$\begin{cases} \Phi_{i,j+1} + \Phi_{i,j-1} + 2\Phi_{i-1,j} - 4\Phi_{i,j} = -\frac{\rho_{i,j}}{\epsilon}\Delta_x\Delta_y & top \\ \Phi_{i,j+1} + \Phi_{i,j-1} + 2\Phi_{i+1,j} - 4\Phi_{i,j} = -\frac{\rho_{i,j}}{\epsilon}\Delta_x\Delta_y & bottom \\ \Phi_{i+1,j} + \Phi_{i-1,j} + 2\Phi_{i,j+1} - 4\Phi_{i,j} = -\frac{\rho_{i,j}}{\epsilon}\Delta_x\Delta_y & left \\ \Phi_{i+1,j} + \Phi_{i-1,j} + 2\Phi_{i,j-1} - 4\Phi_{i,j} = -\frac{\rho_{i,j}}{\epsilon}\Delta_x\Delta_y & right \end{cases} \tag{33}$$

Combining Eq. 31, Eq. 32, and Eq. 33 results in a system of linear equations of the form $\boldsymbol{P} \cdot \boldsymbol{\Phi} = \boldsymbol{c}$ where $\boldsymbol{P}$ is the linear coefficient matrix, $\boldsymbol{\Phi}$ is the electrostatic potential at each grid point, and $\boldsymbol{c}$ is a constant vector, filled with constants:

$$\begin{cases} V_{applied} & for\ Dirichlet\ BCs, \\ -\frac{\rho_{i,j}}{\epsilon}\Delta_x\Delta_y & else \end{cases} \tag{34}$$

The resulting matrix is very large, containing approximately 10 million elements. This, however, does not prove to be that difficult (or time consuming) to solve. Of course, the matrix is not solved directly with inversion. Since the matrix is sparse (only having 5 non-zero diagonals), a conjugate gradient squared iterative solver is used [41]. This method provides both good convergence and fast execution speed. The result is the potential at each grid point in the device. With the potential at each grid point, the computation of the electric field at each grid point is trivial. So, the `poisson` module is complete, having updated the potential and electric field in the device to match that of the new charge distribution.

4.7 *The* `current` *Module*

The final module in the device simulator is the `current` module. This is where the electron distribution is analyzed to compute the currents in the device. The simplest method for computing the current is to count the number of particles that enter and leave the device through the contacts. Throughout the simulation, a net total number of electrons that left through each contact is recorded. At the end of the

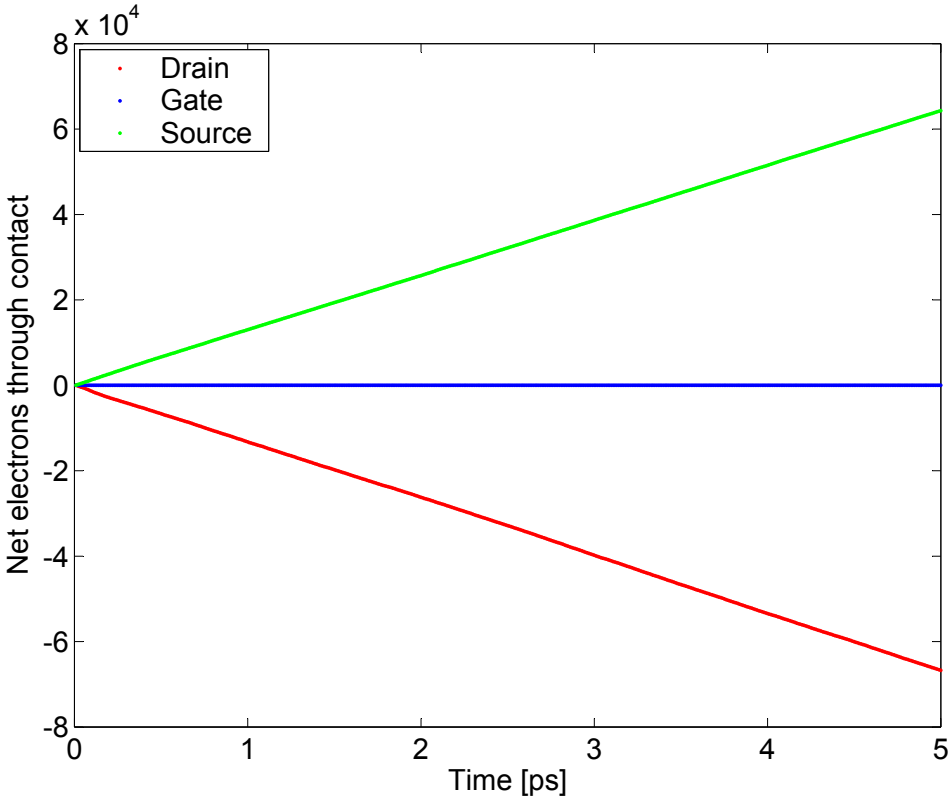

Figure 25: The raw electron count results for a GaAs MESFET simulation. The graph shows the cumulative net number of electrons that enter the device through the drain, gate, and source contacts. The current through a given terminal is the derivative of its electron count line.

simulation, this total is the output for each time step (Figure 25). The derivative of this data is the current through that contact. To achieve proper steady-state current convergence, the simulation needs to last long enough. Generally, 5 ps is enough to enter the steady-state region.

CHAPTER V

MESFET DIRECT-CURRENT BREAKDOWN

With the device simulator in place, allowing the simulation of GaAs, 3C-SiC, and ZB-GaN MESFETs, the first analysis made is the comparison of the direct-current (DC) breakdown of these materials. The details of these analyses are given in this chapter. First, a brief description of the theory of DC breakdown is given, followed by some implementation details, and, finally, the results from the simulations.

5.1 Theory

Device breakdown occurs when the fields in the device are high enough to induce impact ionization. The result of the impact ionization events is the addition of current carrying particles. This additional current from the impact ionization is the breakdown current. The definition of DC breakdown, however, includes the hole population, which this work does not include. So a modified view of breakdown is introduced (as with our previous breakdown work [31]). In this work, the DC breakdown of a device is defined as the point at which the drain current due to breakdown is 3% of the total drain current in the device. This allows the DC breakdown to be computed without the use of holes, and the computation still be accurate. The effect of holes in breakdown is negligible until the device enters the multiplication region, which occurs after the onset of impact ionization. The simulations in this work stop

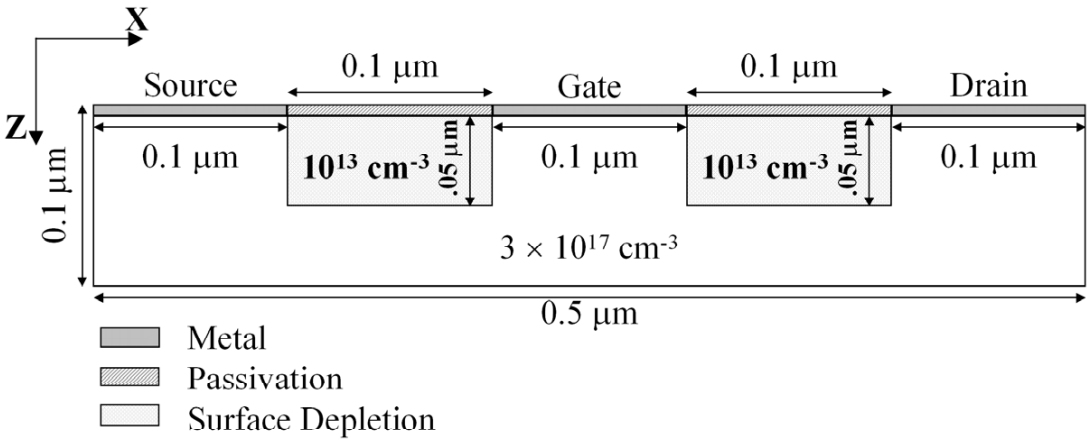

Figure 26: A cross-section of the simulated MESFET for DC breakdown.

soon after the onset of impact ionization, so the net multiplication is relatively low.

5.2 Implementation

A $0.1\mu m$ gate-length MESFET is used for the breakdown calculations. The geometry and doping levels of the device are shown in Figure 26. This device is the same as that used in our previous GaN MESFET simulations [31, 50]. The ionized doping in the device is uniform at $3 \times 10^{17} cm^{-3}$, but contains two surface depletion regions (the drain-gate and source-gate) that have an ionized doping of $1 \times 10^{13} cm^{-3}$. These regions are used to model the interface states that are usually present in devices made from ZB-GaN and 3C-SiC. The simulation parameters are an ambient temperature of 300 K, a uniform grid with a spacing of 2.5 nm in both the x and z directions, 50,000 super particles, and a simulation time of 5 ps. The material parameters and band structures that are used in the simulator were given in Chapter 3.

5.3 Results

5.3.1 Simulator Verification

To verify the accuracy of the simulator, we first compare our simulation results for GaAs to those of Awano et al. [76]. The resulting low-voltage current-voltage characteristics (shown in Figure 27) for this 0.25μm MESFET are in very good agreement with Awano, et al., which verifies the validity of our simulator. The slight difference in the slopes of the I-V curves at higher gate voltages is due to the non-ideal numerical band structure we employ. Awano, et al. use an analytical band structure, where the mass is smaller throughout the entire Γ valley than in the full band model, which leads to higher currents at lower gate voltages. The slight differences between the fully-numerical band structure and the analytical band structure, at low energy, are due to EPM and the numerical errors of the discretization of the IW.

Next, to confirm the 3C-SiC results, we compared the zero-field mobility in 3C-SiC to results from experiments [27]. The results from the mobility simulation are shown in Figure 28. The two solid lines show the range of experimental values from the experiments, while the dotted line is from our simulation of bulk 3C-SiC. Zero-field mobilities are notoriously hard to calculate in a Monte Carlo simulator, because there is no field to drive the electrons. The entire simulation is based on the scattering rates which are, by definition, discrete. However, for the range of impurity concentrations present in the device, our simulator gives very good agreement, and at lower concentrations, it still provides good agreement, with a difference of about

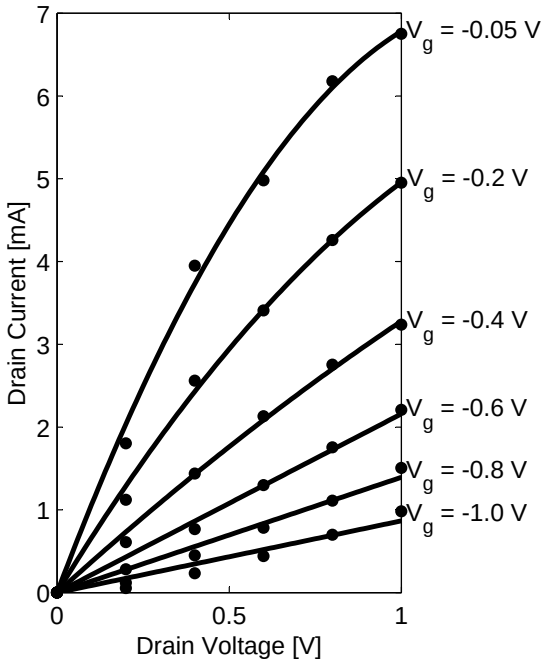

Figure 27: Low-voltage simulation results for a GaAs MESFET. The points are simulation results from Awano, et al., and the solid lines are simulation results from the simulator in this work.

35%. The high concentration region provides higher accuracy because of the significant increase in the impurity scattering rate. This increase gives the Monte Carlo simulator more scatterings per time, which increases the accuracy of the results by making the scatterings more continuous.

5.3.2 DC Breakdown

The calculated drain currents vs. drain-source voltages for ZB-GaN, 3C-SiC and GaAs are shown in Figure 29. The drain-source voltage varies for each material, and the gate-source voltage includes -0.1 V and -1.1 V. The Schottky barrier potential height is included in V_{gs}. The currents are calculated with and without impact ionization at each gate voltage and drain-source voltage. Using the new definition of the DC breakdown voltage, at a gate-source bias of -0.1 V, the breakdown voltage for

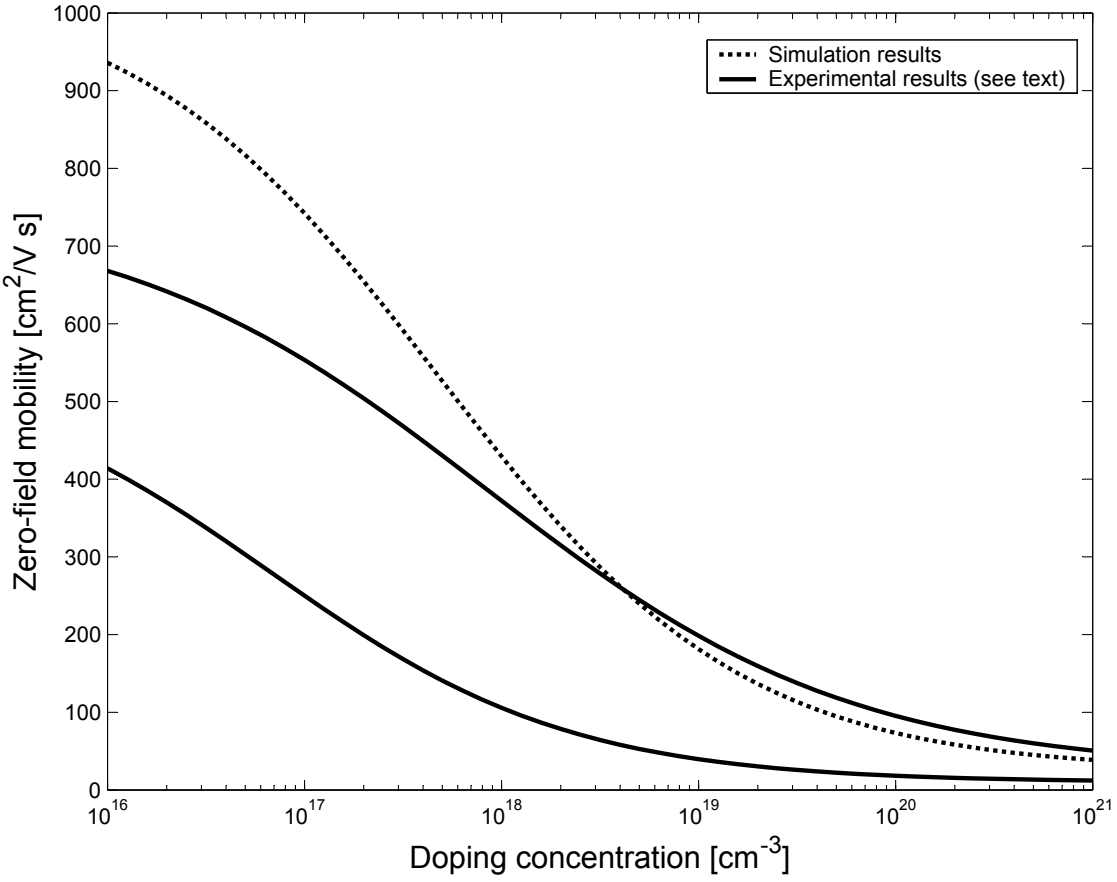

Figure 28: Comparison of zero-field mobility in 3C-SiC with experiment. The two solid lines indicate the range of experimental values.

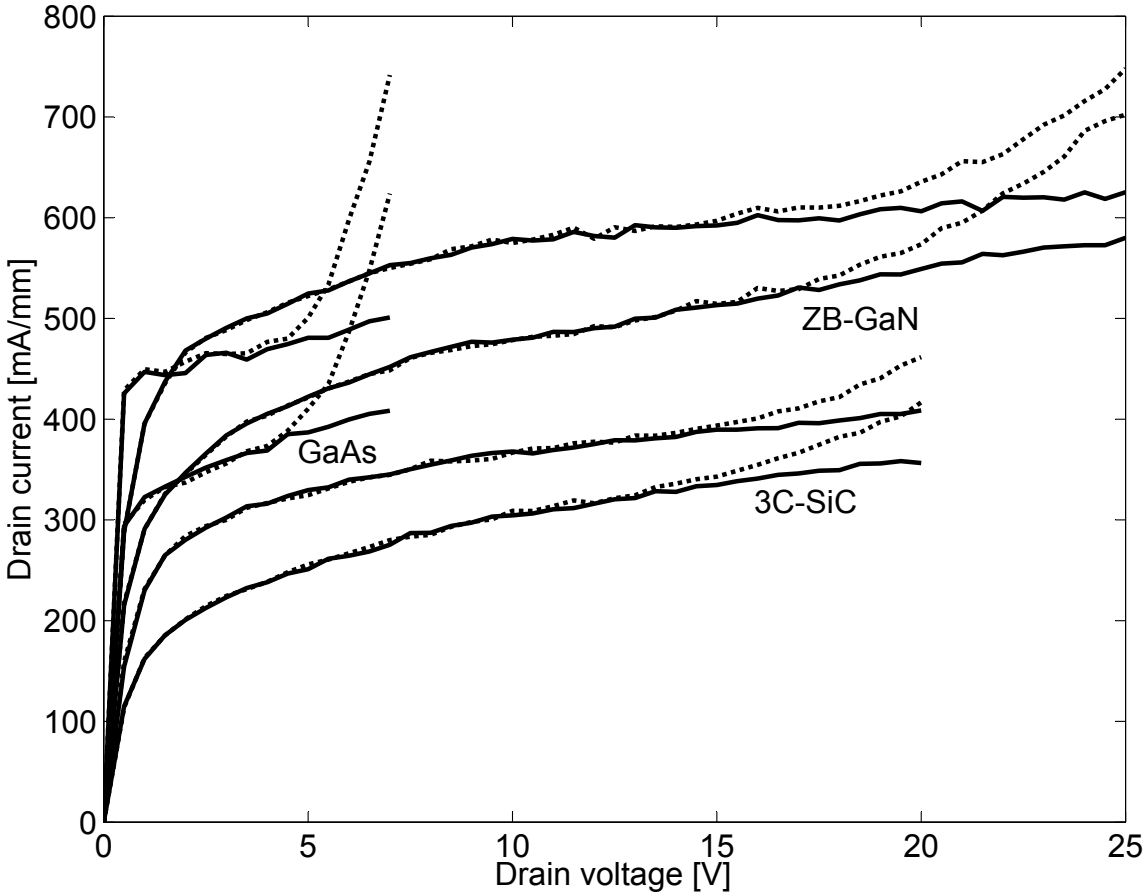

Figure 29: The output characteristics of the MESFET showing DC breakdown. For each material, there are two gate voltages present: -0.1 V and -1.1 V for the higher and lower current curve, respectively. In addition, the drain current is calculated twice, once with impact ionization (dotted lines) and once without impact ionization (solid lines). The DC breakdown voltage is calculated as described in the text.

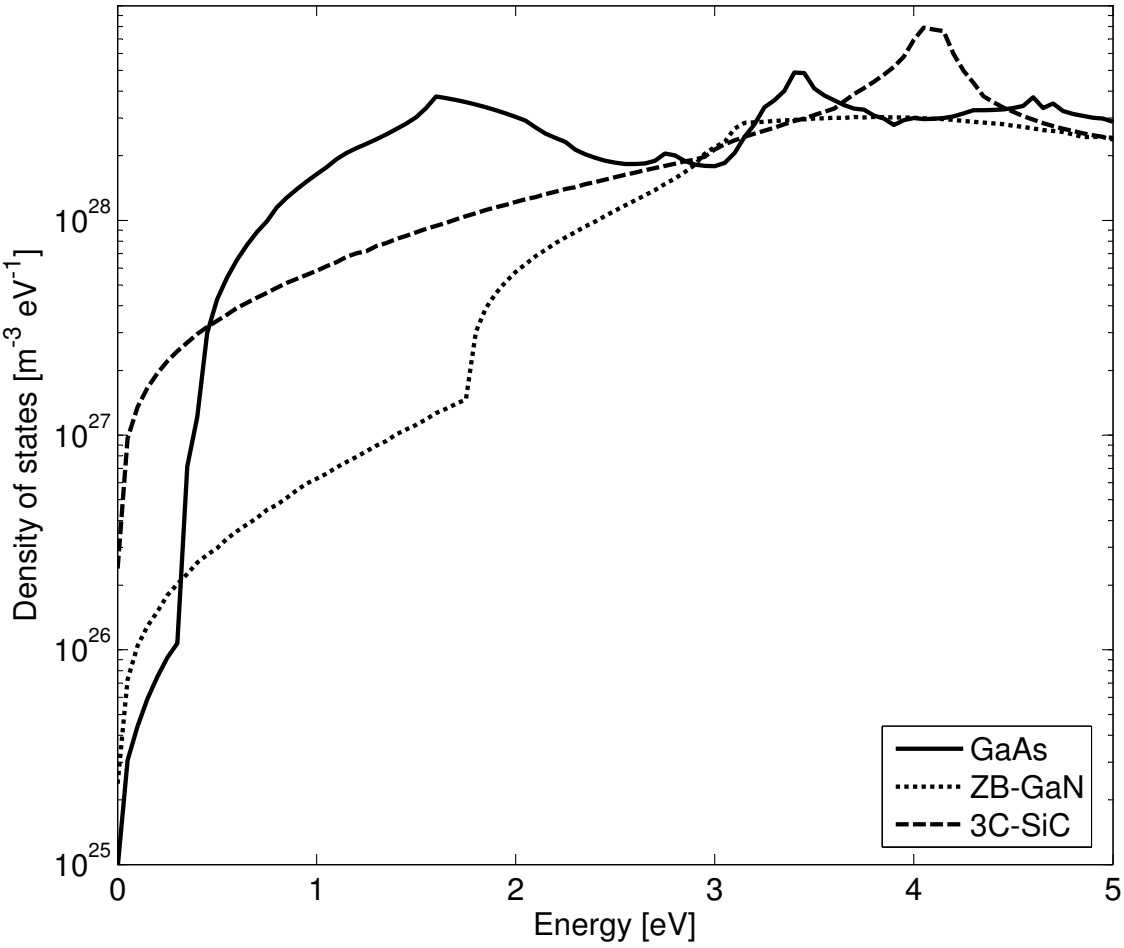

Figure 30: The density of states for GaAs, ZB-GaN, and 3C-SiC as a function of energy.

GaAs, 3C-SiC and ZB-GaN are approximately 5 V, 16 V, and 18 V, respectively.

This sequence of breakdown voltages is expected simply based on the relative values of the energy gap; however, the energy gap does not fully determine the breakdown condition. In general, two conditions determine impact ionization-induced breakdown. These are the impact ionization transition rate, which in turn is a strong function of the bandgap, and the rate at which the carriers heat up to energies where impact ionization can occur. The latter condition is a strong function of the density of states. The density of states for each material is shown in Figure 30. This figure

shows that the density of states in 3C-SiC is much higher at low energies than the density of states of ZB-GaN and GaAs, because 3C-SiC is an indirect-bandgap material. ZB-GaN and GaAs have only the single Γ-valley states at low energies, whereas 3C-SiC has six X-valley states. The larger number of states in the low energy region means that the electrons in 3C-SiC heat slower than do the electrons in ZB-GaN and GaAs. For a given low-voltage bias condition, the electrons in a 3C-SiC device are, on average, cooler than the electrons in a ZB-GaN (or GaAs) device. However, since the threshold energy for impact ionization is significantly lower in 3C-SiC than in ZB-GaN, breakdown is still reached in 3C-SiC before that in ZB-GaN.

5.3.3 Average Energy

It is also useful to examine the spatial average energy of electrons in the device (Figure 31). The gate-source voltage for the mean electron energy calculations is -0.1 V, and the drain-source voltage remains constant at 5 V. The energy is averaged over all of the electrons with the same x-grid point (where the x-direction is defined in Figure 26) for each grid point in the x-direction. The differences in the average-energy distribution reiterate the density-of-states argument stated before. Electrons in GaAs at breakdown have a very high average energy. The reason it achieves such energies is because of its relatively small density-of-states and its small electron mass. The electrons heat up quickly in GaAs. Comparing ZB-GaN and 3C-SiC we see that 3C-SiC does indeed have a cooler electron distribution. Again, this is due to the fact that 3C-SiC is an indirect material and has a significantly higher density-of-states, at low energies, than does either ZB-GaN or GaAs.

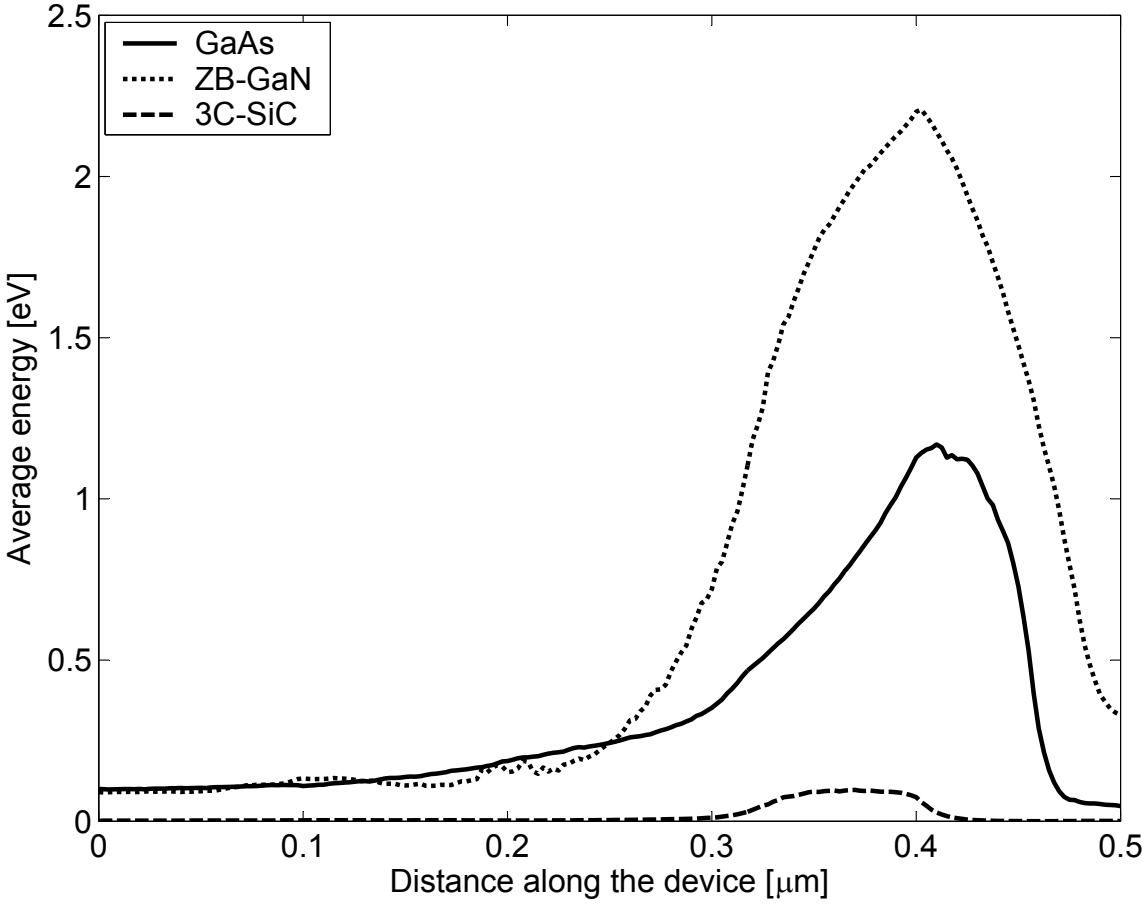

Figure 31: The spatial average-energy through the device for each material. The drain voltage is 5 V for all materials and the gate voltage is -0.1 V. The mean energy is calculated by averaging the electron energy of every electron with the same x-grid position.

The band population of electrons throughout the device is shown in Figure 32. The spatial band population is computed by summing the number of electrons that populate the second conduction band in the z-direction. The percentage of penetration is shown on the y-axis. Only GaAs and 3C-SiC (V_d = 5 V for GaAs, V_d = 15 V for 3C-SiC, and V_g = -0.1 V for both) are shown, because there are no electrons in the second band in ZB-GaN, because the energy of the second band is greater than the threshold energy of impact ionization. Even in GaAs and 3C-SiC, the population is very small, because the device is just entering the multiplication region, and complete breakdown occurs with few impact-ionization events. The band population reinforces the high-energy, high-field regions of the MESFET, with the peak of the high-fields being at the end of the drain contact.

5.3.4 Velocity

The velocity-vector plots in Figure 33 again show the active regions of the device. The graphs show the final average-electron velocity for a drain voltage equal to the breakdown voltage (5 V for GaAs, 16 V for 3C-SiC, and 18 V for ZB-GaN) and a gate voltage of -0.1 V. The depletion region under the gate contact is readily seen, as well as the edge-effects near the 0.5μm side of the device. As expected, the current-carrying region of the MESFET extends from the source, around the depletion region, to the near side of the drain contact.

5.3.5 Conclusions

The DC breakdown characteristics of the ZB-GaN, 3C-SiC, and GaAs MESFETs are determined. ZB-GaN and 3C-SiC have a similar DC breakdown voltage, with both

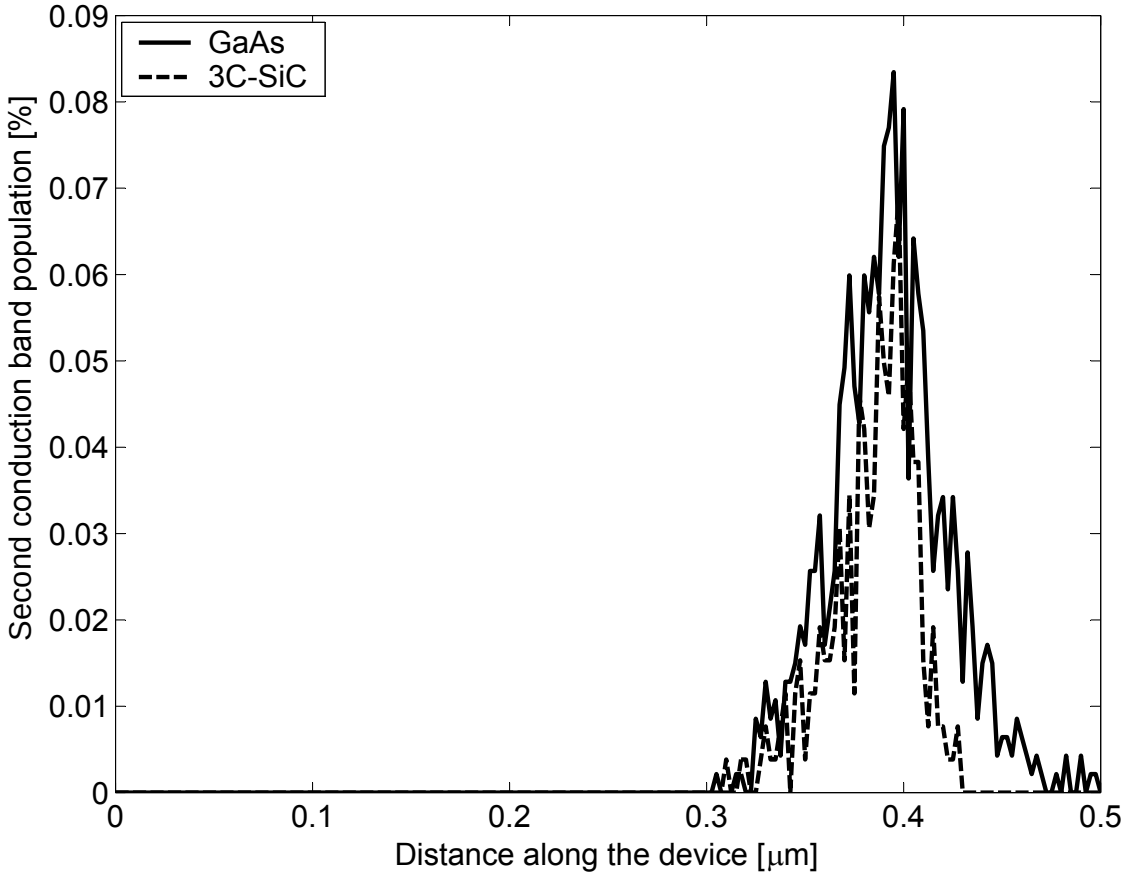

Figure 32: The second conduction band population percentage for GaAs and 3C-SiC. The population is taken at the breakdown voltage for each material. The percentage is calculated by counting all of the electrons that populate the second band with the same x-grid position. The population of ZB-GaN is not shown because the second band population in this material is zero.

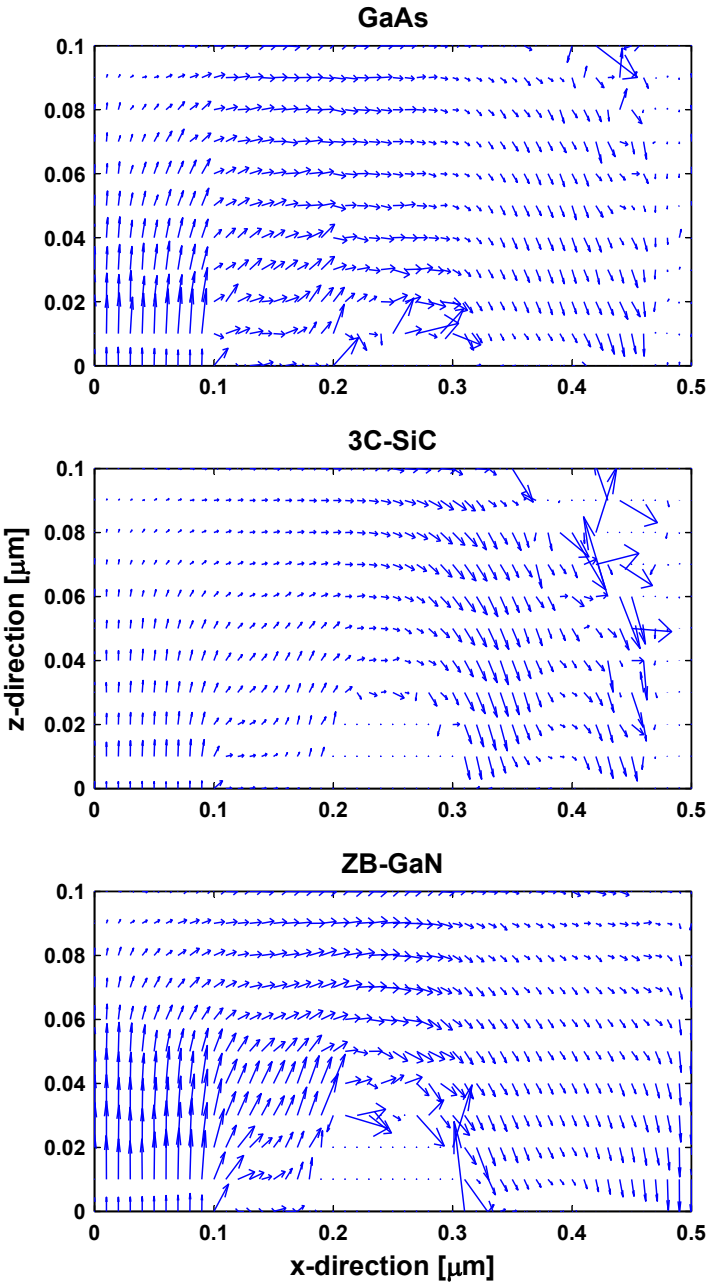

Figure 33: The electron velocity vector plot throughout the MESFET for each material. The drain voltage of the data for each material is the DC breakdown voltage for that material. The length of the vector is proportional to the magnitude of the average velocity, and the arrow points in the direction of the average velocity for that location.

being approximately a factor-of-four greater than the DC breakdown voltage of GaAs. 3C-SiC has a high DC breakdown voltage because of both its relatively large energy gap and its very large low-energy density of states, which results in a cooler device than in either ZB-GaN or GaAs.

From this work, it is found that the MESFET devices made from the wide-bandgap materials perform significantly better than those of the smaller bandgap material, GaAs. It should be noted that due to the inherent uncertainties in the band structure, phonon scattering rates, and impact ionization coefficients, the calculations presented serve only as general guidelines to the expected performance of both the ZB-GaN and 3C-SiC. Until there is a more thorough body of experimental results for these emerging semiconductors, it is only possible to provide qualitative analyses of MESFET devices. Even so, it can be expected that both ZB-GaN and 3C-SiC amplifier designs will provide more power than an equivalent GaAs design.

CHAPTER VI

MESFET RADIO-FREQUENCY BREAKDOWN

With the DC simulations complete, the second analysis made is the comparison of the enhancement of device breakdown during radio-frequency (RF) operation for these materials. The details of these analyses are given in this chapter. First, a brief description of the theory of RF breakdown is given, followed by the implementation details, and finally the results of the simulations.

6.1 Theory

Device RF breakdown is a very important effect in the design of high-power semiconductor devices. When these devices are used in high-power, high-frequency applications, the devices can be operated beyond DC breakdown [77–81]. Since the breakdown voltage under RF conditions is higher than that under DC conditions, the maximum output power can be greater under RF excitation than under DC conditions.

The reason that the high-frequency breakdown is higher than the DC breakdown is because of the reaction time of the carriers in the device. If the carriers reacted instantaneously to the change in bias during the RF excitation, then once the bias crossed the DC breakdown level the device would break down. However, they do not react instantaneously. The carrier reaction time is a function of the device material,

the device structure, and the bias condition. At high operating frequencies, the bias voltage is changing faster than the carriers can react, so there is a delay in the heating of the carriers (for that bias). In effect, the RF excitation is creating a virtual breakdown bias (near the RF large-signal peaks) that is below the DC breakdown voltage and is dependent on the frequency of the excitation. If the large signal excitation falls below its peak voltage before the carriers heat to the DC breakdown point then breakdown is suspended. This effect is shown in Figure 34, where V2 represents the DC breakdown voltage of a device and $f1, f2, f3, f4$ are the frequencies of the excitation with $f4 > f3 > f2 > f1$. In this simple illustration, the black curve represents the RF bias applied to the terminals of the device, and the red curve represents the reaction of the carriers to that bias. We assume that if the red curve touches the V2 on the black curve, breakdown occurs.

6.2 Implementation

The methodology for computing the RF breakdown is more complicated than that with DC breakdown because of the different nature of the processes involved, namely the fact that the process is no longer steady state, but rather the process is time dependent. Consequently the non-equilibrium distribution function (and its tail that determines the breakdown) changes in time. An overview of the process is as follows. First a base frequency is selected, which is the starting point for the RF calculations. At that frequency an RF excitation is found that produces a fixed amount of breakdown in the device (beyond the normal DC amount). The same frequency and same amount of breakdown is chosen for each material; however, because the DC

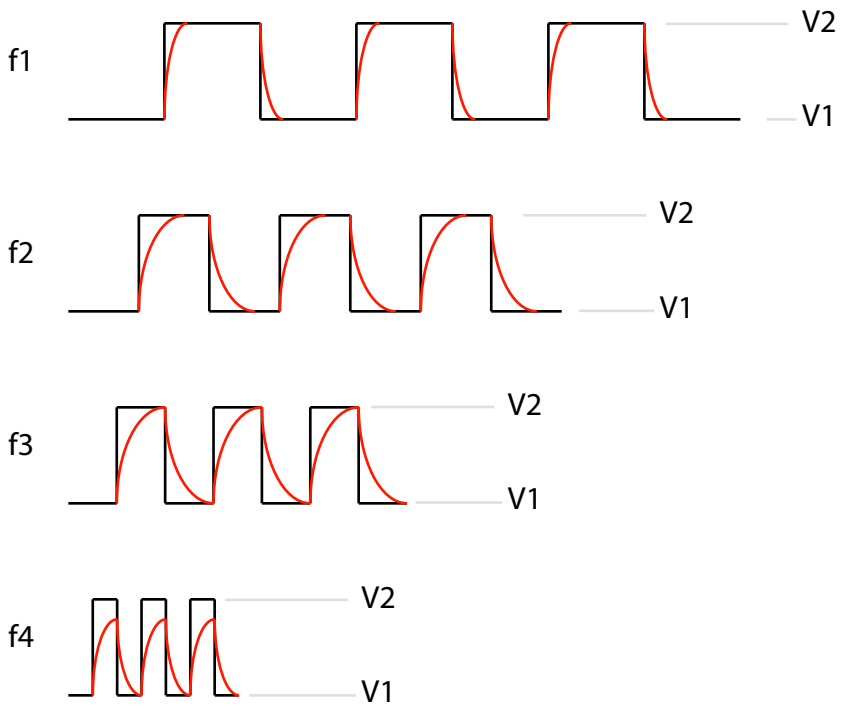

Figure 34: Illustration of the effect of RF excitation. V2 represents the DC breakdown voltage of a hypothetical device and $f1, f2, f3, f4$ are the frequencies of the excitation with $f4 > f3 > f2 > f1$. In this simple illustration, the black curve represents the RF bias applied to the terminals of the device, and the red curve represents the reaction of the carriers to that bias.

breakdown of each material is different, the amplitude of the RF excitation for each material will be different. Now that all of the materials are starting from the same RF breakdown point, the frequency (with the same bias) of the excitation is increased. This will cause the amount of breakdown to decrease with increasing frequency. The frequency at which the breakdown ceases is termed the "RF breakdown frequency." The relationship between the RF breakdown bias and the RF breakdown frequency is reversed: the lower the RF breakdown frequency the higher the RF bias can be without device breakdown occurring.

The RF breakdown frequency will be different for each material because of differences in the band structure and material transport properties. And since, each device structure is the same, and the RF excitation starting point is the same, the result is only based on the characteristics of the material. A material with a lower RF breakdown frequency provides better high-frequency performance, because is is easier to cause breakdown to cease. In other words, for an equivalent high-frequency application, a larger RF excitation can be applied to this material without breakdown occurring.

The methodology for computing the RF breakdown of a device is as follows. A large-signal RF bias is applied between the drain and source, simulating on-state breakdown. Though in most standard common source configurations the RF signal is applied to the gate, this situation is more difficult and computationally expensive to simulate using the Monte Carlo method. The RF breakdown results that are presented are nevertheless useful in examining the effect on the breakdown voltage due to an RF excitation, since the frequency dependence of the carrier heating is

somewhat independent of the bias condition. The waveform applied to the drain contact is assumed to be sinusoidally varying between high and low voltages, V_{hi} and V_{low}, respectively, with angular frequency, ω (Eq. 35). The drain current is again (like under DC breakdown analysis) calculated under two conditions, with and without impact ionization, in order to determine the breakdown point.

$$V_{ds}(t) = (\frac{V_{hi} + V_{low}}{2}) - (\frac{V_{hi} - V_{low}}{2})cos(\omega t + \pi/2) \tag{35}$$

A $0.1\mu m$ gate-length MESFET is used for the RF breakdown calculations. The geometry and doping levels of the device are shown in Figure 35. This device is the same as that used in the computation of the DC breakdown. The ionized concentration in the device is uniform at $3\times10^{17}cm^{-3}$, but contains two surface depletion regions (the drain-gate and source-gate) that each have an ionized doping of $1 \times 10^{13}cm^{-3}$. These regions are used to model the interface states that are usually present in devices made from ZB-GaN and 3C-SiC. The simulation parameters are an ambient temperature of 300 K, a uniform grid with a spacing of 2.5 nm in both the x and z directions, and 50,000 super particles. The material parameters and band structures that are used in the simulator were given in Chapter 3.

The simulation time for RF simulation is different from that used in the DC calculations. In the DC calculations, a fixed simulation time of 5ps was used, which allowed the simulation to converge. In the RF simulations, more simulation time is needed because of the period of the RF excitation. In addition, because the Monte

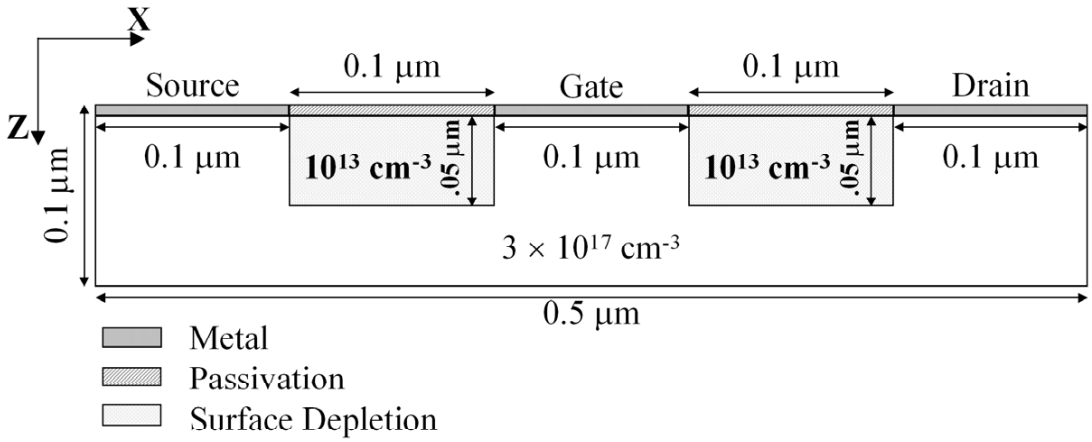

Figure 35: A cross-section of the simulated MESFET for RF breakdown. The contact locations and doping profiles are shown.

Carlo simulator needs time to compute the electron distribution throughout the device, the RF bias applied to the transistor cannot begin with the RF excitation at time zero. A slow ramp to the RF mid-point is needed to give the simulator time to compute the equilibrium electron distribution. If the ramp is too fast the simulator will end up in a non-physical distribution state. Figure 36 shows an example RF excitation for the ZB-GaN MESFET.

6.3 Results

6.3.1 RF Breakdown Starting Point

In order to compute the RF breakdown of the device, we need to determine a common starting point for all of the materials. The drain voltage (V_{ds}) has a RF bias voltage described by Eq. 35, and a gate voltage (V_{gs}) of -0.1 V. In these calculations, we are mainly interested in determining the frequency at which the device no longer experiences the breakdown condition for a given excitation. In order to achieve this (and taking into account the uncertainty of the current computed in a Monte Carlo

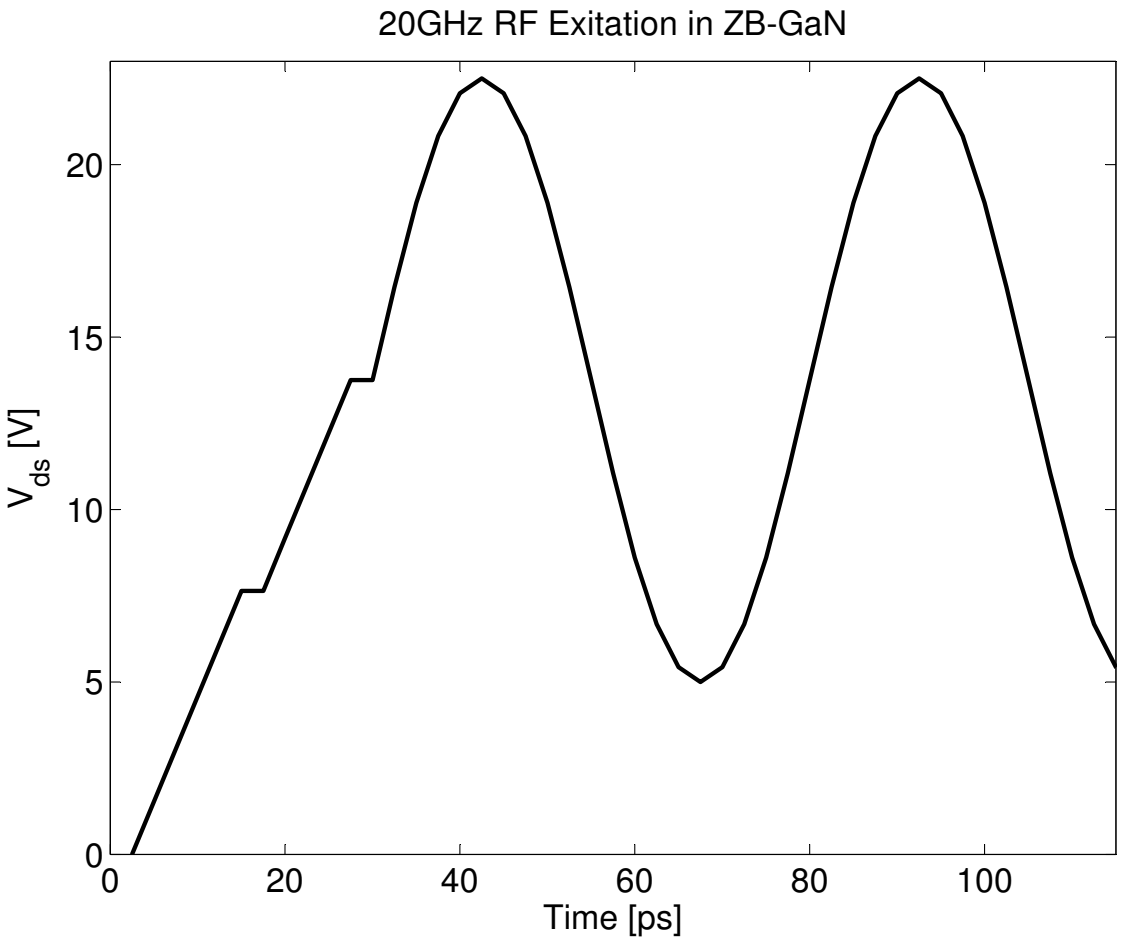

Figure 36: An example of the RF excitation voltage versus time for the ZB-GaN MESFET simulation. The simulation voltage ramps up to the mid-point of the RF excitation, then continues sinusoidally for two periods.

simulator), it is best to select a baseline bias condition such that the calculated drain currents with and without impact ionization are significantly different. To this end, the specific sinusoidal waveform (the V_{hi} and V_{low}) is found that produces a breakdown of 10% at a frequency of $\omega = 20$ GHz. First, a V_{low} point is chosen significantly below the DC breakdown point, then RF simulations are run with varying V_{hi} points around the DC breakdown point. Once these simulations are complete, a narrower range is found, and the process continues until a V_{hi} is found that produces the required breakdown. A sample result of the current (both with impact ionization and without) for the ZB-GaN material is shown in Figure 37.

The results of these simulations are found in Figures 38, 39, and 40, for materials GaAs, ZB-GaN, and 3C-SiC. The figures show the percent impact ionization throughout the simulation time. Like in the DC calculations, the percent impact ionization is computed as the percentage difference between the currents in a simulation with impact ionization off and one with impact ionization on. The resulting biases for the RF excitations are given by Eq. 36.

$$\begin{cases} V_{ds}(t) = 3.8 - 1.8cos(\omega t + \pi/2), & \text{for GaAs} \\ V_{ds}(t) = 13.75 - 8.75cos(\omega t + \pi/2), & \text{for ZB-GaN} \\ V_{ds}(t) = 11.7 - 7.7cos(\omega t + \pi/2), & \text{for 3C-SiC} \end{cases} \tag{36}$$

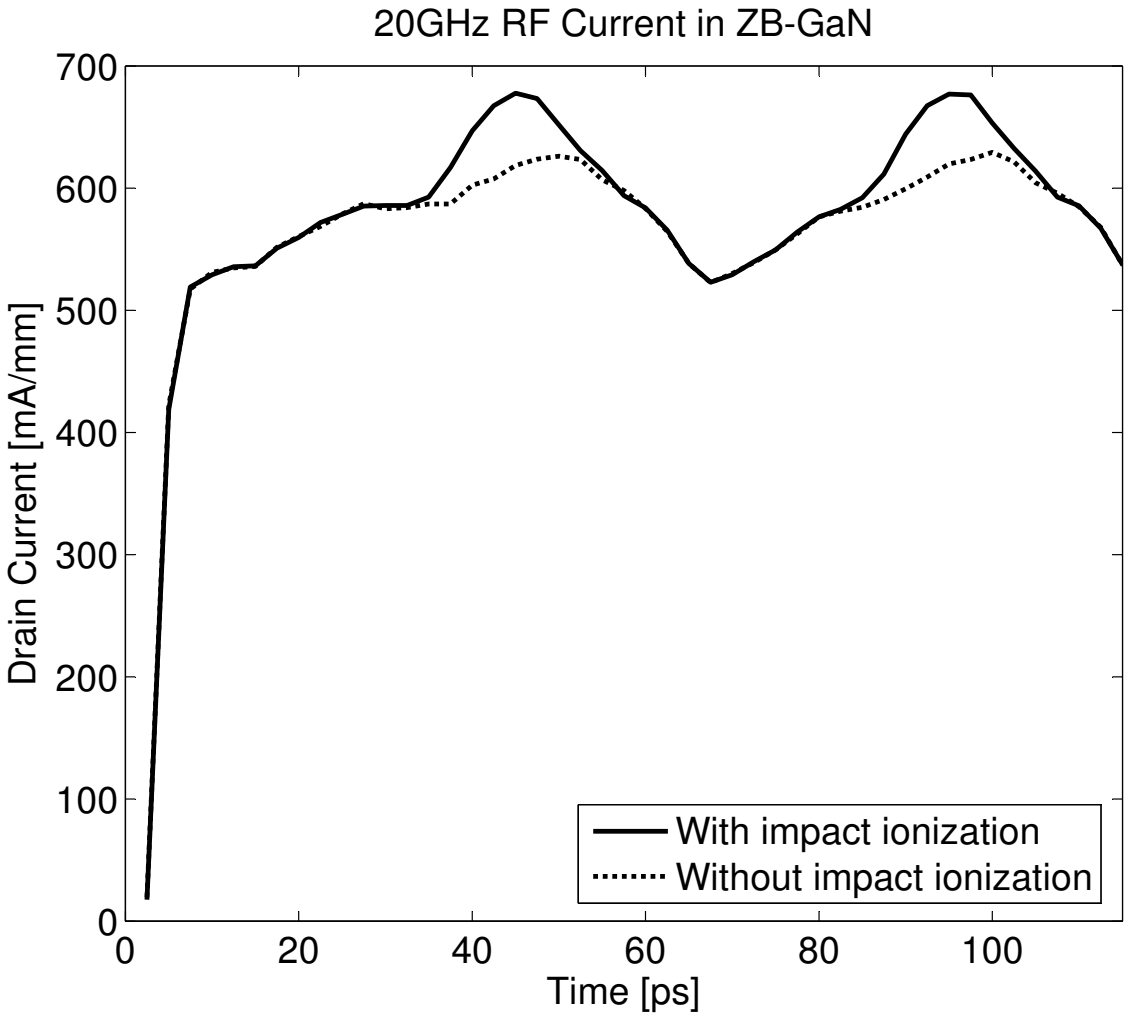

Figure 37: Sample current results of the RF simulation of a ZB-GaN MESFET. The frequency of the RF excitation is 20 GHz with $V_{ds}(t) = 13.75 - 8.75cos(\omega t + \pi/2)$. The results include the current both with impact ionization on and with impaction ionization off. The figure clearly shows the breakdown of the device.

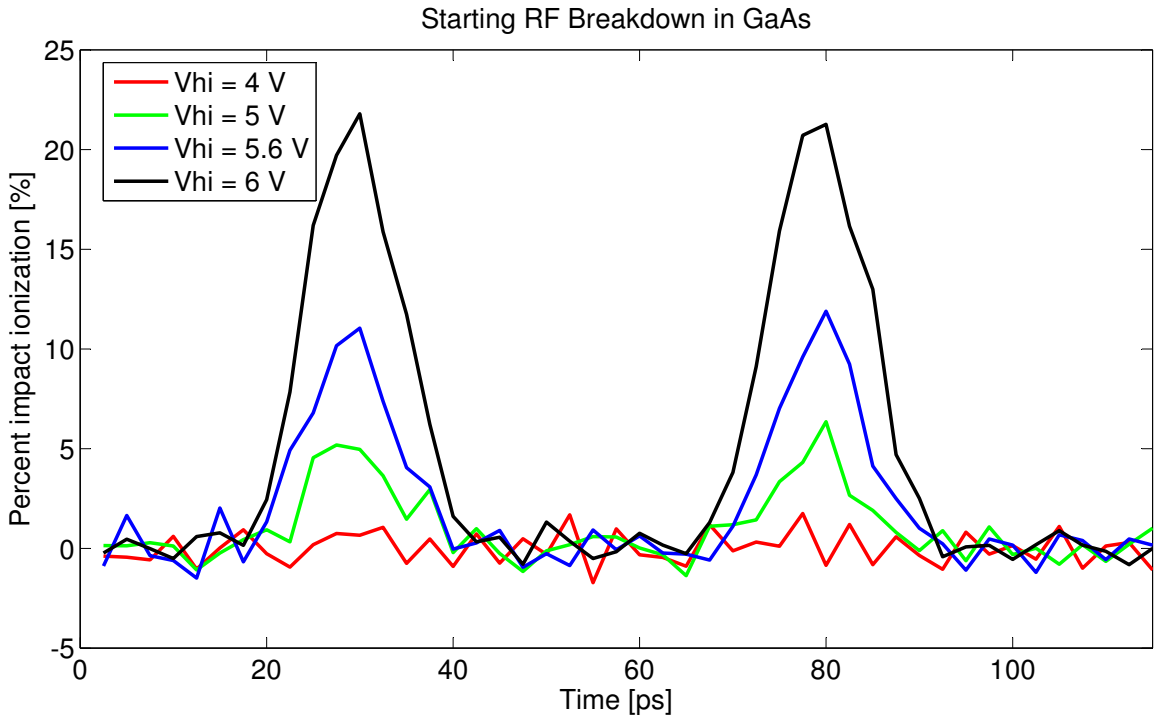

Figure 38: Computation of the RF breakdown starting point in a GaAs MESFET. The graph shows impact ionization percentage versus time for the two periods of the simulation. The drain voltage is varied in order to find the one that produces 10% of impact ionization at the peak.

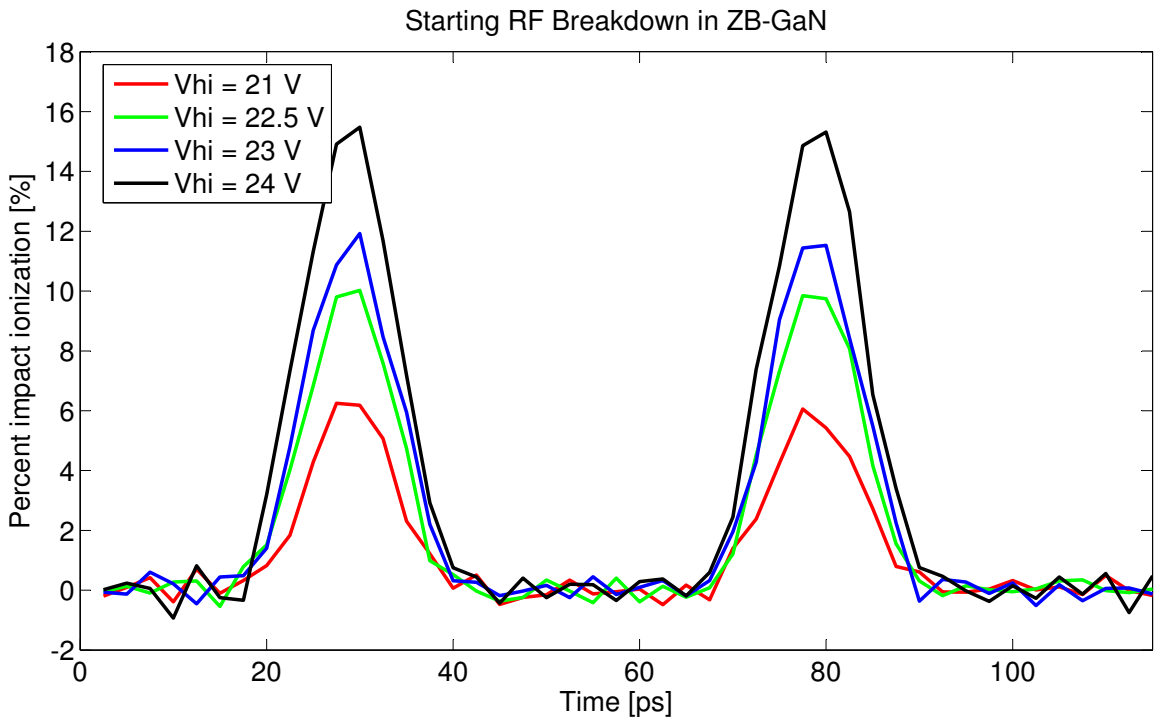

Figure 39: Computation of the RF breakdown starting point in a ZB-GaN MESFET. The graph shows impact ionization percentage versus time for the two periods of the simulation. The drain voltage is varied in order to find the one that produces 10% of impact ionization at the peak.

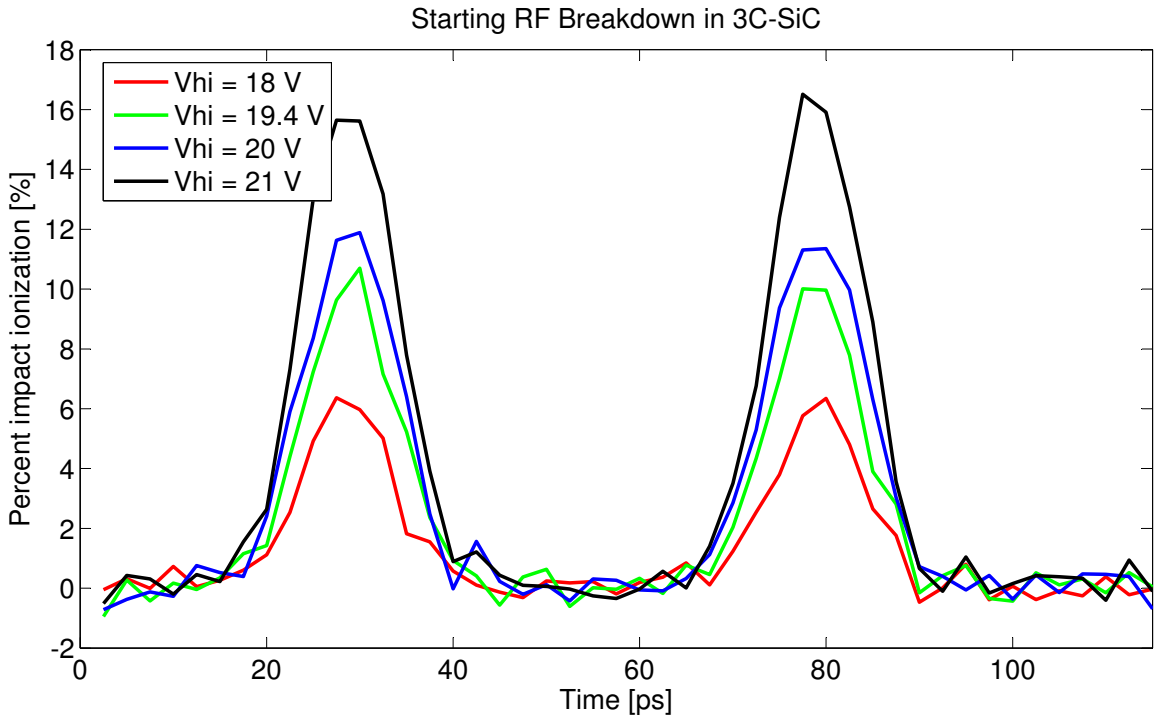

Figure 40: Computation of the RF breakdown starting point in a 3C-SiC MESFET. The graph shows impact ionization percentage versus time for the two periods of the simulation. The drain voltage is varied in order to find the one that produces 10% of impact ionization at the peak.

6.3.2 RF Breakdown

With a suitable starting point for each material, the RF excitation frequency is increased until the device no longer exhibits breakdown (the condition where the calculated drain currents with and without impact ionization drop below 3%). Due to the noise in the currents calculated from a Monte Carlo simulation it is useful to plot each frequency's breakdown, then fit a curve to the results. The RF breakdown results are shown in Figure 41.

The resulting RF breakdown results are 80 GHz, 130 GHz, and 180 GHz for GaAs, 3C-SiC, and ZB-GaN, respectively. It is interesting to note that both GaAs and 3C-SiC have a lower RF breakdown frequency than does ZB-GaN (which means that they can handle larger relative RF excitations without breaking down). Of course, in a GaAs MESFET, the power level at any frequency will be much lower than in either 3C-SiC or ZB-GaN, because the DC breakdown is much lower. However, when only comparing the enhancement of device breakdown during RF excitation, GaAs is better. As stated earlier, it was suggested that as the frequency of the excitation increases, the electrons can no longer fully respond to the changing electric field. As a result, their energy and, consequently, their ionization coefficient settles to an intermediate value between the value that would occur from a DC voltage at the low point of the RF bias and value that would occur from a DC voltage at the high point of the RF bias. Thus for some frequencies, the carriers achieve an average energy below that needed for breakdown.

In a similar way that the shape and magnitude of the density of states (DOS)

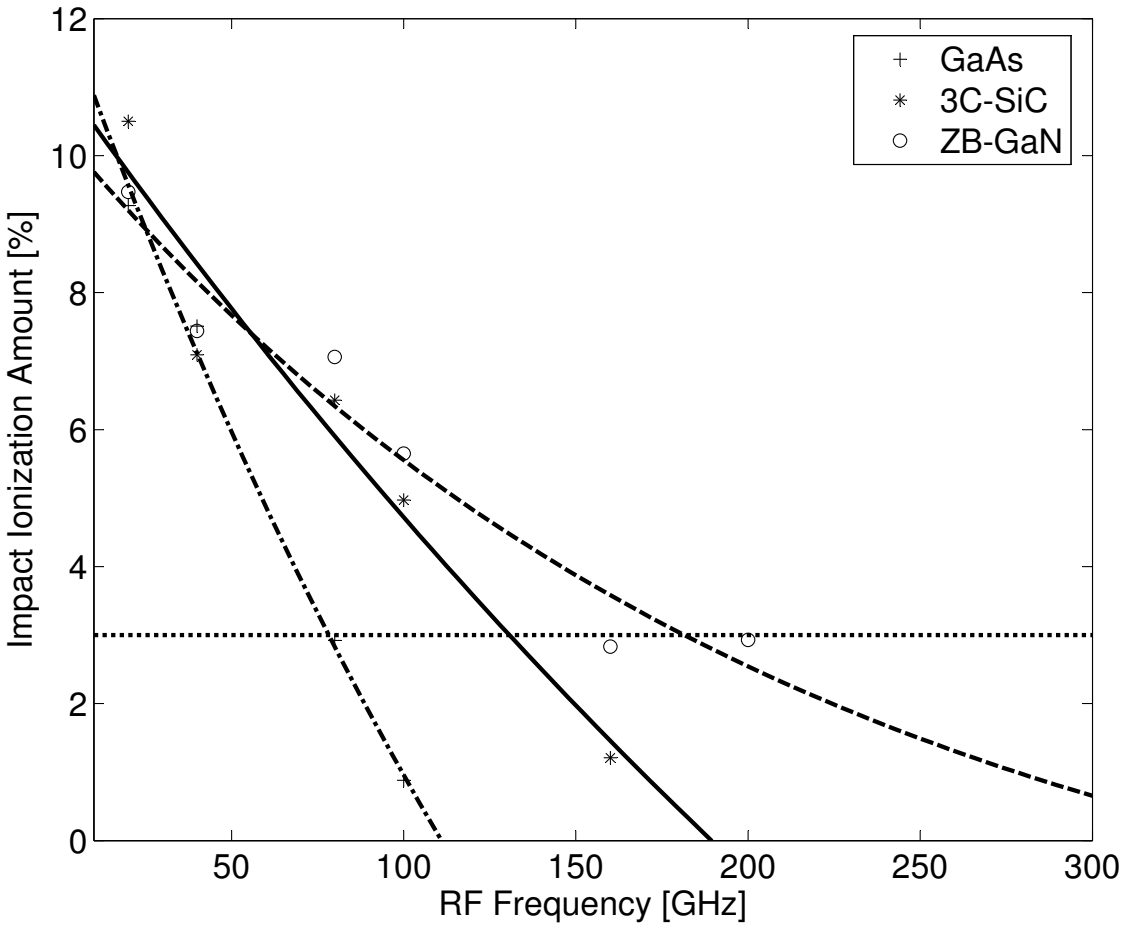

Figure 41: The RF breakdown results for GaAs, 3C-SiC, and ZB-GaN. The data points from the simulations are shown as dots, and the fit of the data is shown as a line. The RF breakdown frequency is found when the line crosses the 3% ionization line. The results are 80 GHz, 130 GHz, and 180 GHz for GaAs, 3C-SiC, and ZB-GaN, respectively.

help determine the DC breakdown, the DOS plays a large role in the determination of the RF breakdown. In the case of DC breakdown, the low energy region of the DOS plays the important role. Since the DC breakdown computation starts from a zero bias condition and increases until impact ionization is achieved, the low energy DOS produces electron inertia that slows the heating of electrons on the way toward breakdown (causing a higher DC breakdown). In the RF breakdown case, the electrons are already heated (from the ramp to the center of the RF bias), so the low energy DOS plays little role in the determination of RF breakdown (since the electrons are already beyond that point). Instead, the higher energy region between about 1eV and 3eV of the DOS comes into play. Figure 42 shows the DOS of each material in that region.

Contrary to the low energy DOS, where 3C-SiC dominates because the material is indirect, in the medium-energy DOS, GaAs dominates, with 3C-SiC following, and ZB-GaN the lowest. This follows exactly the ordering of the results from the RF breakdown calculation. So, physically, the electrons in GaAs cannot follow the RF signal as rapidly as they can in ZB-GaN. We believe that this is again due to the difference in the medium-energy DOS, resulting in a larger electron inertia in GaAs than exists in 3C-SiC and ZB-GaN. At high-energy DOS regions, the device is already beyond breakdown, so this section of the DOS does not come into play in MESFET analysis.

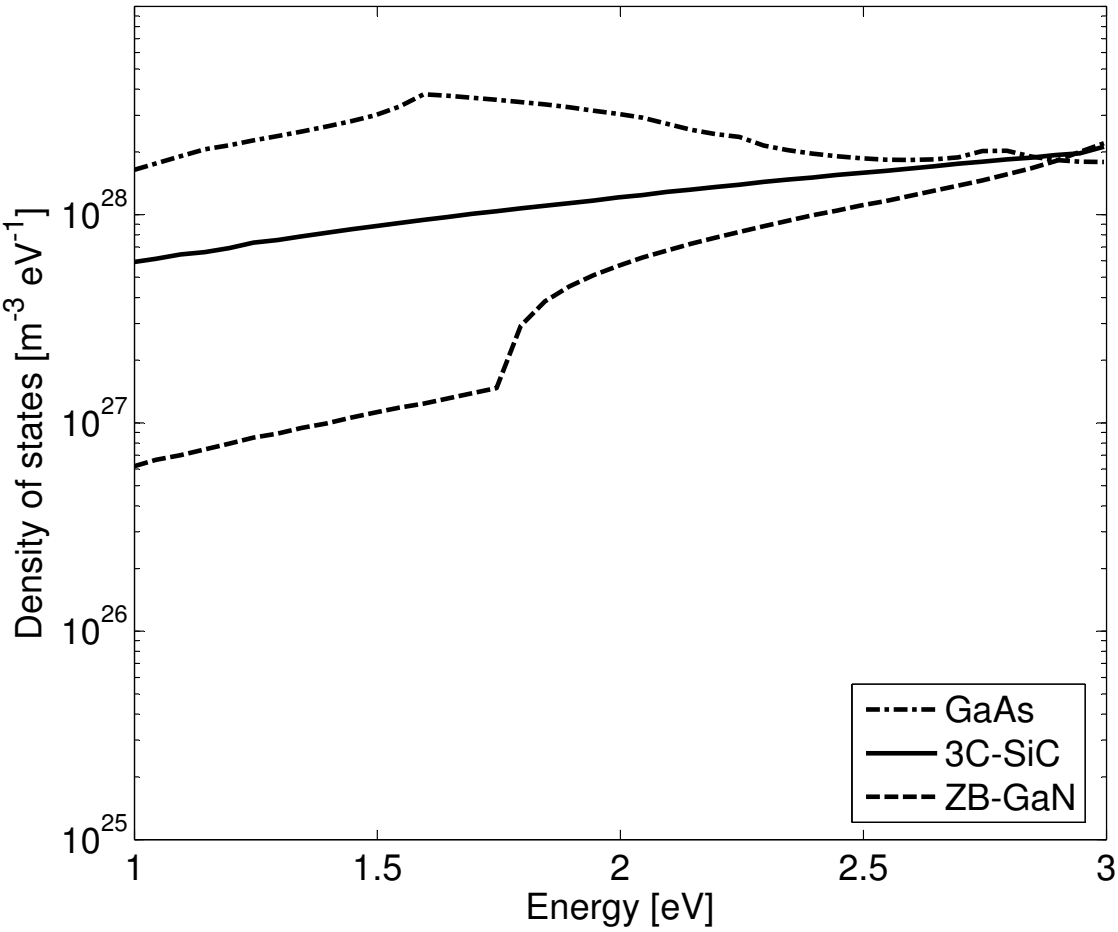

Figure 42: Plot of the density of states for GaAs, 3C-SiC, and ZB-GaN between 1eV and 3eV.

6.3.3 Conclusions

Investigation into the RF breakdown behavior of ZB-GaN, 3C-SiC, and GaAs MESFETs shows that a GaAs MESFET is found to suppress RF breakdown the best, with 3C-SiC second, and, finally, ZB-GaN. As the RF signal increases, the electrons can no longer fully respond to the changing electric field. The differences among the materials are found to be caused by the medium-energy DOS. The higher DOS exhibited in GaAs give the electrons in that device more inertia and prevents the electrons from reaching a high enough energy to produce impact ionization.

RF breakdown is a useful phenomenon that can allow a higher maximum output power from devices made of certain materials. Since an RF bias can prevent the breakdown of materials at voltages where DC breakdown would occur, devices under RF bias can use higher RF biases to produce larger amounts of output power. In this work, it is found that 3C-SiC may allow higher power high-frequency devices than possible with ZB-GaN devices, because the DC breakdowns in both materials are similar, and the RF breakdown in 3C-SiC is lower than that in ZB-GaN, allowing 3C-SiC to operate further beyond breakdown under RF excitations.

CHAPTER VII

SUMMARY AND FUTURE WORK

7.1 Summary of Results

The objective of the research was to analyze device performance for emerging cubic-phase wide-bandgap semiconductors. By comparing two wide-bandgap semiconductors, ZB-GaN and 3C-SiC, to a current, well-understood semiconductor, GaAs, we can understand the advantages and disadvantages of these two materials. This research involved writing a wholly new, full-band Monte Carlo simulator that was general enough to simulate all three materials. The simulator that was designed in this work allows the simulation of any cubic-phase material. With the proper electronic band structure and material parameters, a device made from any cubic-phase material can be simulated. Specifically, the advances that allow this flexibility are the numerical computation of the carrier scattering rates and the new electron final-state selection (i.e. the removal of electron valleys).

The carrier scattering rates are computed numerically for each semiconductor material using the new scattering rate convergence information described here [64]. In addition, the two fitting parameters allow materials with very little experimental or theoretical information available to be simulated. Most other simulators require extensive fitting to produce accurate results. For the materials of interest in this research, this information required by these fitting parameters is lacking.

The final-state selection algorithm uses the overlap integrals and the scattering rate dependencies in its calculation. This not only increases the accuracy of the simulation, it also allows the simulator to simulate indirect materials. Previous simulators that used half-analytical, half-numerical final-state selection could not do this, since the analytical portions of the algorithm failed to work when the conduction band minimum was not at Γ. Included in the final state selection is a new way to perform reverse-energy interpolation. By using a set of energy deltas instead of one, the MC simulator is both faster and more accurate, especially at higher energies.

The results from this work are the first comparison of the wide-bandgap semiconductor materials, ZB-GaN and 3C-SiC, to the smaller bandgap material GaAs. It is also the first published theoretical MESFET breakdown results for 3C-SiC. In addition, the ZB-GaN results are much improved over previous ones, owing to the improved fully-numerical final-state selection. In addition, a high-frequency analysis of the three materials was performed. The high-frequency analysis looked at the breakdown of a MESFET during RF operation. It was found that a MESFET can be pushed beyond DC breakdown during RF operation, which allows higher bias voltages, and higher output power. The combination of the DC breakdown analysis and the RF breakdown analysis provides a comprehensive analysis of the device operation of these cubic-phase wide-bandgap semiconductors.

7.2 Recommendations of Future Work

Although the Monte Carlo simulator designed in this work is implemented to include as much physics as possible, there are still some areas for improvement. The first

improvement (and probably the most difficult) would be to calculate numerically the phonon dispersion curves. In this work, the optical phonons are assumed to have a constant energy, while the acoustic phonon is assumed to be a well-behaved function of the wave-vector. The calculation of the phonon dispersion relations requires the use of a pseudo-rigid ion calculation. Although the calculation of the phonon dispersion relations would increase the accuracy of the calculated scattering rates, it requires many experimentally measured parameters. It is questionable whether the parameters would be available for the emerging materials found in this work and future works.

The second area for improvement is the use of k-dependent scattering rates. In the zincblende phase crystals, the inherent symmetries of the crystal allowed the assumption that the scattering rates are only dependent on the energy of the electron. If the simulator is extended to other crystal phases, this assumption will no longer be valid. A k-dependent scattering rate simulator will involve changes to both the simulator and the scattering rate calculations. The change to k-dependent scattering rates will involve both larger simulator memory requirements and larger computational requirements.

The final improvement that can be made is the extension of the simulator to support other crystal structures (most importantly, wurtzite). A wurtzite-phase simulator is much more data-intensive (and, thus, more memory-intensive). First of all, as mentioned before, the simulator will need to have k-dependent scattering rates. The irreducible wedge of wurtzite is larger than that in zincblende, so the size of the scattering rate computations will be much bigger. In addition, there are often 12 conduction bands in wurtzite phases materials, which means that the band structures

will be larger. Both of these requirements will mean that the simulators will require more memory and more computational power to provide reasonable simulation times. But with the success of a wurtzite-phase simulator comes a great number of additional materials to analyze, which can provide a larger picture of DC and RF breakdown in MESFET devices.

REFERENCES

[1] M. Razeghi and A. Rogalski, "Semiconductor ultraviolet detectors," *Journal of Applied Physics*, vol. 79, pp. 7433–73, 1996.

[2] T. Li, D. J. H. Lambert, M. M. Wong, C. J. Collins, B. Yang, A. L. Beck, U. Chowdhury, R. D. Dupuis, and J. C. Campbell, "Low-noise back-illuminated AlGaN based p-i-n solar-blind ultraviolet photodetectors," *IEEE Journal of Quantum Electronics*, vol. 37, pp. 538–45, 2001.

[3] S. Nakamura, M. Senoh, S.-I. Nagahama, N. Iwasa, T. Yamada, T. Matsushita, Y. Sugimoto, and H. Kiyoku, "Room-temperature continuous-wave operation of InGaN multi-quantum-well-structure laser diodes with a long lifetime," *Appl. Phys. Lett.*, vol. 70, pp. 868–70, 1997.

[4] S. Verghese, K. A. McIntosh, R. J. Molnar, L. J. Mahoney, R. L. Aggarwal, M. W. Geis, K. M. Molvar, E. K. Duerr, and I. Melngailis, "GaN avalanche photodiodes operating in linear-gain mode and Geiger mode," *IEEE Transactions on Electron Devices*, vol. 48, pp. 502–10, 2001.

[5] R. J. Trew, "SiC and GaN transistors - is there one winner for microwave power applications?" *Proceedings of the IEEE*, vol. 90, no. 6, pp. 1032–47, 2002.

[6] U. K. Mishra, P. Parikh, and Y.-F. Wu, "AlGaN/GaN HEMTs - An overview of device operation and applications," *Proceedings of the IEEE*, vol. 90, pp. 1022–31, 2002.

[7] P. M. Asbeck, E. T. Yu, S. S. Lau, G. J. Sullivan, J. V. Hove, and J. Redwing, "Piezoelectric charge densities in AlGaN/GaN HFETs," *Electronic Letters*, vol. 33, pp. 1230–1, 1997.

[8] Y.-F. Wu, B. P. Keller, P. Fini, S. Keller, T. J. Jenkins, L. T. Kehias, S. P. Denbaars, and U. K. Mishra, "High Al-content AlGaN/GaN MODFETs for ultrahigh performance," *IEEE Electron Device Letters*, vol. 19, pp. 50–3, 1998.

[9] H. Morkoc, A. D. Carlo, and R. Cingolani, "GaN-based modulation doped FETs and UV detectors," *Solid State Electronics*, vol. 46, pp. 157–202, 2002.

[10] J. D. Albrecht, R. P. Wang, P. P. Ruden, M. Farahmand, and K. F. Brennan, "Electron transport characteristics of GaN for high temperature device modeling," *Journal of Applied Physics*, vol. 83, pp. 4777–81, 1998.

[11] B. E. Foutz, L. F. Eastman, U. V. Bhapkar, and M. S. Shur, "Comparison of high field electron transport in GaN and GaAs," *Applied Physics Letters*, vol. 70, no. 21, pp. 2849–51, 1997.

[12] N. Mansour, K. W. Kim, N. A. Bannov, and M. A. Littlejohn, "Transient ballistic transport in GaN," *Journal of Applied Physics*, vol. 81, pp. 2901–3, 1997.

[13] S. O. ane B. E. Foutz, M. S. Shur, U. V. Bhapkar, and L. F. Eastman, "Electron transport in wurtzite indium nitride," *Journal of Applied Physics*, vol. 83, pp. 826–8, 1998.

[14] J. Kolník, I. H. Oguzman, K. F. Brennan, W. Rongping, P. P. Ruden, and Y. Wang, "Electronic transport studies of bulk zincblende and wurtzite phases of GaN based on an ensemble Monte Carlo calculation including a full zone band structure," *Journal of Applied Physics*, vol. 78, no. 2, pp. 1033–8, 1995.

[15] J. Kolník, I. H. Oguzman, K. F. Brennan, W. Rongping, and P. P. Ruden, "Monte Carlo calculation of electron initiated impact ionization in bulk zincblende and wurtzite GaN," *Journal of Applied Physics*, vol. 81, no. 2, pp. 726–33, 1997.

[16] E. Bellotti, B. K. Doshi, K. F. Brennan, J. D. Albrecht, and P. P. Ruden, "Ensemble Monte Carlo study of electron transport in wurtzite InN," *Journal of Applied Physics*, vol. 85, no. 2, pp. 916–23, 1999.

[17] M. Bhatnagar and B. J. Baligla, "Comparison of 6H-SiC, 3C-SiC, and Si for power devices," *IEEE Transactions on Electron Devices*, vol. 40, no. 3, pp. 645–55, 1993.

[18] C. E. Weitzel, J. W. Palmour, J. C. H. Carter, K. Moore, K. K. Nordquist, S. Allen, C. Thero, and M. Bhatnagar, "Silicon carbide high-power devices," *IEEE Transactions on Electron Devices*, vol. 43, no. 10, pp. 1732–41, 1996.

[19] J. A. Cooper, "Advances in SiC MOS technology," *Physica Status Solidi A*, vol. 162, no. 1, pp. 305–20, 1997.

[20] A. Elasser and T. P. Chow, "Silicon carbide benefits and advantages for power electronics circuits and systems," *Proceedings of the IEEE*, vol. 90, no. 6, pp. 969–86, 2002.

[21] M. Ruff, H. Mitlehner, and R. Helbig, "SiC devices: physics and numerical simulation," *IEEE Transactions on Electron Devices*, vol. 41, no. 6, pp. 1040–54, 1994.

[22] C. E. Weitzel, "Comparison of SiC, GaAs, and Si RF MESFET power densities," *IEEE Electron Device Letters*, vol. 16, no. 10, pp. 451–3, 1995.

[23] R. Mickevičius and J. H. Zhao, "Comparative Monte Carlo study of electron transport in 3C, 4H and 6H silicon carbide," *Materials Science Forum*, vol. 264-268, pp. 291–4, 1998.

[24] E. Bellotti, H.-E. Nilsson, K. F. Brennan, P. P. Rude, and R. Trew, "Monte Carlo calculation of hole initiated impact ionization in 4H phase SiC," *Journal of Applied Physics*, vol. 87, no. 8, pp. 3864–71, 2000.

[25] H.-E. Nilsson, E. Bellotti, M. Hjelm, and K. F. Brennan, "A comparison between different Monte Carlo models in simulation of hole transport in 4H-SiC," *Mathematics and Computers in Simulation*, vol. 55, no. 1-3, pp. 199–208, 2001.

[26] H.-E. Nilsson, E. Bellotti, K. F. Brennan, and M. Hjelm, "A full band Monte Carlo study of high field carrier transport in 4H-SiC," *Materials Science Forum*, vol. 338-342, pt. 1, pp. 338–42, 2000.

[27] M. Roschke and F. Schwierz, "Electron mobility models for 4H, 6H and 3C SiC," *IEEE Transactions on Electron Devices*, vol. 48, no. 7, pp. 1442–7, 2001.

[28] E. Bellotti, H.-E. Nilsson, K. F. Brennan, and P. P. Ruden, "Ensemble Monte Carlo calculation of hole transport in bulk 3C-SiC," *Journal of Applied Physics*, vol. 85, no. 6, pp. 3211–17, 1999.

[29] H.-E. Nilsson, U. Englund, M. Hjelm, E. Bellotti, and K. F. Brennan, "Full band Monte Carlo study of high field transport in cubic phase silicon carbide," *Journal of Applied Physics*, vol. 93, pp. 3389–94, 2003.

[30] M. Weber, L. Tirino, K. Brennan, and M. Farahmand, "Theoretical study of RF breakdown in GaN wurtzite and zincblende phase MESFETs," *Journal of Computational Electronics*, vol. 1, pp. 235–9, 2002.

[31] M. Farahmand and K. F. Brennan, "Comparison between wurtzite phase and zincblende phase GaN MESFETs using a full band Monte Carlo simulation," *IEEE Transactions on Electron Devices*, vol. 47, no. 3, pp. 493–7, 2000.

[32] E. Bellotti, B. Doshi, K. F. Brennan, P. P. Ruden, S. J. Pearton, C. Kuo, A. F. Wright, and T. Uenoyama, "Ensemble Monte Carlo study of electron transport in bulk indium nitride," *GaN and Related Alloys. Symposium*, pp. G6.59.1–6, 1999.

[33] K. F. Brennan, E. Bellotti, M. Farahmand, J. Haralson II, P. P. Ruden, J. D. Albrecht, and A. Sutandi, "Materials theory based modeling of wide band gap semiconductors: from basic properties to devices," *Solid-State Electronics*, vol. 44, no. 2, pp. 195–204, 2000.

[34] I. H. Oguzman, E. Bellotti, K. F. Brennan, J. Kolnik, R. Wang, and P. P. Ruden, "Theory of hole initiated impact ionization in bulk zincblende and wurtzite GaN," *Journal of Applied Physics*, vol. 81, no. 12, pp. 7827–34, 1997.

[35] U. V. Bhapkar and M. S. Shur, "Monte Carlo calculation of velocity-field characteristics of wurtzite GaN," *Journal of Applied Physics*, vol. 82, no. 4, pp. 1649–55, 1997.

[36] W. J. Fan, M. F. Li, T. C. Chong, and J. B. Xia, "Electronic properties of zinc-blende GaN, AlN, and their alloys $Ga_{1-x}Al_xN$," *Journal of Applied Physics*, vol. 79, no. 1, pp. 188–94, 1996.

[37] I. H. Oğuzman, J. Kolník, K. F. Brennan, R. Wang, T.-N. Fang, and P. P. Ruden, "Hole transport properties of bulk zinc-blende and wurtzite phases of GaN based on an ensemble Monte Carlo calculation including a full zone band structure," *Journal of Applied Physics*, vol. 80, no. 8, pp. 4429–36, 1996.

[38] M. Farahmand, K. F. Brennan, E. Gebara, D. Heo, Y. Suh, and J. Laskar, "Theoretical study of RF breakdown in bulk GaN and GaN MESFETs," *IEEE Transactions on Electron Devices*, vol. 48, no. 9, pp. 1844–9, 2001.

[39] M. Farahmand, M. Weber, L. Tirino, K. F. Brennan, and P. Ruden, "Theoretical study of direct-current and radio-frequency breakdown in GaN wurtzite- and zincblende-phase MESFETs," *Journal of Physics: Condensed Matter*, vol. 13, no. 46, pp. 10 477–86, 2001.

[40] M. Farahmand and K. F. Brennan, "Full band Monte Carlo simulation of zincblende GaN MESFET's including realistic impact ionization rates," *IEEE Transactions on Electron Devices*, vol. 46, no. 7, pp. 1319–25, 1999.

[41] M. Farahmand, "Advanced simulation of wide band gap semiconductor devices," Ph.D. dissertation, Georgia Institute of Technology, August 2000.

[42] H. Shichijo, K. Hess, and G. E. Stillman, "Simulation of high-field transport in GaAs using a Monte Carlo method and pseudo-potential band structures," *Applied Physics Letters*, vol. 38, no. 2, pp. 89–91, 1981.

[43] H. Shichijo and K. Hess, "Band-structure-dependent transport and impact ionization in GaAs," *Physical Review B (Condensed Matter)*, vol. 23, no. 8, pp. 4197–207, 1981.

[44] M. A. Littlejohn, J. R. Hauser, and T. H. Glisson, "Velocity-field characteristics of GaAs with γ-l-x conduction-band ordering," *Journal Applied Physics*, vol. 48, pp. 4587–90, 1977.

[45] M. V. Fischetti, "Monte Carlo simulation of transport in technologically significant semiconductors of the diamond and zinc-blende structures. I. Homogeneous transport," *IEEE Transactions on Electron Devices*, vol. 38, no. 3, pp. 634–49, 1991.

[46] W. Fawcett, A. D. Boardman, and S. Swain, "Monte Carlo determination of electron transport properties in gallium arsenide," *J. Phys. Chem. Solids*, vol. 31, pp. 1963–90, 1970.

[47] K. F. Brennan, E. Bellotti, M. Farahmand, H.-E. Nilsson, P. P. Ruden, and Yumin, "Monte Carlo simulation of noncubic symmetry semiconducting materials and devices," *IEEE Transactions on Electron Devices*, vol. 47, no. 10, pp. 1882–90, 2000.

[48] M. V. Fischetti and S. E. Laux, "Monte Carlo analysis of electron transport in small semiconductor devices including band-structure and space-charge effects," *Physical Review B (Condensed Matter)*, vol. 38, no. 14, pp. 9721–45, 1988.

[49] L. Tirino, "Transport properties of wide bandgap semiconductors," Ph.D. dissertation, Georgia Institute of Technology, Atlanta, GA, 2004.

[50] M. Farahmand, C. Garetto, E. Bellotti, K. F. Brennan, M. Goano, E. Ghillino, G. Ghione, J. D. Albrecht, and P. P. Ruden, "Monte Carlo simulation of electron transport in the III-nitride wurtzite phase materials system: binaries and ternaries," *IEEE Transactions on Electron Devices*, vol. 48, no. 3, pp. 535–42, 2001.

[51] F. Dessenne, D. Cichocka, P. Desplanques, and R. Fauquembergue, "Comparison of wurtzite and zincblende III-V nitrides field effect transistors: A 2D Monte Carlo device simulation," *Material Science Engineering B*, vol. 50, pp. 315–8, 1997.

[52] A. W. Smith and K. F. Brennan, "Hydrodynamic simulation of semiconductor devices," *Progress in Quantum Electron*, vol. 21, no. 4, pp. 293–360, 1998.

[53] E. Bellotti, "Advanced modeling of wide band gap semiconductor material and devices," Ph.D. dissertation, Georgia Institute of Technology, June 1999.

[54] M. Goano, E. Bellotti, E. Ghillino, G. Ghione, and K. F. Brennan, "Band structure nonlocal pseudo-potential calculation of the III-nitride wurtzite phase materials system. part I. binary compounds GaN, AlN, and InN," *Journal of Applied Physics*, vol. 88, no. 11, pp. 6467–75, 2000.

[55] M. Goano, E. Bellotti, E. Ghillino, C. Garetto, G. Ghione, and K. F. Brennan, "Band structure nonlocal pseudo-potential calculation of the III-nitride wurtzite phase materials system. part II. Ternary alloys $Al_xGa_{1-x}N$, $In_xGa_{1-x}N$, and $In_xAl_{1-x}N$," *Journal of Applied Physics*, vol. 88, no. 11, pp. 6476–82, 2000.

[56] E. Ghillino, C. Garetto, M. Goano, G. Ghione, E. Bellotti, and K. F. Brennan, "Simplex algorithm for band structure calculation of noncubic symmetry semiconductors: application to III-nitride binaries and alloys," *VLSI Design*, vol. 13, no. 1-4, pp. 63–8, 2001.

[57] H. K. Jung, K. Taniguchi, and C. Hamaguchi, "Impact ionization model for full band Monte Carlo simulation in GaAs," *Journal of Applied Physics*, vol. 79, no. 5, pp. 2473–80, 1996.

[58] Y. Kamakura, H. Mizuno, M. Yamaji, M. Morifuji, K. Taniguchi, C. Hamaguchi, T. Kunikiyo, and M. Takenaka, "Impact ionization model for full band Monte Carlo simulation," *Journal of Applied Physics*, vol. 75, no. 7, pp. 3500–6, 1994.

[59] H. K. Jung, H. Ohtsuka, K. Taniguchi, and K. C. Hamaguchi, "Ionized impurity scattering rate for full band Monte Carlo simulation in heavily doped n-type silicon," *Journal of Applied Physics*, vol. 79, no. 5, pp. 2559–65, 1996.

[60] M. Stobbe, R. Redmer, and W. Schattke, "Impact ionization rate in GaAs," *Physical Review B (Condensed Matter)*, vol. 49, no. 7, pp. 4494–500, 1994.

[61] S. E. Laux, M. V. Fischetti, and D. J. Frank, "Monte Carlo analysis of semiconductor devices: the DAMOCLES program," *IBM Journal of Research and Development*, vol. 34, no. 4, pp. 466–94, 1990.

[62] E. M. Conwell and V. F. Weisskopf, "Theory of impurity scattering in semiconductors," *Physical Review*, vol. 77, no. 3, pp. 388–90, 1950.

[63] J. Bude, K. Hess, and G. J. Iafrate, "Impact ionization in semiconductors: effects of high electric fields and high scattering rates," *Physical Review B (Condensed Matter)*, vol. 45, no. 19, pp. 10 958–64, 1992.

[64] L. Tirino, M. Weber, K. F. Brennan, E. Bellotti, M. Goano, and P. P. Ruden, "Fully numerical monte carlo simulator for noncubic symmetry semiconductors," *Journal of Computational Electronics*, vol. 1, no. 1-2, pp. 231–4, 2002.

[65] L. Tirino, M. Weber, K. F. Brennan, and E. Bellotti, "A general Monte Carlo model including the effect of the acoustic deformation potential on the transport properties," *Journal of Computational Electronics*, submitted for publication.

[66] A. W. Smith and K. F. Brennan, "Hydrodynamic simulation of semiconductor devices," *Progress in Quantum Electronics*, vol. 21, no. 4, pp. 293–360, 1997.

[67] H. Kosina, M. Nedjalkov, and S. Selberherr, "Theory of the Monte Carlo method for semiconductor device simulation," *IEEE Transactions on Electron Devices*, vol. 47, no. 10, pp. 1898–908, 2000.

[68] L. Tirino, M. Weber, K. F. Brennan, E. Bellotti, and M. Goano, "Temperature dependence of the impact ionization coefficients in GaAs, cubic SiC, and zinc-blende GaN," *Journal of Applied Physics*, vol. 94, no. 1, pp. 423–30, 2003.

[69] K. F. Brennan, *The Physics of Semiconductors: with applications to optoelectronic devices.* New York: Cambridge, 1999.

[70] B. K. Ridley, *Quatum Processes in Semiconductors, 3rd edition.* Oxford: Oxford University Press, 1993.

[71] H. M. Tutuncu and G. P. Srivastava, "Phonon dispersion on a GaAs(110) surface studied using the adiabatic bond charge model," *Journal of Physics: Condensed Matter*, vol. 8, no. 10, pp. 1345–58, 1996.

[72] H. Brooks and C. Herring, "Scattering by ionized impurities in semiconductors," *Physical Review*, vol. 83, pp. 879–87, 1951.

[73] T. Kunikiyo, M. Takenaka, Y. Kamakura, M. Yamaji, H. Mizuno, M. Morifuji, K. Taniguchi, and C. Hamaguchi, "A Monte Carlo simulation of anisotropic electron transport in silicon including full band structure and anisotropic impact-ionization model," *Journal of Applied Physics*, vol. 75, no. 1, pp. 297–312, 1994.

[74] D. Ong, K. F. Li, S. A. Plimmer, G. J. Rees, J. P. R. David, and P. N. Robson, "Full band Monte Carlo modeling of impact ionization, avalanche multiplication, and noise in submicron GaAs p^+-i-p^+ diodes," *Journal of Applied Physics*, vol. 87, no. 11, pp. 7885–91, 2000.

[75] C. Jacoboni and P. Lugli, *The Monte Carlo Method for Semiconductor Device Simulation*. New York: Springer-Verlag/Wein, 1989.

[76] N. H. Y. Awano, K. Tomizawa and M. Kawashima, "Simulation of GaAs submicron FET with hot-electron injection structure," *Electron. Letters*, vol. 19, no. 17, pp. 697–8, 1983.

[77] L. T. K. F. B. P. P. R. M. Farahmand, M. Weber, "Theoretical study of direct-current and radio-frequency breakdown in GaN wurtzite- and zinc-blende-phase MESFETs (metal-semiconductor field-effect transistors)," *Journal of Physics: Condensed Matter*, vol. 46, no. 13, pp. 10 477–86, 2001.

[78] E. C. S. Y. M. H. D. Heo, E. Gebara and J. Laskar, "An improved deep submicron MOSFET RF nonlinear model with new breakdown current model and drain to substrate nonlinear coupling," *2000 IEEE MTT-S International Microwave Symposium Digest*, no. 2, pp. 745–8, 2000.

[79] J. V. D. Schreurs, "Measuring transistor dynamic load lines and breakdown currents under large-signal high-frequency operating conditions," *1998 IEEE MTT-S International Microwave Symposium Digest*, no. 3, pp. 1495–8, 1998.

[80] C. J. W. Y. A. Tkachenko and J. C. M. Hwang, "GaAs MESFET lifetime prediction using microwave waveform probing," *47th ARFTG Conference Digest*, pp. 67–9, June 1996.

[81] J. Q. R. Teyssier, J.P.; Viaud, "A new nonlinear I(V) model for FET devices including breakdown effects," *IEEE Microwave and Guided Wave Letters*, vol. 4, no. 4, pp. 104–6, April 1994.

[82] E. G. M. G. G. Camarchia, V.; Bellotti, "Physics-based modeling of submicron GaN permeable base transistors," *IEEE Electron Device Letters*, vol. 23, no. 6, 2002.

[83] A. K. A. C. E. S. G. Carnez, B.; Cappy, "Modeling of a submicrometer gate field-effect transistor including effects of nonstationary electron dynamics," *Journal of Applied Physics*, vol. 51.

[84] W. Hänsch, *The Drift Diffusion Equation and its Applications in MOSFET Modeling*. New York: Springer-Verlag/Wein, 1991.

[85] K. Nummila, A. A. Ketterson, and I. Adesida, "Delay time analysis for short gate-length GaAs MESFETs," *Solid-State Electronics*, vol. 38, no. 2, pp. 517–24, 1995.

[86] M. Feng and J. Laskar, "On the speed and noise performance of direct ion-implanted GaAs MESFETs," *IEEE Transactions on Electron Devices*, vol. 40, no. 1, pp. 9–17, 1993.

[87] G. W. Wang, M. Feng, C. L. Lau, C. Ito, and T. R. Lepkowski, "0.25-μm gate millimeter-wave ion-implanted GaAs MESFETs," *IEEE Electron Device Letters*, vol. 10, no. 5, pp. 186–8, 1989.

[88] H. Kniepkamp, "GaAs MESFET, a low-noise microwave transistor," *Siemens Review*, vol. 44, no. 9, pp. 412–7, 1977.

[89] Y. C. Pao, W. Ou, and J. S. Harris Jr., "$\langle 110 \rangle$-oriented gaas mesfets," *IEEE Electron Device Letters*, vol. 9, no. 3, pp. 119–21, 1988.

[90] S. Shikata, J. Tsuchimoto, and H. Hayashi, "A novel self-aligned gate process for half-micrometer gate GaAs ICs using ECR-CVD," *IEEE Transactions on Electron Devices*, vol. 37, no. 8, pp. 1800–3, 1990.

[91] H. Daembkes, W. Brockerhoff, K. Heime, and A. Cappy, "Improved short-channel GaAs MESFETs by use of higher doping concentration," *IEEE Transactions on Electron Devices*, vol. ED-31, no. 8, pp. 1032–7, 1984.

[92] K. Nishimura, K. Onodera, S. Aoyama, M. Tokumitsu, and K. Yamasaki, "High-performance 0.1μm-self-aligned-gate GaAs MESFET technology," *IEEE Transactions on Electron Devices*, vol. 44, no. 11, pp. 2113–19, 1997.

[93] E. Bellotti, M. Farahmand, H.-E. Nilsson, K. F. Brennan, P. P. Ruden, R. J. Shul, F. Ren, W. Pletschen, and M. Murakami, "Monte Carlo based calculation of transport parameters for wide band gap device simulation," *Wide-Bandgap Electronic Devices Symposium (Materials Research Society Symposium Proceedings Vol. 622)*, vol. 622, pp. T6.24.1–6, 2000.

[94] H.-E. Nilsson, A. Martinez, M. Hjelm, E. Bellotti, K. F. Brennan, D. Tsoukalas, and C. Tsamis, "Monte Carlo simulation of multi-band carrier transport in semiconductor materials with complex unit cells," *Simulation of Semiconductor Processes and Devices 2001. SISPAD 01*, pp. 214–7, 2001.

[95] S. N. Mohammed and H. Morkoc, "Progress and prospects of group-III nitride semiconductors," *Progress in Quantum Electron*, vol. 20, no. 5-6, pp. 361–525, 1996.

[96] M. L. Cohen and T. K. Bergstresser, "Band structure and pseudo-potential form factors for fourteen semiconductors of the diamond and zinc-blende structures," *Physical Review*, vol. 141, no. 2, pp. 789–96, 1966.

[97] J. C. Phillips and L. Kleinman, "New method for calculating wave functions in crystals and molecules," *Physical Review*, vol. 116, no. 2, pp. 287–94, 1959.

[98] K. F. Brennan, N. Mansour, and Y. Wang, "Simulation of advanced semiconductor devices using supercomputers," *Computer Physics Communications*, vol. 67, pp. 73–92, 1991.

[99] J. Zimmermann, P. Lugli, and D. K. Ferry, "On the physics and modeling of small semiconductor devices. IV. generalized, retarded transport in ensemble Monte Carlo techniques," *Solid-State Electronics*, vol. 26, no. 3, pp. 233–9, 1983.

[100] C. Jacoboni and L. Reggiani, "The Monte Carlo method for the solution of charge transport in semiconductors with applications to covalent materials," *Reviews of Modern Physics*, vol. 55, no. 3, pp. 645–705, 1983.

[101] M. Saraniti, S. Wigger, G. Zandler, G. Formicone, and S. Goodnick, "Cellular automata studies of vertical MOSFETs," *1998 International Conference on Modeling and Simulation of Microsystems, Semiconductors, Sensors and Actuators*, pp. 437–48, 1998.

[102] M. Saraniti and S. Goodnick, "Hybrid full-band cellular automaton/Monte Carlo approach for fast simulation of charge transport in semiconductors," *IEEE Transactions on Electron Devices*, vol. 47, no. 10, pp. 1909–16, 2000.

[103] C. Jungemann, S. Keith, M. Bartels, and B. Meinerzhagen, "Efficient full-band Monte Carlo simulation of silicon devices," *IEICE Transactions on Electronics*, vol. E82-C, no. 6, pp. 870–9, 1999.

[104] S. Jallepalli, M. Rashed, W.-K. Shih, C. M. Maziar, and A. F. Tasch Jr., "A full-band Monte Carlo model for hole transport in silicon," *Journal of Applied Physics*, vol. 81, no. 5, pp. 2250–5, 1997.

[105] P. P. Ruden, E. Bellotti, H.-E. Nilsson, and K. F. Brennan, "Modeling of band-to-band tunneling transitions during drift in Monte Carlo transport simulations," *Journal of Applied Physics*, vol. 88, no. 3, pp. 1488–93, 2000.

[106] N. S. Mansour, K. Diff, and K. F. Brennan, "Ensemble Monte Carlo study of electron transport in degenerate bulk GaAs," *Journal of Applied Physics*, vol. 70, no. 11, pp. 6854–9, 1991.

[107] R. Mickevičius and J. H. Zhao, "Monte Carlo study of electron transport in SiC," *Journal of Applied Physics*, vol. 83, no. 6, pp. 3161–7, 1998.

[108] P. Lautenschlager, M. Garriga, S. Logothetidis, and M. Cardona, "Interband critical points of GaAs and their temperature dependence," *Physical Review B*, vol. 35, no. 17, pp. 9174–89, 1987.

[109] S. Adachi, "GaAs, AlAs, and $Al_xGa_{1-x}As$: material parameters for use in research and device applications," *Journal of Applied Physics*, vol. 58, no. 3, pp. R1–29, 1985.

[110] Y. Awano, K. Tomizawa, N. Hashizume, and M. Kawashima, "Monte Carlo particle simulation of a GaAs short-channel MESFET," *Electronics Letters*, vol. 19, no. 1, pp. 20–1, 1983.

[111] Y. Awano, K. Tomizawa, and N. Hashizume, "Principles of operation of short-channel gallium arsenide field-effect transistor determined by Monte Carlo method," *IEEE Transactions on Electron Devices*, vol. ED-31, no. 4, pp. 448–52, 1984.

[112] K. Tomizawa, Y. Awano, N. Hashizume, and M. Kawashima, "Simulation of GaAs submicron FET with hot-electron injection structure," *Electronics Letters*, vol. 19, no. 17, pp. 697–8, 1983.

[113] K. Tomizawa, Y. Awano, N. Hashizume, and M. Kawashima, "Simulation of near ballistic electron transport in a submicron GaAs diode with $Al_xGa_{1-x}As$/GaAs heterojunction cathode," *IEE Proceedings I (Solid-State and Electron Devices)*, vol. 132, no. 1, pp. 37–41, 1985.

[114] Y. Ando, W. Contrata, Y. Hori, and N. Samoto, "Monte Carlo simulation for electron transport in MESFETs including realistic band structure of GaAs," *IEEE Electron Device Letters*, vol. 20, no. 9, pp. 454–6, 1999.

[115] K. Tomizawa, Y. Awano, and N. Hashizume, "Monte Carlo simulation of GaAs submicron n^+-i(n)-n^+ diode with GaAlAs heterojunction cathode," *Electronics Letters*, vol. 18, no. 25-26, pp. 1067–9, 1982.

[116] M. Saraniti, A. Rein, G. Zandler, P. Vogl, and P. Lugli, "An efficient multigrid Poisson solver for device simulations," *IEEE Transactions on Computer-Aided Design of Integrated Circuits and Systems*, vol. 15, no. 2, pp. 141–50, 1996.

[117] C. Jungemann and B. Meinerzhagen, "Analysis of the stochastic error of stationary Monte Carlo device simulations," *IEEE Transactions on Electron Devices*, vol. 48, no. 5, pp. 985–92, 2001.

[118] T. González and D. Pardo, "Monte Carlo determination of the intrinsic small-signal equivalent circuit of MESFETs," *IEEE Transactions on Electron Devices*, vol. 42, no. 4, pp. 605–11, 1995.

[119] J. Bude and R. K. Smith, "Phase-space simplex Monte Carlo for semiconductor transport," *Semiconductor Science and Technology*, vol. 9, no. 5S, pp. 840–3, 1994.

[120] F. M. Bufler, A. Schenk, and W. Fichtner, "Efficient Monte Carlo device modeling," *IEEE Transactions on Electron Devices*, vol. 47, no. 10, pp. 1891–7, 2000.

[121] K. Tomizawa, Y. Awano, and N. Hashizume, "Monte Carlo simulator of AlGaAs/GaAs heterojunction bipolar transistors," *IEEE Electron Device Letters*, vol. EDL-5, no. 9, pp. 362–4, 1984.

[122] D. Schroeder and U. Witkowski, "Simulation of semiconductor devices with ideal metallic contacts," *IEEE Transactions on Electron Devices*, vol. 44, no. 4, pp. 679–81, 1997.

[123] K. Matsuzawa, K. Uchida, and A. Nishiyama, "A unified simulation of Schottky and ohmic contacts," *IEEE Transactions on Electron Devices*, vol. 47, no. 1, pp. 103–8, 2000.

[124] K. Matsuzawa, K. Uchida, and A. Nishiyama, "Monte Carlo simulation of sub-0.1μm devices with Schottky contact model," *IEICE Transactions on Electronics*, vol. E83-C, no. 8, pp. 1212–17, 2000.

[125] J. Sanchez and T. A. DeMassa, "Modeling gate emissions: A review - Part I," *Microelectronic Engineering*, vol. 20, no. 3, pp. 185–210, 1993.

[126] D. L. Woolard, H. Tian, M. A. Littlejohn, and K. W. Kim, "Efficient ohmic boundary conditions for the Monte Carlo simulation of electron transport," *IEEE Transactions on Electron Devices*, vol. 41, no. 4, pp. 601–6, 1994.

[127] D. L. Woolard, H. Tian, A. Littlejohn, and K. W. Kim, "The implementation of physical boundary conditions in the Monte Carlo simulation of electron devices," *IEEE Transactions on Computer-Aided Design of Integrated Circuits and Systems*, vol. 13, no. 10, pp. 1241–6, 1994.

[128] T. González and D. Pardo, "Physical models of ohmic contact for Monte Carlo device simulation," *Solid-State Electronics*, vol. 39, no. 4, pp. 555–62, 1996.

[129] A. Shibkov, M. Ershov, and V. Ryzhii, "Numerical simulation of carrier transport in Schottky barrier diodes," *Electronics Letters*, vol. 28, no. 19, pp. 1841–2, 1992.

[130] S. M. Sze, *Physics of Semiconductor Devices, 2nd ed.* New York: Wiley, 1981.

[131] S. M. Sze, *High-Speed Semiconductor Devices*. New York: Wiley, 1990.

[132] K. F. Brennan and A. S. Brown, *Theory of Modern Electronic Semiconductor Devices*. New York: Wiley, 2002.

[133] K. Tomizawa, *Numerical Simulation of Submicron Semiconductor Devices*. Boston: Artech House, 1993.